

UV/Photocatalyst Based Photoreactor Design for Water Treatment

by

Yongmei Jiao

A thesis submitted in partial fulfillment
of the requirements for the degree of
Doctor of Philosophy (PhD) in Engineering Science

The Faculty of Graduate Studies
Laurentian University
Sudbury, Ontario, Canada

© Yongmei Jiao, 2020

THESIS DEFENCE COMMITTEE/COMITÉ DE SOUTENANCE DE THÈSE
Laurentian Université/Université Laurentienne
Faculty of Graduate Studies/Faculté des études supérieures

Title of Thesis Titre de la thèse	UV/Photocatalyst Based Photoreactor Design for Water Treatment		
Name of Candidate Nom du candidat	Jiao, Yongmei		
Degree Diplôme	Doctor of Philosophy		
Department/Program Département/Programme	Natural Resources Engineering	Date of Defence Date de la soutenance	December 15, 2020

APPROVED/APPROUVÉ

Thesis Examiners/Examineurs de thèse:

Dr. John Ashley Scott
(Co-Supervisor/Co-directeur de thèse)

Dr. Tom Kovala
(Co-Supervisor/Co-directeur de thèse)

Dr. Helen Shang
(Co-Supervisor/Co-directrice de thèse)

Dr. Corey Laamanen
(Committee member/Membre du comité)

Dr. Nathan Basiliko
(Committee member/Membre du comité)

Dr. Jason Zhang
(External Examiner/Examineur externe)

Dr. Nelson Belzile
(Internal Examiner/Examineur interne)

Approved for the Faculty of Graduate Studies
Approuvé pour la Faculté des études supérieures
Dr. Lace Marie Brogden
Madame Lace Marie Brogden
Acting Dean, Faculty of Graduate Studies
Doyenne intérimaire, Faculté des études supérieures

ACCESSIBILITY CLAUSE AND PERMISSION TO USE

I, **Yongmei Jiao**, hereby grant to Laurentian University and/or its agents the non-exclusive license to archive and make accessible my thesis, dissertation, or project report in whole or in part in all forms of media, now or for the duration of my copyright ownership. I retain all other ownership rights to the copyright of the thesis, dissertation or project report. I also reserve the right to use in future works (such as articles or books) all or part of this thesis, dissertation, or project report. I further agree that permission for copying of this thesis in any manner, in whole or in part, for scholarly purposes may be granted by the professor or professors who supervised my thesis work or, in their absence, by the Head of the Department in which my thesis work was done. It is understood that any copying or publication or use of this thesis or parts thereof for financial gain shall not be allowed without my written permission.

Abstract

A germicidal ultraviolet (UV-C)/photocatalyst based advanced oxidation process (AOP) has potential to disinfect and mineralize waterborne organic pollutants without generating disinfection by-products. But low efficiency has hindered application of this technology. In this study, I have looked to improve the AOP process through use of enhanced photocatalytic surfaces and reactor design. The intention is that the resulting improvements will help in combating the effects of water eutrophication due to global warming, which is often accompanied by accelerated cyanobacterial (blue-green algae) growth and waterway contamination by their toxins.

An acidic anatase titanium dioxide (TiO_2) slurry doped with tungsten oxide (WO_3) or rutile TiO_2 was coated onto stainless steel plates, and annealed at 460, 500, and 540°C in a muffled furnace. The coatings were ~10 μm thick and demonstrated good durability. This method enabled bandgap reduction to the visible light spectrum for all coatings, with the smallest bandgap being 2.48 eV. The higher annealing temperatures resulted in rougher coated surfaces, which had negative effect on photocatalytic activities. Methylene blue (MB) degradation tests under UV-C showed that the coatings annealed in 460°C had the best performance and with a rate constant of 5.59 h^{-1} .

An UV-C/ TiO_2 based photocatalytic reactor with a corrugated configuration was designed to accommodate a larger photocatalytic surface per unit volume. With TiO_2 coated corrugated plates, a 70 % MB solution was degraded within the first 10 minutes with the highest photonic efficiency of 2.83 %. A light absorption model was developed and validated with light intensity measurements. A set of corrugated photocatalytic reactors with the same surface area, but

different geometries were analyzed and the one with flatter configuration showed better energy absorption capacity.

A household scale UV-C/TiO₂ reactor was then designed for drinking water treatment. A 3D UV-C absorption model, that agreed well with light intensity measurements, was used to predict light energy absorbed by the photocatalyst coatings and to optimize reactor design. The system degraded a synthesized raw water pollutant (uracil) and the organic matter in lake water by 34.2 % and 33.2 % respectively in 24 minutes, and also concurrently inactivated *Escherichia coli*.

Keywords

Corrugated photocatalytic reactor, Reaction modelling, Light absorption modelling, TiO₂, Coatings, Doping, Annealing, Band gap, Roughness, Advanced oxidation process, Household scale photocatalytic reactor, Drinking water TOC reduction, *E. coli* inactivation, 3D UV-C absorption model, Energy saving

Co-Authorship Statement

The Article *A Corrugated Plate Photocatalytic Reactor for Degradation of Waterborne Organic Contaminants* published by The Canadian Journal of Chemical Engineering **2019, volume 97**, co-authors are:

- A. Yongmei Jiao designed and built the corrugated reactor, performed experiments, modelling development and article drafting
- B. Dr. A. Thomas Kovala from the Northern Ontario School of Medicine, Sudbury ON Canada, offered critical revision on experimental work
- C. Dr. Helen Shang from the Bharti School of Engineering, Laurentian University, Sudbury ON Canada, contributed the concept design and modelling verification of the reactor
- D. Dr. John Ashley Scott from the Bharti School of Engineering, Laurentian University, Sudbury ON Canada, provided grant fund support, contributed the concept design, critical revision, and final inspection of the work, as well as editing of the article.

The Article *TiO₂ Based Nanopowder Coatings Over Stainless Steel Plates For UV-C Photocatalytic Degradation of Methylene Blue* published by The Canadian Journal of Chemical Engineering **2020, volume 98**, co-authors are:

- A. Yongmei Jiao designed, developed the coating method, performed experiments, theory analysis and article drafting
- B. Dr. Nathan Basiliko from the Bharti School of Engineering, Laurentian University, Sudbury ON Canada, contributed critical revision of the experiments

- C. Dr. A. Thomas Kovala from the Northern Ontario School of Medicine, Sudbury ON Canada, contributed data inspection of the work
- D. Dr. Jeffrey Shepherd from the Department of Chemistry and Biochemistry, Laurentian University, Sudbury ON Canada, contributed data collection
- E. Dr. Helen Shang from the Bharti School of Engineering, Laurentian University, Sudbury ON Canada, contributed the data inspection of the work
- F. Dr. John Ashley Scott from the Bharti School of Engineering, Laurentian University, Sudbury ON Canada, provided grant fund support, contributed the concept design, critical revision, and final inspection of the work, as well as editing of the article.

The article *A UV-C based advanced photooxidation reactor design for remote households and communities not connected to a municipal drinking water system* submitted to Journal of Environmental Chemical Engineering, co-authors are:

- A. Yongmei Jiao designed, built the household scale column reactor, performed experiments, modelling development and article drafting
- B. Dr. Helen Shang from the Bharti School of Engineering, Laurentian University, Sudbury ON Canada, contributed modelling inspection in this work
- C. Dr. John Ashley Scott from the Bharti School of Engineering, Laurentian University, Sudbury ON Canada, provided grant fund support, contributed the concept design, critical revision, and final inspection of the work, as well as editing of the article

Acknowledgments

I would like to express my gratitude to my supervisor Dr. John Ashley Scott, for the guidance and relentless support throughout my PhD journey. My sincere appreciations are also given to Dr. Helen Shang for the instruction and help with the reactor light irradiation modelling work, as well as Dr. A. Thomas Kovala, and committee members Dr. Corey Laamanen and Dr. Nathan Basiliko for helping with project development.

Many thanks to Dr. Gerusa Senhorinho for her support and tutoring on *Escherichia coli* testing, culturing, and other biological experiment instructions.

Special thanks are given Mr. William Zhe and Dr. Turgut Yalcin for the help with SEM imaging and XRD analysis, and to Dr. Jeffrey Shepherd for help with AFM analysis of the coated photocatalyst.

And many thanks to the Ongen team members in our group for giving me such a pleasant and supportive working environment.

Table of Contents

Abstract	iii
Co-Authorship Statement.....	v
Acknowledgments.....	vii
Table of Contents	viii
List of Tables	xiii
List of Figures	xiv
Nomenclature	xvi
Chapter 1 Introduction	1
1.1 Natural Organic Matter and Water Disinfection	1
1.2 UV Based Advanced Oxidation Processes	3
1.2.1 UV/Photocatalyst Process	4
1.2.2 UV/H ₂ O ₂ /Photocatalyst Process	7
1.2.3 Disinfection By-products	8
1.2.4 Energy Efficiency and Cost	9
1.3 Photocatalytic Reactor Design and Modelling.....	10

1.3.1 UV Irradiation	10
1.3.3 Reactor Design and Modelling	12
1.3.2 Photocatalyst	13
1.4 Reactor Design Challenges and this work	15
Chapter 2 A Corrugated Plate Photocatalytic Reactor for Degradation of Waterborne Organic	
Contaminants	18
2.1 Introduction	19
2.2 Experimental Details	22
2.2.1 Photocatalytic Reactor System Set-up	22
2.2.2 Preparing the TiO ₂ Coated Stainless Steel Plates	23
2.2.3 Experimental Runs	24
2.3 Results and Discussions	25
2.3.1 Comparison Tests	25
2.3.2 Factors Influencing Methylene Blue (MB) Degradation	26
2.3.2.1 Effect of flowrate	27
2.3.2.2 Effect of concentration	29
2.3.2.3 Reaction kinetics	30

2.3.3 Irradiation Modelling	33
2.3.3.1 UV-C absorption coefficient $\alpha(\lambda)$	35
2.3.3.2 UV-C lamp intensity modelling	36
2.3.3.3 3D LASREA modelling	38
2.3.3.4 Effect of geometry	46
2.3.3.5 Reactor performance	48
2.4 Conclusions	51
 Chapter 3 TiO ₂ Based Nanopowder Coatings over Stainless Steel Plates for UV-C Photocatalytic Degradation of Methylene Blue	
3.1 Introduction	52
3.2 Methodology	55
3.2.1 TiO ₂ Coating on Stainless Steel Plates	55
3.2.2 Characterization of Physical Properties	57
3.2.3 Bandgap Energy Evaluating of Coatings	58
3.2.4 Photocatalytic Activity in an UV-C/Photocatalyst Reactor	60
3.3 Results and Discussions	62
3.3.1 Adhesion Test and Durability	62

3.3.2 Coating Thickness and Coverage.....	62
3.3.3 Coating Roughness	64
3.3.4 XRD Assessment of the Rutile Ratio of the Coating.....	69
3.3.5 Bandgap Energy of Coatings	72
3.3.6 MB Degradation Using Plates with Different Coatings	73
3.3.7 Coating Parameter Analysis.....	77
3.4 Conclusion	79
 Chapter 4 An UV-C Based Advanced Photooxidation Reactor Design for Remote Households and Communities Not Connected to A Municipal Drinking Water System80	
4.1 Introduction	81
4.2 Experimental Details	84
4.2.1 Photocatalyst Coating	84
4.2.2 Reactor Design.....	85
4.2.3 Experimental Runs.....	87
4.3 Results and Discussions	88
4.3.1 Light Irradiance Absorption Modelling	88
4.3.1.1 3D UV-C Absorption Model for TiO ₂ Coated Surface	89

4.3.1.2 Model Validation	95
4.3.1.3 Model Justification in Water.....	96
4.3.1.4 Photonic Efficiency Comparison	98
4.3.2 Advanced Oxidation Experiments	98
4.3.2.1 Sample Run Naming	99
4.3.2.2 Disinfection and AOP	99
4.3.2.3 Uracil and Lake Water Natural Organic Matter Degradation.....	101
4.3.2.4 Electrical Energy Per Order (EE/O) Evaluations.....	107
4.4 Conclusions	107
Chapter 5 Conclusion and Future Work	109
5.1 Conclusion	109
5.2 Future Work	111
References.....	113
Appendices.....	120
Appendix a. <i>E. coli</i> Culture and Storage.....	120
Appendix b. Prototype Photoreactors	124

List of Tables

Table 1.1 AOP applications and DBPs overview	9
Table 2.1 Parameters used in LASREA modelling.	40
Table 2.2 Photonic efficiency of MB degradation with different reactors.	50
Table 3.1 Composition (wt.%) comparison between TiO ₂ coated and non-coated 316L steel plates	63
Table 3.2 Rutile wt.% at different annealing temperatures	71
Table 3.3 Bandgap energy obtained from photocatalyst powder before and after coating	73
Table 4.1 <i>E. coli</i> Inactivation Test.....	100
Table 4.2 Uracil and Lake Water NOM % Degradation in 24 Minutes	102

List of Figures

Figure 1.1 UV/TiO ₂ based advanced oxidation process (AOP).	5
Figure 2.1 the UV-C corrugated photocatalytic reactor system diagram.	23
Figure 2.2 Methylene blue degradation with three different reactor configurations.	26
Figure 2.3 Flowrate versus methylene blue degradation rate.	27
Figure 2.4 Methylene blue degradation at three different initial concentrations.	30
Figure 2.5 Linearized Langmuir-Hinshelwood model (Equation (2.2)).	32
Figure 2.6 Cosine emission for an element on a lamp surface.	36
Figure 2.7 A sphere coordinate system.	38
Figure 2.8 UV-C lamp irradiation coordinate system.	41
Figure 2.9 Cross section of a UV-C tube with projection to a point on the reactor plate.	43
Figure 2.10 Calculated and measured light intensity.	45
Figure 2.11 UV-C light intensity absorption profiles for each plate.	46
Figure 2.12 Reactor plate configurations with the same illuminated area.	47
Figure 2.13 Absorbed power by reactors with different number of plates and light source.	48
Figure 3.1 Determining the cut-off wavelength of photocatalyst powder and coatings.	60

Figure 3.2 The UV-C photocatalytic water treatment system.	61
Figure 3.3 TiO ₂ film thickness.	63
Figure 3.4 SEM images of plate surfaces.	65
Figure 3.5 AFM images of plate surfaces.	66
Figure 3.6 Annealing temperature vs. coating roughness.	67
Figure 3.7 Height distribution of scanned peaks (valleys) on coatings.	69
Figure 3.8 Anatase/rutile mixed coating XRD curves before annealing and after different annealing temperatures.	70
Figure 3.9 Methylene blue degradation vs. plate annealing temperature.	75
Figure 3.10 Methylene blue degradation rate constants with different coatings.	77
Figure 4.1 The experimental water purification system.	86
Figure 4.2 UV-C light absorption coordinate system.	91
Figure 4.3 Cross section view of a lamp irradiation to a point of the reactor.	93
Figure 4.4 UV-C powder absorption profile along the reactor wall.	95
Figure 4.5 Measured UV-C light irradiance and model predictions.	96

Nomenclature

Symbol	Description
3D	three dimensional
$\alpha(\lambda)$	absorption coefficient
AFM	atomic force microscope
AOP	advanced oxidation process
CYN	cylindrospermopsin
DBPs	disinfection by-products
DI	deionized water
DO	dissolved oxygen
<i>E. coli</i>	Escherichia coli
EE/O	electrical energy per order
E-H	electron-hole
eV	electron volt
H ₂ O ₂	hydrogen peroxide
HAAs	haloacetic acids
LASREA	local area-specific rate of energy absorption
LEDs	light emitting diodes
L-H	Langmuir-Hinshelwood
MB	methylene blue
NOM	natural organic matter
OH·	hydroxy radical
SEM	scanning electron microscope
THMs	trihalomethanes
TiO ₂	titanium dioxide
TOC	total organic carbon
UV	ultraviolet
WO ₃	tungsten oxide
WTP	water treatment plant
XRD	X-ray diffractometer
η	photonic efficiency

Chapter 1 Introduction

Water safety and quality are essential to human well-being and development. As a result of the progressive industrial development during the past century, global warming aggravates water eutrophication and natural organic matter contamination. Due to the well-known carcinogenic by-products generated by traditional chlorine disinfection and stricter drinking water regulations, alternative water treatment studies such as ultraviolet (UV)/photocatalyst based advanced oxidation process (AOP) have been gaining extensive interest. UV/photocatalyst based AOP has the potential to degrade water pollutant without generating disinfection by-products, but practical application is facing challenges because of low efficiency and high cost. In this study, the researcher has worked on improving AOP through use of an enhanced photocatalytic surface coating and reactor design. This Chapter is a review of the related issues regarding water treatment, photocatalyst, and reactor design.

1.1 Natural Organic Matter and Water Disinfection

The majority water for human consumption is taken from renewable surface water runoff and groundwater recharge; both these sources can be contaminated with bacteria (such as *E. coli*) and chemicals generated by agricultural, industry, and municipal discharges.^[1] It was reported that more than 40 % of water bodies are suffering moderate or heavy eutrophication.^[2] Due to the global warming and eutrophication, there had been increasing reported incidences of blue green algae contamination in potential drinking water sources over the last twenty years, including in Canada. As an autochthonous natural organic matter (NOM) source, blue green algae, a common cyanobacteria, tend to dominate in large lakes and produce toxin (cylindrospermopsin, CYN),

which may cause fever, diarrhea, hepatomegaly and kidney damage.^[3] CYN is very soluble in water and hard to remove with traditional water treatment methods or with natural (sunlight) UV irradiation, which greatly contributes to toxicity and NOM to water bodies.^[3]

NOM is an extremely complex mixture of organic compounds, which occurs naturally or from human activities through numerous hydrological and biogeochemical processes.^[4] Carbon is the key constituent of NOM and total organic carbon (TOC) has been used to quantify organic matter in particulate, colloidal, and dissolved form.^[4] The majority NOM can be removed during coagulation/sedimentation processes in a traditional water treatment plant.^[5] However, there is still part of the NOM that may enter the final disinfection stage, which may result in formation of harmful disinfection by-products (DBPs) with the traditional chlorination disinfection process, and also higher NOM concentrations can have adverse effects on pathogen inactivation.^[6]

The primary purpose of disinfection of water is to ensure microbial safety.^[6] Conventional chlorination has been the predominant method for decades, but it has been found to have the potential to produce carcinogenic DBPs, in particular trihalomethanes (THMs) and haloacetic acids (HAAs).^[7] As an alternative, UV disinfection has been applied in wastewater treatment in North America since the early 1980s,^[8] and was not introduced in drinking water treatment until late 1990s, when it was found to be effective in treatment of protozoa.^[9] UV light at a wavelength of 254 nm (the so called germicidal wavelength in the UV-C range) has high germicidal efficiency on almost all bacteria, viruses and protozoa, due to high absorption and subsequent inactivation of bacterial DNA.^[10] However, it does not significantly change the water quality in terms of reducing NOM, which is often required to meet drinking water safety targets.^[6]

There is a need to develop alternative safe and sustainable disinfection methods that can both kill pathogens and remove or degrade NOM (or TOC) in water. One example is ozonation, which relies on the generation of free radicals to destroy bacteria, but with bromate left behind.^[11-13] As a means of tackling harmful waterborne organic molecules, there is, therefore, significant growing interest in the use of advanced oxidation processes.

1.2 UV Based Advanced Oxidation Processes

Advanced oxidation processes (AOPs), which use a number of methods to achieve *in situ* production of highly reactive oxidization species to destruct organic matter, have been gaining significant attention in water treatment studies.^[14] AOPs can be roughly classified as ozone based, UV based, electrochemical, catalytic, and physical, which generate different types of oxidizing agents, such as sulfate, chlorine, and hydroxy radical (OH·).^[14] Among these radicals, OH· has the highest oxidizing capacity that has potential to mineralize organic matter without generating additional wastes. It is non-selective, not toxic with a short lifetime, and not corrosive to equipment.^[15] Some AOPs may generate harmful by-products or incur high capital costs, such as ozone-based AOPs.^[15] Since solar energy is free and UV-C disinfection systems have been applied to more and more water treatment plants (WTPs),^[8] the generating of OH· from UV based AOPs is seen to be potentially the most cost-effective.

UV based AOPs include homogenous such as UV/hydrogen peroxide (H₂O₂), the most common one used in drinking water treatment,^[16] and heterogeneous processes, such as UV/Titanium dioxide (TiO₂), the most popular catalyst in photocatalytic water treatment because of its high photocatalytic activity, insolubility in water, low cost, photo-corrosion resistance, and nobleness

with respect to chemical reactions.^[13,17] The potential of generating OH· without using chemicals has attracted extensive attention in UV/photocatalyst based AOP research.^[18]

1.2.1 UV/Photocatalyst Process

Photocatalysts are semiconductor materials that generate electron-hole (E-H) pairs upon receiving light, which enables chemical reactions of participating species with a self-regenerating ability after each reaction.^[19] As shown in Figure 1.1, electromagnetic rays in the UV-Vis spectrum can cause transition of photocatalysts (such as TiO₂) valence electrons between different electronic energy levels. When absorbing UV energy, valence electrons can jump from the valence band to the conduction band to form an electric current (e_{cb}^-), which is a necessary condition of photochemical reactions.^[20,21] Meanwhile positive holes are formed on the valence band ($h\nu_{vb}^+$) of photocatalysts which react with water, oxygen and ions as described by the following Equations:^[22,23]

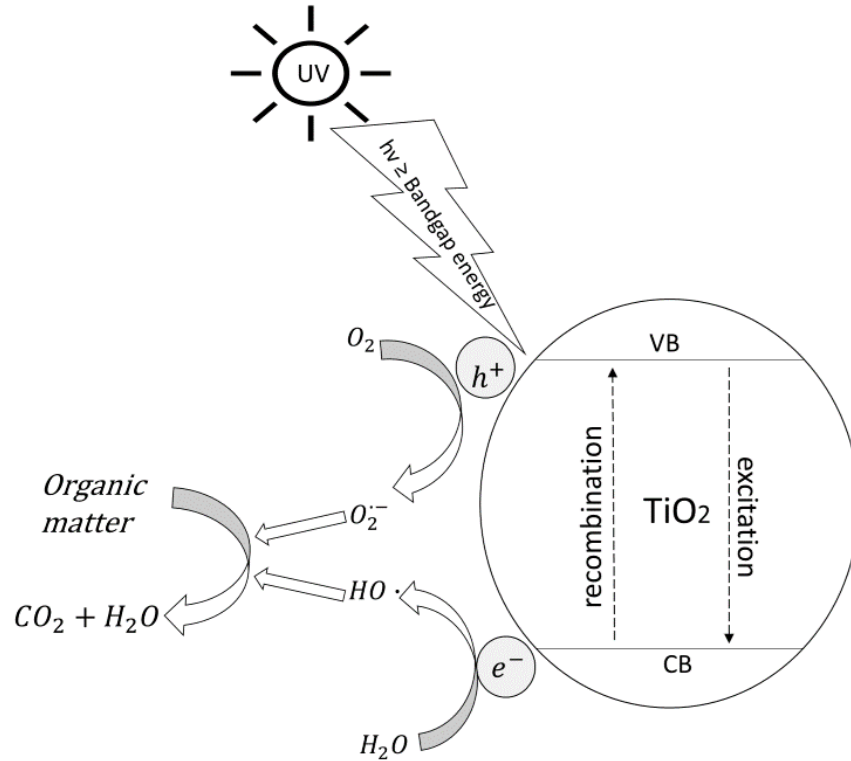
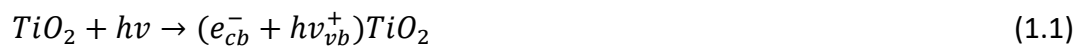


Figure 1.1 UV/TiO₂ based advanced oxidation process (AOP).



OH· formation process is complicated, but generally has the following reactions:^[24]





If the UV wavelength is less than 242 nm, water might go through direct photolysis: ^[23]



As shown in Equations (1.1) to (1.10), OH·s could be produced either through electrons reacting with oxygen, hydrogen ions, and hydrogen peroxide, or through reactions of the positive E-H pairs with water, oxygen, and hydroxyl ions. The life time of the OH·s is about 70 ns with a very slow diffusion rate, thus it has been assumed that they are only responsible for reacting with adjacent molecules only.^[25]

E-H recombination (the reverse reaction of Equation (1.1)) is detrimental to AOP processes, which degrade photoelectric energy into heat.^[26] Doping metal or non-metal ions into the TiO₂ lattice or mixing different forms of TiO₂ such as anatase with rutile can prolong the life time of charge carriers, slow down the E-H reunion, and increase reaction rate. Doping processes also help reduce the bandgap of catalyst materials, with generally a shorter bandgap meaning less photonic energy required to trigger a photocatalytic process.^[17] Other considerations of reducing E-H recombination are:^[27]

- immobilizing photocatalyst, due to the high E-H recombination, in a slurry reactor.
- different catalyst coating methods may result in different morphologies, which have different E-H recombination rates.
- applying electric potential on the TiO₂ film to control E-H recombination.

1.2.2 UV/H₂O₂/Photocatalyst Process

UV/H₂O₂/photocatalyst process involves three types of processes: UV/H₂O₂, UV/photocatalyst, and an independent process-UV/H₂O₂/Photocatalyst process. UV/H₂O₂ AOP is an well-established technology for water and waste water treatment, OH· production by UV irradiation to H₂O₂, the whole process is represented by Equation (1.11):^[28]



OH· formed during the cleavage of the O-O bond in H₂O₂, but it will undergo the following steps:^[28]



There are also termination reactions with the excessive unreacted HO·s:^[28]



The efficiency of OH· generation depends on light energy absorption and the nature of the molecules to be degraded. However, high concentrations of H₂O₂ may scavenge OH·s and may hinder the effectiveness of the oxidation, and hence the concentration may have to be adjusted to maximize the reactions.^[15] The cost of H₂O₂ is also high compared other chemicals when applied to AOP at a large scale WTP.^[16]

UV/H₂O₂/photocatalyst AOP produces a considerable increase in the photodegradation rate since with the addition of H₂O₂ (an effective “electron trapper”) into a UV/photocatalyst (TiO₂) system, the Equation (1.1) equilibrium shifting will produce more positive holes in the valance band to generate extra OH·s (Equation (1.17)).^[15]



It was reported that with a ferrihydrite doped TiO₂ photocatalyst, this UV/H₂O₂/photocatalyst AOP enabled improved E-H pairs separation, which resulted in more efficient degradation of the target pollutant than with UV/H₂O₂ alone.^[14]

1.2.3 Disinfection By-products

With the wide spread of UV disinfection and the application of AOPs, any resulting DBPs need to be also investigated.^[18] Because of different AOP application levels (full commercial, pilot plant, or laboratory), DBPs and the toxicity levels are different.^[18] Table 1.1 shows an overview of AOP applications and DBPs.

Table 1.1 AOP applications and DBPs overview

AOP	Application	DBP
UV /H ₂ O ₂	Full commercial, pilot plant, or laboratory applications were reported in worldwide for potable and re-use water treatment. ^[18,29]	No bromate products for raw water treatment; chlorophenols and chlorinated compounds were destructed; atrazine, desethylatrazine, and simazine were mineralized. ^[18] Likely enhanced iodinated DBP from the reaction of iodide and H ₂ O ₂ . ^[29]
UV /TiO ₂	Limited commercial applications were reported: slurry reactor and TiO ₂ coated reactor, but no pilot trials to validate DBP results yet; laboratory applications were reported; free of chemical addition may be a good potential of cost saving. ^[18]	TOC reduction reported with less DBP than chlorine treated water; 3-methyl-2,4-hexanedione was identified in treated water from ultrafiltration and UV/TiO ₂ processes. ^[18]
UV /TiO ₂ /H ₂ O ₂	Only wastewater pilot and bench-scale research data were found. ^[18]	Limited data were reported on potential DBPs with UV/TiO ₂ /H ₂ O ₂ process; herbicide (propyzamide) was reported to be decomposed into intermediates, but only being mineralized to CO ₂ and H ₂ O with additional ultrasonic treatment. ^[18]

1.2.4 Energy Efficiency and Cost

Using the most up-to-date information, a study of electrical energy per order (EE/O, electrical energy in kWh required to degrade a contaminant by one order of magnitude in 1 m³ of contaminated water) was made to compare the AOPs: UV/ H₂O₂ < 1kWh/m³ and UV/photocatalyst > 100 kWh/m³.^[14] Apart from energy comparison, reagent costs are high for

H₂O₂. Only with a reusable photocatalyst coating, can the UV/ H₂O₂/photocatalyst AOP have the potential to lower costs and improve performance.

1.3 Photocatalytic Reactor Design and Modelling

Reactor design is as critical as photocatalyst design in that it can influence mass transfer of contaminants to the photocatalyst surface and utilization of UV irradiation. Effective irradiation is essential because it determines the amount of water treated per effective unit area of deployed photocatalyst surface.^[13] Light absorption modeling is very important for a photocatalyst reactor design, since the more energy absorbed by the reactor, the more reactions may occur with a limited reactor volume and light sources

1.3.1 UV Irradiation

A photon is defined as a particle of light with a discrete bundle of electromagnetic energy (E), which can be expressed by Planck's Quantum Theory: ^[30]

$$E = hc/\lambda \tag{1.18}$$

where h is Planck constant, c is the constant velocity of light, and λ is the wavelength of the electromagnetic wave.

From Planck's theory, the shorter the wavelength, the higher the photonic energy. At the spectrum of UV-A (400-320 nm), UV-B (320-280nm), and UV-C (280-100 nm), the photon energy ranges from 3.10 to 12.4 eV (electron volt),^[31] which are almost equal or greater than bandgaps of photocatalyst.

Photons can be generated both from natural light rays and artificial lights, the latter achieved by passing electricity through a semiconductor in a light bulb, which is basically the reverse activity of photocatalysis.^[32] The sun emits electromagnetic rays with different energy levels, with most of the short-waved rays absorbed by the ozone layer, the long-wave rays reaching the Earth consist of (photonic energy level from low to high) infrared and visible lights, and UV rays (over 98 % is UV-A, less than 2 % is UV-B, and negligible UV-C).^[33] The light intensity reaching ground from the sun, especially at the UV range, is affected by a number of factors, such as position of the sun, amount ozone in the atmosphere, clouds, rain, fog, or altitude of the ground level.^[33] The light used in water disinfection is UV-C, which has to be produced artificially.

UV-C had been reported to inactivate water-borne microorganisms,^[27] and has been commercially applied in water disinfection for many years.^[34] UV-C in its germicidal spectrum of 200 to 280 nm, is especially damaging to bacterial cells due to the greater absorbing tendency by their DNA.^[10] Compared to UV-A and UV-B, a unit photon of UV-C possesses higher energy^[35] and has higher photon excitation potential.

Commercial applications of UV-A and UV-B lamps are mainly focused on coating, pest control, or medical applications (disease treatments).^[33] UV light emitting diodes (UV LEDs) have emerged in recent years for curing, medical and security purposes. The early versions of UV-C lamps only had a wavelength of 254 nm and were low-pressure mercury arc lamps containing mercury and an inert gas in a transmitting tube such as quartz. UV-C lamps with a broader spectrum (200-320 nm) of high energy are now commercially available.^[34] and UV-C LEDs have been also developed for water disinfection.^[36] Compared to traditional UV-C lamps, they are compact, eliminate mercury leaking, able to be switched on/off instantly, and robust with

longer life spans. However, their high cost and low wall-plug efficiency currently limit their application.^[36]

1.3.3 Reactor Design and Modelling

Reactor design is as equally critical as photocatalyst design in that it can influence mass transfer of contaminants to the photocatalyst surface and utilization of UV irradiation. Effective irradiation is essential because it determines the amount of water treated per effective unit area of deployed photocatalyst surface.^[13] The absorbed energy by a photocatalytic reactor can be modeled with the local area-specific rate of energy absorption (LASREA) method, with the energy absorbed by a photocatalytic reactor dependent on catalyst absorption properties, photonic energy diffused from the lamps, and reactor geometry.^[37,38] Light absorption modeling is very important to help optimize photocatalyst reactor scale-up design, since the more energy absorbed by the reactor, the more reactions may occur with a limited reactor volume and light source.

A photocatalytic reactor can be evaluated with the apparent photonic efficiency (or photonic efficiency), which is defined as the ratio of the reaction rate (in moles/second) to the efficient photonic flux (in photons/second, or Einstein/second, sometimes in %).^[37] It is regarded as a very important parameter to evaluate photocatalytic activity or reactor performance.^[26] Photonic efficiency comparisons have to be based on experimental conditions, catalyst nature, and the nature of the reaction.^[26] The photocatalytic reactor should be designed so as to provide sufficient high specific surface area of catalyst and effective illumination distribution across this surface.^[13]

There are three types of corrugated reactors designed for water treatment found in the literature: the first type is stationary corrugated plate reactor, which is immersed into water reservoir, with UV lamps laying above crossing trough all corrugated surfaces.^[39] The second is a rotating drum (corrugated shape) reactor powered by electric motors, a water film is formed during drum rotating and pollutants are degraded with UV lights above.^[40-42] The third is a stationary corrugated plate reactor that is located above reservoir with water distribution pipes above coated photocatalyst plates and with the UV irradiation on as well.^[37] The advantages of this layout is that there is no mechanical movement other than pumping a flow of water (saving energy) and the coated area being irradiated is maximized.

1.3.2 Photocatalyst

Photocatalysts in UV/photocatalyst based AOPs are directly involved in the reactions. Presently, although various type photocatalytic reactors have been designed, photonic efficiencies are generally low,^[27] with a major reason being the low efficiency of the photocatalyst materials.

A photocatalyst is a material that generates electron-hole (E-H) pairs upon receiving light, which enables chemical reactions of participating species and with self-regenerating ability after each reaction.^[19] The bandgaps between conduction band and valence band in photocatalytic materials (mostly semiconductors) are narrower than in insulators and broader than that in metals. Upon receiving sufficient energy or being struck by photons, it makes it possible for electrons to move from the valence band to the conduction band, where both an electric current and E-H pairs form on the surface.^[32] Bandgaps for some photocatalytic materials such as TiO₂, ZnO, WO₃, CdS are 3.1, 2.8, 2.8, 2.5 eV (electron-volt) respectively.^[17] The optimization of bandgap of a photocatalyst material has been one of the most important topics in photocatalyst design, since

with a shortened bandgap, a photocatalyst can be active through broad spectrum of light energy.^[43]

For water treatment purposes, a photocatalyst should be inexpensive, chemically stable to UV irradiation, and physically durable-titanium dioxide (TiO_2) has such properties.^[44] TiO_2 has three types of crystal structures, called anatase, rutile, and brookite.^[45] The anatase crystal has a high surface area and exhibits better photo activities than the other two structures. Doping rutile into anatase was reported to be able to lower the E-H recombination rate,^[46] whilst doping WO_3 in anatase can promote charge carrier transport.^[47] Proper doping can, therefore, result in higher photocatalytic activity than use of a pure composition.

Free photocatalyst suspensions in flow-through system not only pose problems for subsequent separation but could also increase costs due to loss of photocatalyst. However, there are slurry type reactors commercially available such as Photo-Cat[®], which take advantage of a ceramic ultrafiltration system to separate out the photocatalyst.^[18] The advantages of a photocatalyst suspension are large surface area and good interaction among reactants, but this can also block the penetration of UV flux, and post reaction filtration of the fine photocatalyst particles is required. Photocatalyst immobilization on a substrate for water treatment will avoid an after-treatment recovery process, and offer a different electron transfer path to slow down E-H recombination.^[22]

The selection of substrate materials for immobilisation, such as metals, glasses, and polymers, also depends on the reactor design. Metal substrates, such as aluminum and stainless steel, are usually adopted in industrial projects.^[17] Photocatalytic coating parameters such as particle size, surface area, film thickness, and crystal phase, crystallinity influence photocatalytic activities.^[22]

Reported coating methods include sol-gel, chemical vapor deposition, electrodeposition, sol-spray, and hydrothermal.^[22] Different compositions of photocatalysts, different substrates, different coating methods, different crystalline or curing temperature would result in different morphologies of coatings, which consequently influences photocatalytic activities.^[46]

TiO₂ anatase doped with other photocatalyst powders and cured onto steel plates has resulted in reduced bandgaps and better oxidation properties.^[43] Immobilized TiO₂ reactors are available to treat wastewater, swimming pool and potable water, but information on DBP formation is not available.^[18]

1.4 Reactor Design Challenges and this work

There have been over 8000 publications regarding photocatalytic water treatment (1999-2017), but only a very small portion is about reactor design.^[44] Furthermore, whilst UV/photocatalyst based AOPs have been a research subject for the past three decades, but unlike homogenous AOPs that have been well documented, heterogeneous AOP applications for water treatment are very limited.^[44]

The contrast between the number of literature publications and the few commercial applications can be attributed to bench-scale studies tend to over-represent opportunities and overlook limitations.^[44] Compared to commercialized UV/H₂O₂ processes, the main challenge lies in the low photoconversion efficiency. In organic matter free water, OH[·] production can reach 100 % with an UV/H₂O₂ process, but only reach to 2% in an UV/TiO₂ process.^[44] The advantage of UV/H₂O₂ AOP is, therefore, high conversion efficiency of OH[·]s, but it comes with a chemical cost and uncertainty over DBPs.^[18] However, since the cost of TiO₂ material is not expensive (~1

USD/kg),^[44] if it can be reused, cost savings in addition to chemical additive free operation will be of commercial value. There is also a benefit of the UV/TiO₂ process in that photocatalysts enable not only oxidation, but also reduction so they could reductively remove oxyanions such as nitrate, chromate, and redox-active metal ions.^[44] This way for example, Cr(VI) could be reduced to less toxic Cr(III), which is also easily precipitated out of solution.^[44]

Achieving better OH[·] conversion efficiency with a UV/TiO₂ process lies in advancement of photocatalyst material design to obtain safe, efficient, reusable and cost-effective surfaces. It also depends on better reactor design to achieve a better interaction among photons, water, and photocatalysts.^[13]

To adapt a bench-scale success to a commercial level one, an UV/TiO₂ process design has to be evaluated from various angles including cost, feasibility of large-scale production, tendency to foul in the proposed water matrix, and long-term stability.^[44]

The objective of this research project is to make contributions to the development of efficient and cost-effective photocatalytic reactor system from laboratory to household scales, and to gain insight into issues related to optimizing design and operation of the reactors.

As presented in Chapters 2, 3, and 4, this research objective was approached systematically with three major outcomes (two publications^[37,43] and one submitted manuscript):

- A 16-plates corrugated reactor with UV-C irradiation was designed, and the system performance was examined with a common waterborne compound methylene blue (MB). A 3D light energy absorption across the reactor was modelled and analysed; the reaction kinetics well agreed the Langmuir-Hinshelwood isotherm and the reactor performance was evaluated.

- A novel photocatalyst coating method was developed and analysed with different instruments and MB degradation experiments. Besides the good durability, all the bandgaps of the coatings were reduced from UV range to visible spectrum range.
- A household scale AOP column reactor was built, with the lined photocatalyst coating, it could not only disinfect *E. coli* but also degrade the model compound (uracil) with a practical volume, and the organic matter in the Lake water during a short period of time (24 minutes). A 3D light energy absorption model was developed to evaluate and compare the photonic efficiency and EE/O.

Chapter 2 A Corrugated Plate Photocatalytic Reactor for Degradation of Waterborne Organic Contaminants

Yongmei Jiao^a, A.Thomas Koval^b, Helen Shang^a, John Ashley Scott^{a*}

^a Bharti School of Engineering, Laurentian University, Sudbury, Ontario, Canada

^b Northern Ontario School of Medicine, Sudbury, Ontario, Canada

* corresponding author: jascott@laurentian.ca

Published by *The Canadian Journal of Chemical Engineering*, Volume 97 Issue 6, June 2019, Pages: 1760-1770

A UV-C/titanium dioxide (TiO₂) plate coated photocatalytic reactor using a corrugated frame system was designed for water borne organic contaminant degradation. The anticipated advantages of using the corrugated layout include a larger photocatalytic surface area per unit volume and improved photocatalytic activity. The water distribution system was designed to provide good interaction between the water pollutant, photocatalyst and photons. As a model organic contaminant, degradation of a methylene blue solution was carried out at room temperature at different concentrations and flowrates. With an 11 mg/L methylene blue solution, 70 % was degraded within the first 10 minutes using TiO₂ coated corrugated plates, whereas under the same conditions the degradation rate was only 12 % for a corrugated reactor without a catalyst coating, and 4 % for a no-plates reactor. Methylene blue degradation was described by the Langmuir-Hinshelwood model, and the apparent photonic efficiency of the corrugated arrangement was found to be in a range of 1.53 - 2.83 % when half the initial concentration was degraded.

The local area specific rate of energy absorption (LASREA) profile over the plates was determined from a model developed based on UV-C light irradiation distribution and plate configuration. Light intensity measurements were carried out and found to agree well with this model. A set of corrugated plate photocatalytic reactors with different geometries, but with the same coated area were then analyzed, and absorbed UV light intensities integrated to determine the best geometry.

2.1 Introduction

As a means of tackling harmful waterborne organic molecules, there is a significant interest in the use of advanced oxidation processes (AOPs). With these processes, non-biodegradable and toxic trace contaminating chemicals are oxidized and decomposed by generated hydroxyl radicals,^[48] or other oxidizing species such as Fe^{2+} and H_2O_2 .^[49]

Ultraviolet (UV) photocatalytic oxidation is a subset of AOPs.^[50] As electromagnetic wave, light from the UV-Vis region of the spectrum can drive transitions from the valence to the conduction band in semiconductors; when absorbing UV energy, the valence electrons can jump from valence band to the conduction band to form an electric current, and meanwhile positive holes are formed on the valence band, which is a necessary condition of photocatalytic reactions.^[20,21] Electron-Hole (E-H) recombination is detrimental to AOP process, which degrades photoelectric energy into heat.^[26]

Titanium dioxide (TiO_2) is the most popular catalyst in photocatalytic water treatment because of its high photocatalytic activity, insolubility in water, low cost, and low toxicity^[13] (except for fine particle inhalation).^[51] Doping metal or non-metal ions into the TiO_2 lattice or mixing

different forms of TiO₂ such as anatase with rutile can prolong the life-time of charge carriers, slow down the E-H reunion, and increase reaction rate.^[52,53] In water treatment process, free photocatalyst suspensions in flow-through systems would not be feasible for subsequent separation of water and catalysts and, therefore, its immobilization on reactor surfaces is necessary.

There are various UV band widths, including UV-C which is the germicidal spectrum of 200 to 280 nm. That is, the irradiation range that is especially damaging to bacterial cells due to a greater absorbing tendency by their DNA.^[10] Compared to UV-A and UV-B, a unit photon of UV-C possesses higher energy.^[35] Therefore, in water treatment using UV-C instead of UV-A or UV-B in a photocatalytic reactor should not only provide disinfection, but also enhanced oxidative degradation of waterborne pollutants. UV based AOPs also have the potential to degrade organic contaminants without the harmful by-products produced by other disinfection processes, such as chlorination or ozonation.^[11,13,54]

The photocatalytic material is critical to the AOP process as it is directly involved in the reactions. Reactor design is also critical in that it can influence mass transfer of contaminants to the photocatalyst surface and utilization of UV irradiation; effective irradiation is essential because it determines the amount of water treated per effective unit area of deployed photocatalyst surface.^[13]

Different types of UV photocatalytic reactors have been designed to degrade organic molecules in air and water.^[13,41,55-58] Due to the surface reactions, the reactor should be configured for optimum mass transfer of oxygen, reactant and product.^[13] In order to achieve these requirements, photocatalytic reactors with angled plates have been proposed as they can

accommodate more catalyst surface under a given illuminated area, and absorb photon energy more effectively.^[38,40]

Methylene blue (MB) is a common environmental pollutant in water bodies. It is estimated that 15 % of the total output of dyes are discharged into waterways and MB is among the most common industrial dyes.^[59] MB degradation with conventional water treatment methods is not however effective due to its stable molecular structure.^[60] MB solutions are, therefore, often used in photocatalytic material and reactor tests,^[12,40,61–63] with the photocatalytic materials adopted usually being either TiO₂, or TiO₂ doped with other elements. With a specified time period, the TiO₂/UV-based photocatalysis can result in the blue color of MB being lost due to decomposition into CO₂, NH₄⁺, NO₃⁻, and SO₄²⁻.^[64]

In this work, a UV-C/TiO₂ photocatalytic reactor using angled TiO₂ coated plates in a corrugated configuration was designed and tested through assessing MB degradation. The reactor system included a 3D printed system for effective water distribution over the plates. The anticipated advantages of using the corrugated layout are the larger surface area per unit volume and the possibility for “recapturing” reflected photons from the angled plates.

Absorbed UV-C light intensities were integrated to determine the best geometry option and MB degradation tests then carried out to confirm the impact of geometry on degradation efficiency. A kinetic study of MB degradation was carried out at different concentrations and flow rates, and Langmuir-Hinshelwood (L-H) kinetic analysis applied. The local area specific rate of energy absorption (LASREA) profile over the plates was also determined with a model developed from the properties of UV-C light irradiation and the TiO₂ coating. Light intensity tests were carried out to prove the validity of the model. Reactor performance was analyzed, and the photonic

efficiency was compared with regards MB degradation with other types of photocatalytic reactors.

2.2 Experimental Details

2.2.1 Photocatalytic Reactor System Set-up

The set-up of the corrugated UV-C photocatalytic reactor system is shown in Figure 2.1. The water distribution system and the plate frame were produced by a 3D printer (Dimension[®] 1200es, United States). The holes in the pipe running along the top of plates were designed to distribute water evenly onto 16 TiO₂ coated 304 stainless steel plates (3.5 cm × 9.7 cm × 0.13 cm each), which were placed on a 3D printed frame with an angle of 33.2° between adjacent plates. A 1 mm gap between adjacent angled plates was incorporated as this reduced bubble generation and accumulation of water on the TiO₂ coated steel plate surfaces. Due to the non-transparent nature of the plates, the top reactor area being illuminated by the lamp was 19.2 cm × 9.7 cm. A peristaltic pump (Kamoer[®], China) and a container (19 cm × 29 cm × 5 cm) completed the system.

An UV-C lamp (Odyssea[®], China) with a 36_watt power output produced monochromatic UV irradiation at a wavelength of 254 nm. There are two tubes in this lamp, each with a length of 38 cm and a diameter of 1.675 cm. There was a 0.125 cm gap between the two tubes.

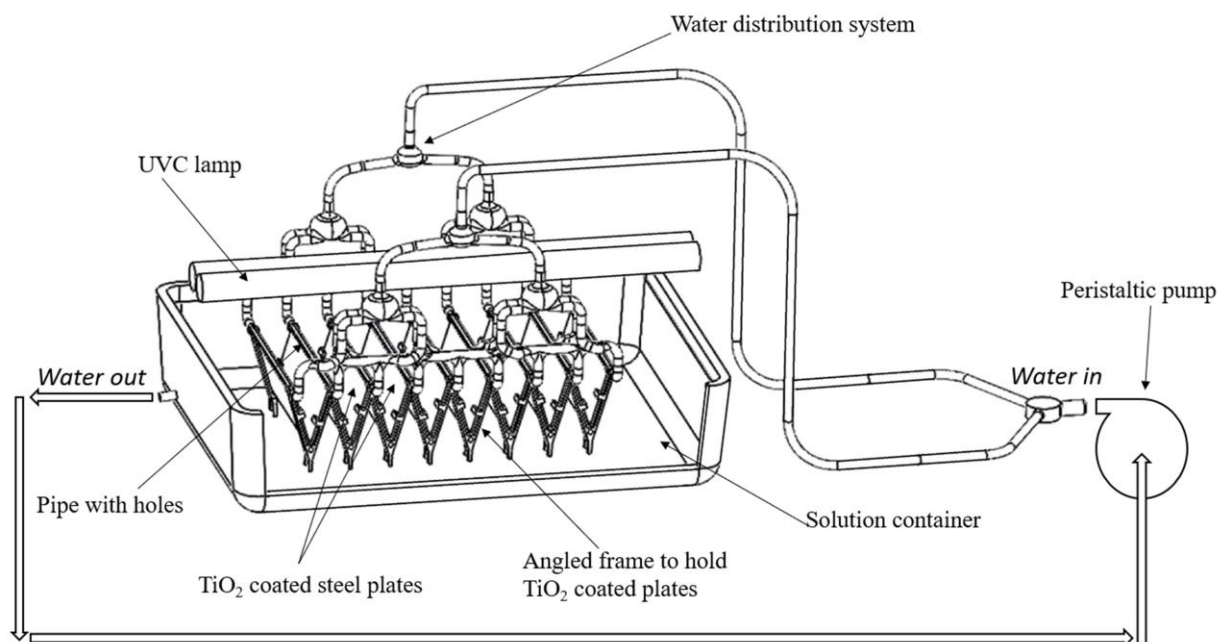


Figure 2.1 the UV-C corrugated photocatalytic reactor system diagram.

2.2.2 Preparing the TiO₂ Coated Stainless Steel Plates

The TiO₂ coating method used was modified from previously reported work.^[65] TiO₂ powder composed of 85 % anatase and 15 % rutile (Nanostructured & Amorphous Materials Inc., United States) was mixed into a 25 % ethanol solution to a slurry density of about 60 mg/mL. Stainless steel plates were oxidized by washing with 25 % (V/V) hydrochloric acid before being baked in a muffle furnace at 200°C for 2 hours. The TiO₂ slurry was then brushed onto the steel plates, which were further baked at about 270°C for 5 hours. They were then washed, dried, and recoated with the same slurry and the process repeated until the TiO₂ loading was above 1mg/cm², which was determined by weighting the plates. Based on the bulk density (0.25 – 0.3 g/cm³) of TiO₂ and the average loading (42 mg) on a plate (9.7cm × 3.5cm), the thickness of

TiO₂ film is estimated to be between 41 to 49 μm. The coated steel plates (or bare steel plates) were then soaked in milli-Q water for 1-2 hours before use in the photo reactor.

After each experimental run, the coated steel plates were washed with detergent, rinsed, air dried, and then oven dried at 250 °C. The loss of TiO₂ was about 1.6 mg during each run for a plate with an initial average loading of 42 mg. The plates were reused for five runs without any apparent loss in efficiency.

2.2.3 Experimental Runs

All experiments were conducted in a dark chamber. For each experimental run, 250 mL MB solution samples were prepared, which were diluted with milli-Q water to concentration ranges of 20, 11 and 5 mg/L.

Experiments were conducted with and without TiO₂; with bare plates in a corrugated configuration and with TiO₂ coated plates in a corrugated configuration (Figure 2.1). The MB solution was circulated in the system until its concentration stabilized. Changes in MB concentration were assessed by a spectrophotometer (HACH® DR2800) at a wavelength of 661nm; MB absorption curve was linear under 6 mg/L of concentration, for higher concentration measurement, solution was diluted to obtain an accurate result. All tests were conducted at room temperature (21±2°C) and with solution initial pH at 5.4 ± 0.2, depending on the pH of milli-Q water. Over a one-hour run, the temperature increase was 0.9±0.2°C, and no evaporation of water was observed.

2.3 Results and Discussions

2.3.1 Comparison Tests

Three reactor configurations were set up. The first was with a UV-C lamp but without any plates, the second had 16 bare uncoated steel plates ($3.5\text{cm} \times 9.7\text{cm} \times 0.13\text{cm}$ each) in a corrugated layout (Figure 2.1), and the third was with 16 TiO_2 coated plates in the corrugated configuration (33.2° between two adjacent plates). One of the advantages of a corrugated reactor is that it can accommodate much more coated catalytic area under a specified irradiated area. For example, with our reactor the top area being irradiated (above all the reactor plates) was 186.24 cm^2 , but with the 16-plates corrugated layout, the total photocatalyst coated area illuminated was 543.2 cm^2 , which is about 3 times that of a flat-plate reactor located in the same illuminated area.

Degradation tests were conducted with these three reactor configurations with a water volume of 250 mL and an MB concentration of 11 mg/L. Figure 2.2 shows that after one hour there was 12 % MB degradation with the non-coated 16-plates reactor and only 4 % degradation with the no-plate reactor. Whereas, with the TiO_2 coated 16-plates corrugated reactor, 70 % of the MB was degraded within the first 10 minutes, and more than 90 % after an hour.

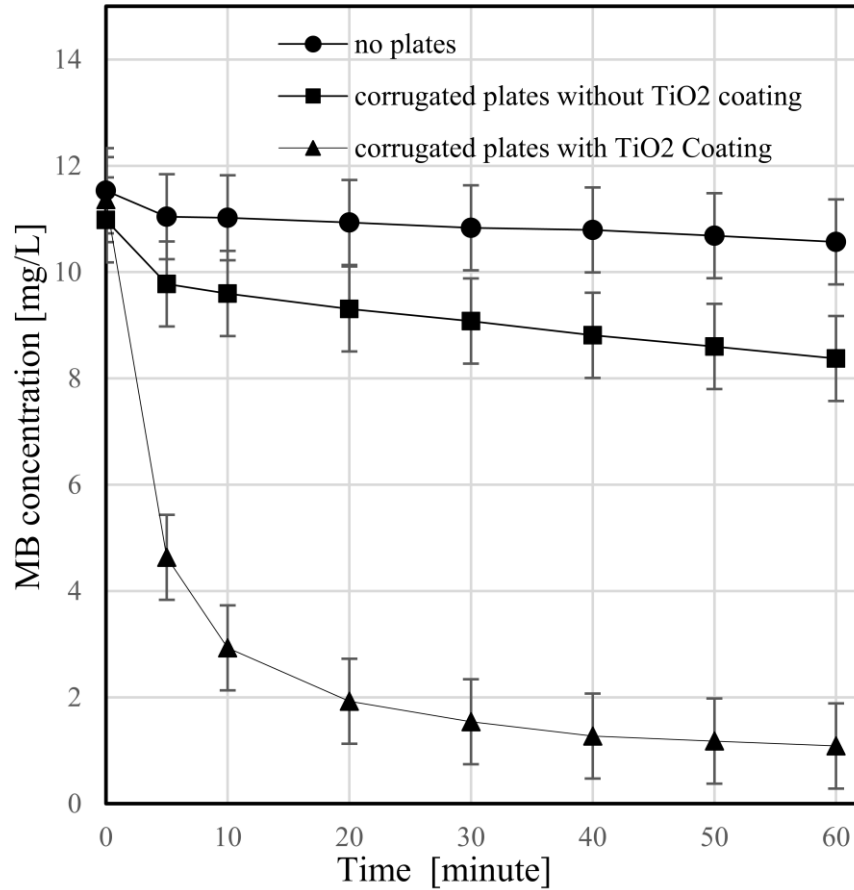


Figure 2.2 Methylene blue degradation with three different reactor configurations.

The different MB degradation results with the three reactor configurations in Figure 2.2 also demonstrate that UV-C irradiation alone can only result in a low photochemical MB degradation, although the presence of the angled plates does enhance the level. The latter is presumably due to the 16-plates configuration improving mass transfer and interaction among photons, MB and water molecules.

2.3.2 Factors Influencing Methylene Blue (MB) Degradation

2.3.2.1 Effect of flowrate

MB degradation tests at an initial concentration of 11 mg/L were conducted at four different flowrates (553, 725, 850, and 975 mL/min) with the 16-plates photocatalytic reactor. The results (Figure 2.3) show that the highest (first ten minutes) initial degradation rate was obtained at 725 mL/min.

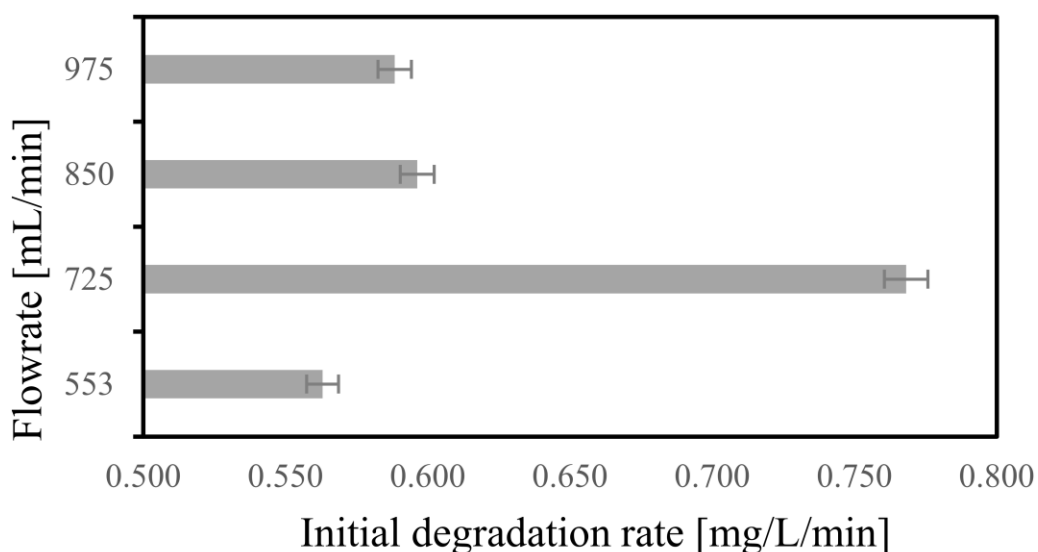


Figure 2.3 Flowrate versus methylene blue degradation rate.

The significance of MB flowrate on degradation indicated the importance of mass transfer to a heterogeneous process. The photocatalytic reaction relies on the flow to transport the reactant onto the catalytic surface, where the pollutant is adsorbed and the reaction occurs, and then to take degradation products away.^[26] Due to the surface reaction nature of the photocatalytic process, research on photocatalyst surface flow profile/pattern had been crucial to optimizing

reactor design.^[12,39,40,54] The reactor design in this paper is different from other reactors and the authors discuss experimental results from a fluid dynamic aspect in order to analyze the vital adsorption part of the process.

As shown in Figure 2.1, the MB solution was distributed from the pipes along the top of the plates and could be described as laminar flow. As the MB solutions in the tests are at low concentrations, the adsorption process can be assumed to be largely dependent on the surface friction of the flow. If we consider the flow is in a pipe with a relatively large diameter, the surface friction factor can be estimated from Equation (2.1):^[66]

$$f = \frac{64}{Re} \quad (2.1)$$

where f is the friction factor, a dimensionless empirical factor that is a function of Reynolds number (Re), which is a function of pipe diameter, average fluid flow velocity, fluid density, and the dynamic viscosity of the fluid. For laminar flow with a fixed pipe size, flow density and dynamic viscosity of the water bases solution will change with temperature. However, as the temperature was the same for all experiments, Re will in our case change only with the flow rate. Therefore, when flowrate increases the friction factor will decrease and less adsorption will occur on the pipe surface.

The results indicate that higher pump speed or higher flowrate reduced MB adsorption on the coated surface, and thus reduced the degradation rate. With a pump speed lower than 725 mL/min, the photocatalytic area was not fully utilized, and with a pump speed above 725 mL/min, degradation rate was reduced as adsorption decreased.

As atmospheric oxygen has to penetrate through the solution film and reach the coated surface for the photocatalytic reaction to happen,^[39] sufficient adsorption is needed to enable this to occur.

2.3.2.2 Effect of concentration

MB degradation was carried out at a flowrate of 725 mL/min at initial concentrations of 20, 11, and 5 mg/L (Figure 2.4), and the degradation rates over the first 10 minutes found to be 1.22, 0.77, and 0.39 mg/L/min respectively. For each concentration three runs were performed, and the variation was $\pm 9.6\%$.

Higher degradation rates at higher concentrations of MB indicate that adsorption sites on the catalytic surface were greater than the number of reacting molecules, and, therefore, the system did not appear to be saturated. Further solution tests would, therefore, need to be done in order to find the maximum capacity of the reactor.

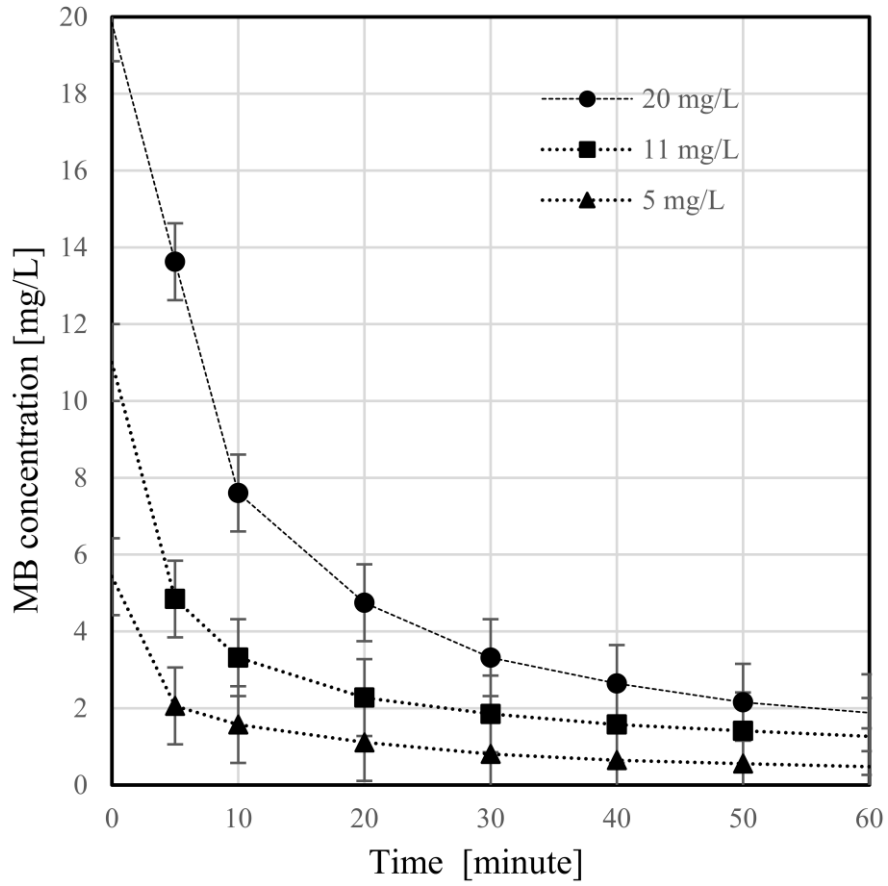


Figure 2.4 Methylene blue degradation at three different initial concentrations.

2.3.2.3 Reaction kinetics

In a heterogeneous photocatalytic process, photoexcitation produces electrons and hole-pairs on the surface where organic molecules are adsorbed and reacted with hydroxyl radicals or recombined with electrons.^[59] MB degradation in a heterogeneous photocatalytic system can be described by the Langmuir-Hinshelwood model, which can be expressed as Equation (2.2):^[59]

$$\frac{1}{r_0} = \frac{1}{k_r} + \frac{1}{k_r k_a C_0} \quad (2.2)$$

where r_0 is the degradation rate (from $t = 0$ to $t = 10$ minutes, the relative linear part), k_r is the specific reaction rate constant, k_a the equilibrium constant, and C_0 the initial concentration. For this batch reactor, the degradation rate r_0 is obtained from the concentration change with time (the first 10 minutes in this work) from Equation (2.3):

$$\frac{dC}{dt} = -r \quad (2.3)$$

where r is the instant rate of MB degradation and C the instant concentration of MB.

By plotting the inverse of rate for the first 10 minutes, r_0 , for five different initial concentrations ($C_0 = 20, 17, 11, 7,$ and 5 mg/L), against the inverse initial the concentration, a straight line was obtained (Figure 2.5). From the slope and intercept with the y-axis, k_r and k_a were determined to be 9.852 mg/(L·min) and 0.008 L/mg respectively.

It is, however, difficult to compare the apparent constant for different designs of reactors. In some literature the product of k_r and k_a was considered as the apparent rate constant, and the unit is in time^{-1} .^[67] For example, the apparent rate constant for MB degradation in a solar photocatalytic reactor with TiO_2 suspended in water was reported as 0.035 /h,^[68] whilst in this paper it is 4.55 /h. The apparent rate constant for a spinning disc reactor with immobilized TiO_2 was reported as 0.0003 /s,^[54] whilst in this paper it was 0.0013 /s.

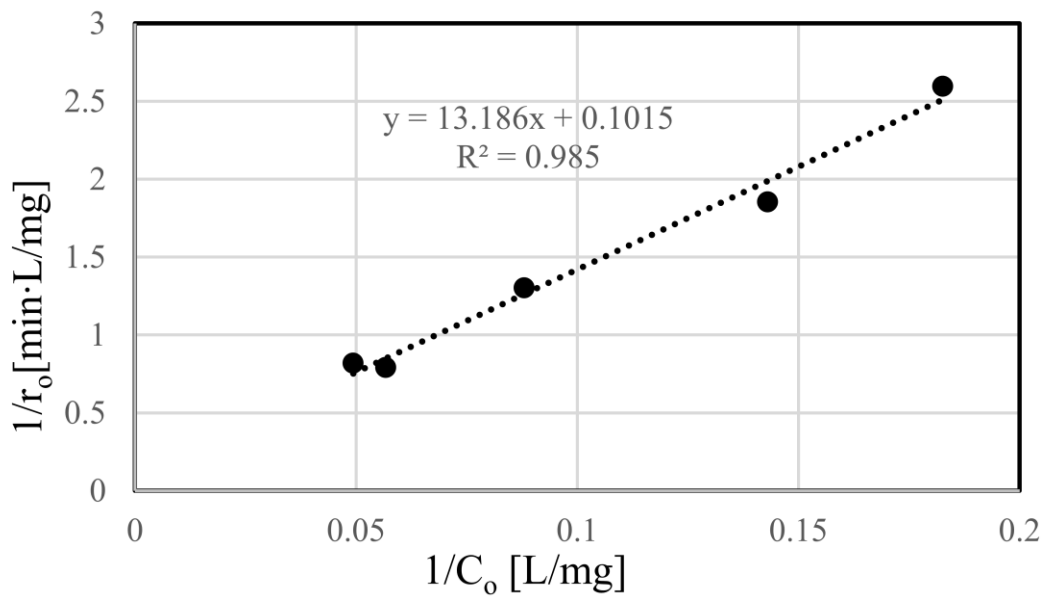


Figure 2.5 Linearized Langmuir-Hinshelwood model (Equation (2.2)).

The whole process was, however, described well by the L-H model, which confirms that heterogeneous catalytic character of the system.^[26] This confirmation also means the catalyst's properties are well preserved during the coating process and there was no significant loss or dissolution of catalyst. Whereas for example, if choosing ZnO as catalyst, in water treatment there may be zinc ions dissolved into the water,^[69] and, therefore, it would not be a full heterogeneous process.

Using a dye to evaluate photocatalytic reaction had been controversial, because dye materials (including MB) have light absorption peaks at the visible light range, and, therefore active dye decolorization occurs under solar light, which is referred to as sensitization; degradation may, therefore, involve a photosensitization mechanism,^[70] which is not a photocatalytic process and cannot be described by the L-H model. However, the model is still appropriate for evaluating

photocatalytic processes under UV-C light (e.g., light at a wavelength of 254 nm) due to the large wavelength gaps between UV-C wavelengths and dye active decolorization wavelength peaks (Figure 2.2).^[70] With UV-C irradiation only, MB concentration did not change much within one hour, but with the photocatalyst reactor, MB degraded significantly, and the reaction was a good fit to L-H model, demonstrating the heterogeneous catalytic nature of the reaction.

2.3.3 Irradiation Modelling

Photocatalytic reactors rely on photocatalysts and photons to carry out reactions. To evaluate and optimize the performance of a photocatalytic reactor as well as to prepare for scale-up design, irradiation modelling is essential to evaluate the photon energy absorption on the photocatalyst surface. With other conditions fixed, the more radiation energy absorbed, the more reactions may occur.

Different designs of corrugated photocatalytic reactors with simulated solar radiation (UV-A or UV-B lamps) have been previously discussed,^[38,59] and it was found that photon energy absorption on an angled catalyst coated film was enhanced by catching the reflected photons.

Several radiation absorption models corrugated reactors have been proposed, including the local volumetric rate of energy absorption (LVREA), which is more suitable dealing with gas phase reactions; and local area specific rate of energy absorption (LASREA), which expresses radiation absorption profiles in heterogeneous photocatalytic reactors, is more suitable for liquid phase reactions.^[38] Energy absorbed by a reactor not only depends on the incident energy, but also the catalyst coating, and the reactor geometry, with the catalyst coating directly affecting the UV-C absorption coefficient, $\alpha(\lambda)$.^[38]

Using LASREA modelling to evaluate reactor photon energy absorption in corrugated reactors had been reported,^[38-40] where a diffuse emission model was adopted for lamp modelling. However, when calculating light intensity absorption, half sphere coordinates were applied, whereas a full sphere coordinate system was used for emitter light intensity modelling by others,^[71] which is considered reasonable in that the emitter on a lamp emits light rays in all directions. The reactor light energy absorption profiles derived in reported literature^[38-40] were all in two dimensions (2D) with one extruded from a 2D profile, and with simplified lamp surface modelling. For this work, a 3D LASREA profile was developed across the whole projected surface area of all the lamp(s) in order to provide more precise energy absorption profiles. The derived model was also tested with a light intensity detector, which agreed well.

As light rays are vectors with a diffusive emission nature, energy absorption profile is influenced by the reactor geometry. Therefore, as predicting the photon energy absorption is very important in photocatalytic reactor design, this 3D LASERA model can be used to optimize reactor geometry.

Photonic efficiency is also a very important parameter to evaluate the performance of a photocatalytic reactor, which requires the information of incident energy to a reactor and reaction rate, LASERA model can be used to calculate the incident energy that is needed for evaluating reactor performance.

2.3.3.1 UV-C absorption coefficient $\alpha(\lambda)$

As a photocatalytic material, titanium dioxide, especially in its anatase form, is readily excited by photon energy, where energy is transferred by its electron from the valence band to its conduction band, which generates an E-H pair. The more photon energy is absorbed, the more E-H pairs generated, and the more photocatalytic reactions occur. The optical absorption coefficients of materials determine the penetration depth of the light, and these values strongly depend on the wavelength of the light.^[72]

The spectral absorption coefficient $\alpha(\lambda)$ of the TiO₂ coating is the fraction of the absorbed incident energy of wavelength λ . The relationship is expressed in Equation (2.4):^[40]

$$\alpha(\lambda) = 0.5 - 0.5 \tanh\left[\frac{\lambda - 355.66}{12.743}\right] \quad (2.4)$$

As the UV-C lamp used had a wavelength of 254 nm and the coating method was similar to that previously described,^[40] then $\alpha(\lambda)$ can be taken as equal to 1, that is the incident energy was totally absorbed by the coated film, with no reflection.

With UV-A or UV-B irradiation, $\alpha(\lambda)$ will be less than 1, which means a fraction of the photons will be reflected, and if this happens in a corrugated reactor, the reflected photons could, therefore, be a new source of radiation to be projected onto an adjacent reactor plate.^[40]

2.3.3.2 UV-C lamp intensity modelling

The incident energy on a reactor is determined by the lamp irradiation. Elements in a UV-C fluorescent lamp surface are considered as Lambertian Emitters that have a diffuse or cosine emission pattern with respect to the lamp surface^[71] (Figure 2.6):

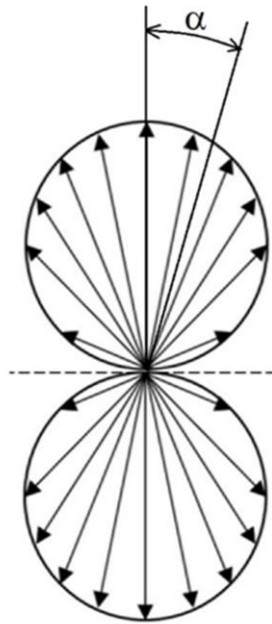


Figure 2.6 Cosine emission for an element on a lamp surface.

According to the cosine emission theory, if an element on the surface in the lamp's normal direction has a light intensity I_0 , then for a direction of angle α to the normal, the light intensity I can be expressed as Equation (2.5):^[39,55]

$$I = I_0 \cos \alpha \quad (2.5)$$

Due to the diffuse emission nature of the UV-C ray, the received light intensity decreases with distance from the source.^[55] The magnitude of the irradiated light power (I_0) at any point from the source element can be derived from a sphere coordinated system. If a light source element (with a power of dP) is enclosed in a spherical surface with a radius of r (Figure 2.7), the total power received by the sphere surface area be written as Equation (2.6):^[71]

$$dP = 2 \int_0^{\pi/2} I_0 \cos \alpha (2\pi r \cdot \cos \alpha) r d\alpha = I_0 \pi^2 r^2 \quad (2.6)$$

Therefore, the value of the light power received from any differential area on the plate surface equals Equation (2.7):

$$I_0 = \frac{dP}{\pi^2 r^2} \quad (2.7)$$

In previous work,^[38,39] the expression of this value is different as the power source is considered to be enclosed in a half sphere. This results in a difference of $1/\pi$, and consequently, for the calculated LASREA, there will be a fixed proportional difference of $1/\pi$.

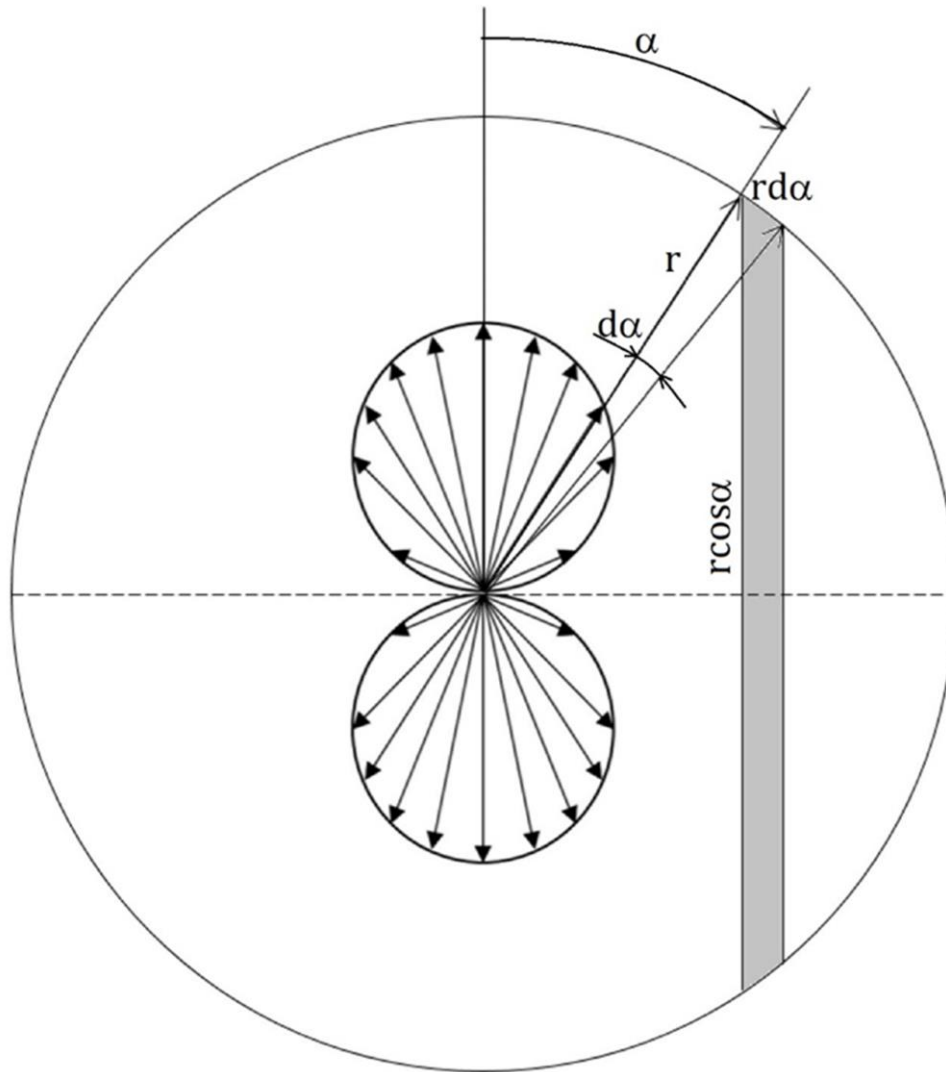


Figure 2.7 A sphere coordinate system.

2.3.3.3 3D LASREA modelling

Since the distance between the UV-C lamp and the corrugated plates is relatively close, it is inaccurate to model the lamp tube as a line source. Instead, a cylindrical surface is modelled as

the radiation source. Any differential area under the lamp, therefore, receives light from all projectable areas from the lamp section.

The absorbed energy at any point on a reactor plate depends on the light intensity value, the angle from light source normal, incident direction to the reactor plate, and the absorption coefficient.^[38,39,71] A three-dimensional coordinate system was, therefore, set-up for the reactor system, with Figure 2.8 depicting any two angled plate surfaces I and II under the lamp tube, with the tube axis coincident to the Y-axis. As the absorption coefficient is assumed to be 1, this means all the photonic energy can be absorbed by the plates and no photon reflection need to be taken into account. Furthermore, as the irradiation condition is identical to both plates only one plate and the incident energy need to be calculated. The parameters used in LASREA calculation are given in Table 2.1.

Table 2.1 Parameters used in LASREA modelling.

$\alpha(\lambda)$	absorption coefficient of the TiO ₂ film
dP	specific intensity on the lamp surface = output power/lamp surface area
P	a random point on the plate, with known coordinates
P'	a random point on the lamp tube that can be projected to P
\vec{n}_{lamp}	lamp normal vector
\vec{pp}'	irradiation ray vector
r	modulus of vector \vec{pp}'
\vec{n}_I	the normal vector of surface I
α	angle between lamp normal \vec{n}_{lamp} and vector \vec{pp}'
β	angle between \vec{pp}' and the plate surface normal \vec{n}_I or \vec{n}_{II}
ϕ	half angle between the plates
a	width of the plate
b	half plate length
l	half-length of the lamp projection from the angled plates
d	distance from the lamp bottom to the top of the plates
R	lamp transection radius
θ_1, θ_2	angles at the cross section of lamp surface where two end tangent points project to a specified point on the reactor plate (Figure 2.9)
θ	any angle between θ_1 and θ_2
t	any point at Y-axis on which the cross-section elements can be projected to the reactor plate

The intensity absorbed along the lamp surface by any point on one of the reactor plates can be expressed as Equation (2.8):

$$I = a(\lambda) \frac{dP}{\pi^2} \iint_{\text{lamp surface}} \frac{\cos \alpha \cdot \cos \beta}{r^2} ds \quad (2.8)$$

Based on this 3D system, the normal vector of surface I is Equation (2.9):

$$\vec{n}_I = (ab \cdot \cot \varphi)j + (-ab)k \quad (2.9)$$

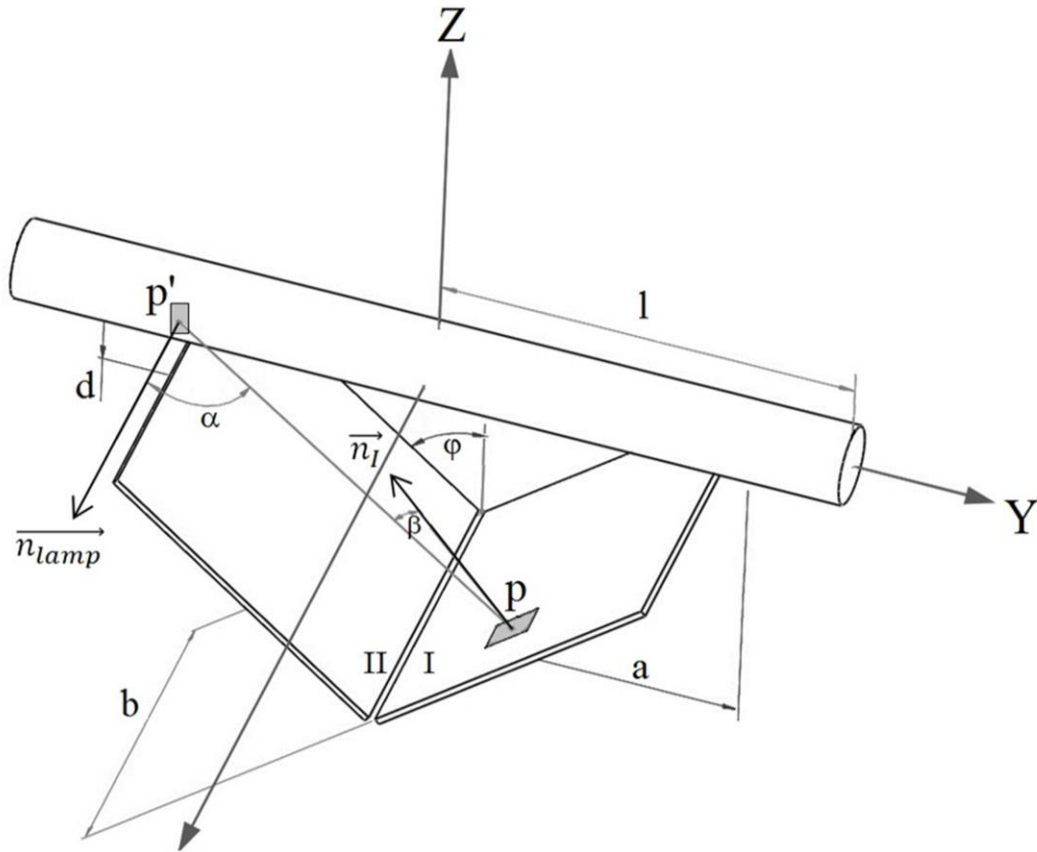


Figure 2.8 UV-C lamp irradiation coordinate system.

The lamp tube surface area is expressed as a parameter Equation (Figure 2.9). Any point P' on the tube has a coordinate: P' (Rcosθ, t, Rsinθ), where R is the radius of the tube cross section and t is the position of the point on the y-axis. Therefore, the lamp normal vector can be written as Equation (2.10):

$$\overrightarrow{n_{lamp}} = -(R \cos \theta)i - (R \sin \theta)k \quad (2.10)$$

For a random point P on the plate with known coordinates (m, n, q), the vector $\overrightarrow{pp'}$ becomes Equation (2.11):

$$\overrightarrow{pp'} = (R \cos \theta - m)i + (t - n)j + (R \sin \theta - q)k \quad (2.11)$$

The influenced differential cross section to the point can be found by examining the two angles θ1 and θ2, which are obtained by solving Equation (2.12):

$$\overrightarrow{n_{lamp}} \cdot \overrightarrow{pp'} = 0 \quad (2.12)$$

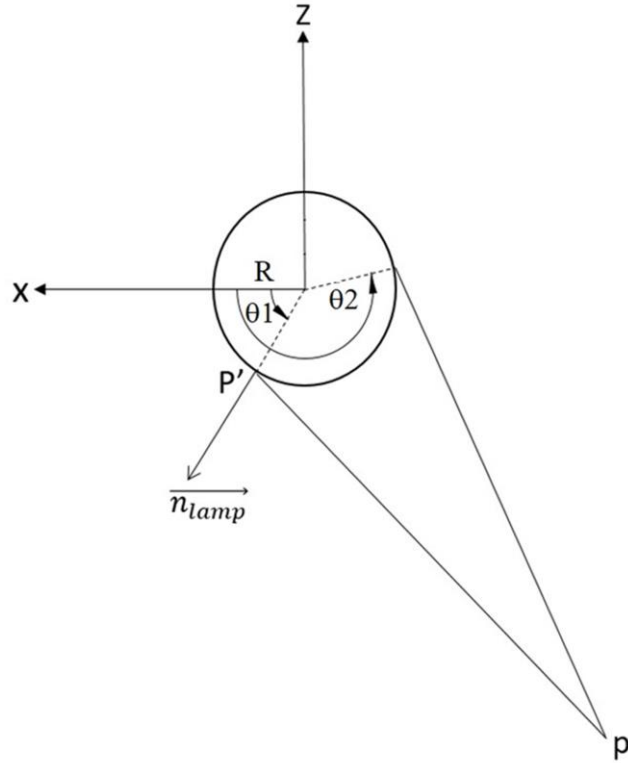


Figure 2.9 Cross section of a UV-C tube with projection to a point on the reactor plate.

By solving Equation (2.12), the boundary angles θ_1 and θ_2 can be expressed as Equation (2.13) and Equation (2.14):

$$\theta_1 = 2\left(\tan^{-1}\left(\frac{m - \sqrt{m^2 + q^2 - R^2}}{q + R}\right)\right) \quad (2.13)$$

$$\theta_2 = 2\left(\tan^{-1}\left(\frac{m + \sqrt{m^2 + q^2 - R^2}}{q + R}\right)\right) \quad (2.14)$$

Considering the P point coordinates (m, n, q) as known, then the lamp radius R , θ_1 and θ_2 become known values. The boundary of the t value is $(-1, 1)$ and, therefore, the boundary values

for the lamp surface integration can be determined, and Equation (2.8) can be rewritten as Equation (2.15):

$$I = a(\lambda) \frac{dP}{\pi^2} \int_{-l}^l \int_{\theta_1}^{\theta_2} \frac{\cos \alpha \cdot \cos \beta}{r^2} R d\theta dt \quad (2.15)$$

The other items in Equation (2.8) are cosine of vector angles (α and β), and vector modulus r , which can be determined from Equation (2.16), (2.17) and (2.18):

$$\cos \alpha = \frac{\vec{n}_{lamp} \cdot \vec{pp}'}{|\vec{n}_{lamp}| \cdot |\vec{pp}'|} \quad (2.16)$$

$$\cos \beta = \frac{\vec{n}_I \cdot \vec{pp}'}{|\vec{n}_I| \cdot |\vec{pp}'|} \quad (2.17)$$

$$r = |\vec{pp}'| = \sqrt{(R \cos \theta - m)^2 + (t - n)^2 + (R \sin \theta - q)^2} \quad (2.18)$$

By substituting Equations (2.13), (2.14), (2.16), (2.17) and (2.18) into Equation (2.15), and with the given values of the lamp and reactor plates, the light intensity at a specific point can be obtained. By integrating across the plate surface, the total absorbed power by one plate can be calculated and the intensity distribution across the surface can be plotted.

Power absorption by one single plate of the reactor can be expressed as Equation (2.19):

$$w = \frac{1}{\sin \varphi} \int_{-b}^b \int_0^a |I| dy dx \quad (2.19)$$

The numeric value of light intensity absorption was calculated using MATLAB[®], [73] in which the lamp surface was divided into 10^6 differential areas, and the modelled results were compared

to measurements made with a photo detector (Solarmeter[®] 8.0 UV-C, United States). Figure 2.10 shows the good agreement between simulated and actual measurements, which suggests that the diffuse emission theory is suitable to model the corrugated plate system.

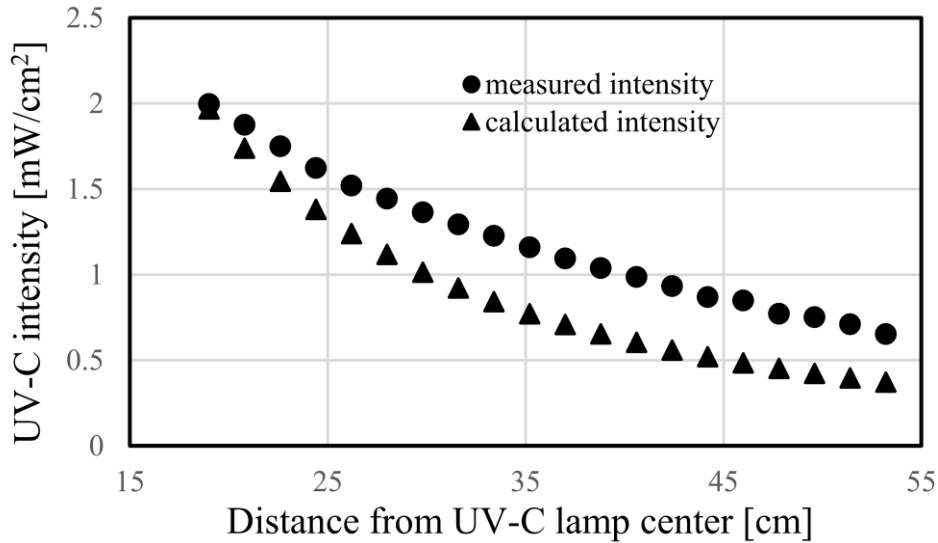


Figure 2.10 Calculated and measured light intensity.

The LASREA profile of each plate, which was divided into 27160 differential patches, was, therefore, plotted using (Figure 2.11). The top lighter sections are the closest points between the lamp tubes and the plate. Figure 2.11(a) shows the energy absorption profile of a reactor plate under one lamp (two tubes), with a distance of 1 cm to the top of the plate, and Figure 2.11(b) shows the energy absorption profile of a plate under two lamps (four tubes), with the same lamp to plate distance. The power absorbed is generally higher in Figure 2.11(b), due to the increase in incident energy.

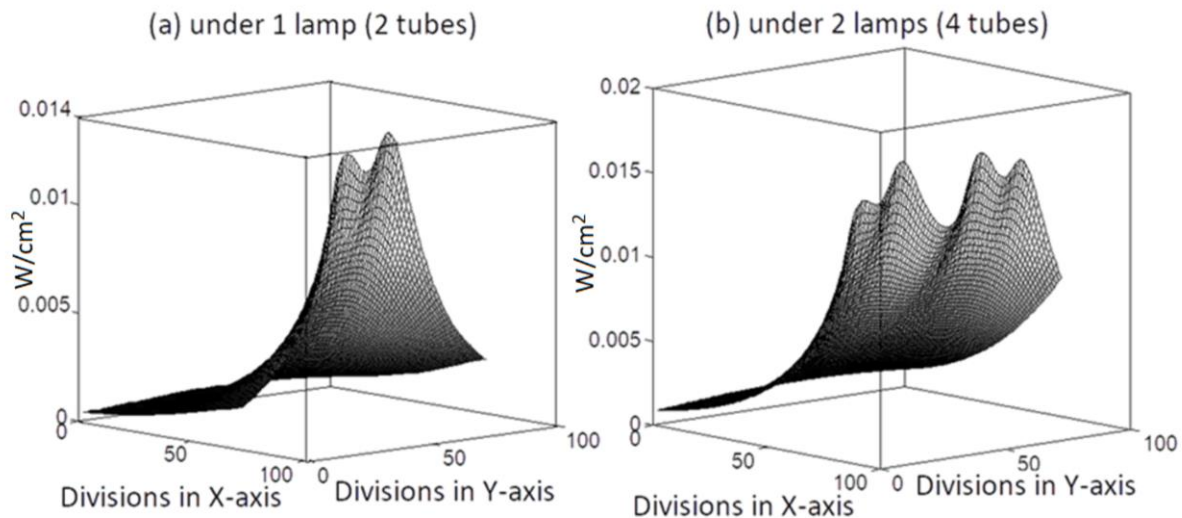


Figure 2.11 UV-C light intensity absorption profiles for each plate.

2.3.3.4 Effect of geometry

Compared to other types of photocatalytic reactors, the advantage of the corrugated plate configuration is that in a given illuminated area, more catalytic surface can be accommodated, and more photons may be captured. However, this type of configuration is likely to have a limit, as if too many surfaces are “crowded” together, light illumination may be blocked. Therefore, a comparison was made between corrugated reactors of different geometries, but with the same total coated area, reaction volume and illumination conditions (Figure 2.12). Individual plate size varied from 67.90 cm² (adjacent angle 36.7°) for an 8-plates reactor to 27.16 cm² (adjacent angle 31.4°) for a 20-plates reactor, and each reactor has a total coated area of 543.2 cm².

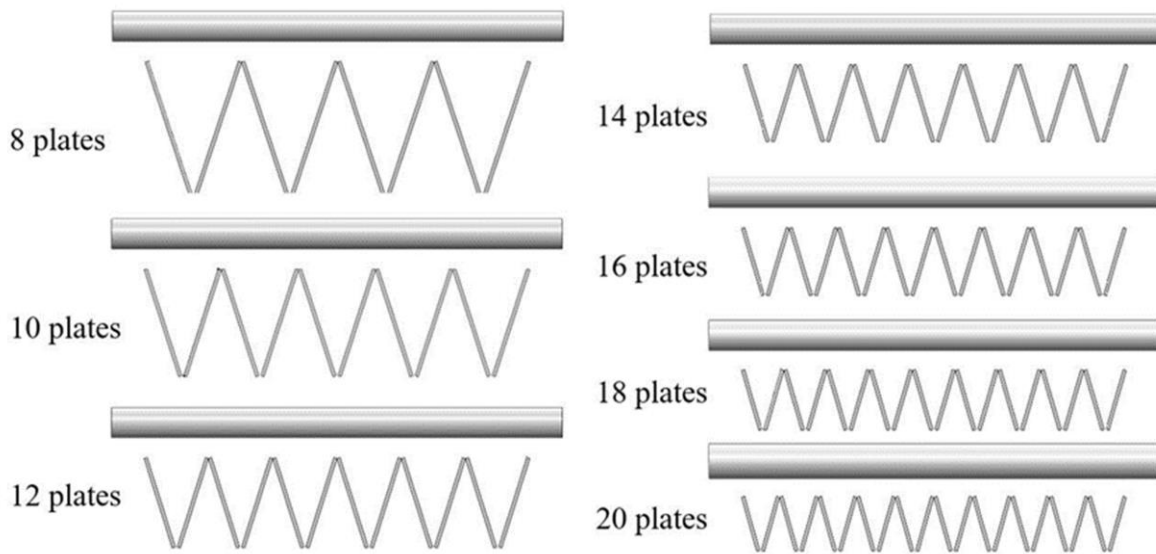


Figure 2.12 Reactor plate configurations with the same illuminated area.

By integrating across a plate surface using Equation (2.19), power absorption by each plate can be calculated. As shown in Figure 2.13, the reactor with the least number of plates, 8, had the most capacity to absorb light energy, which was 1.5 times more energy than the 20-plates reactor. Energy absorption with different lamp positions were also calculated, and the closer the lamp to the reactor, the more energy can be absorbed.

The illuminated lengths from the lamp are different at different reactor boundaries. However, the difference and resulted discrepancy are not significant. For example, to the layout (1 cm distance between lamp and the top of reactor plates), the projected illumination source length is less than 1 mm longer for the 8-plates reactor than the 20-plates one. If we made exactly the same illumination length by covering part of the light source, the difference of the total power

absorption for the 8-plates reactor is only 0.0034 W, which is less than 1% of the original value. When the light source is located further from the reactor, this will result in a bigger illumination difference, but due to the light intensity decay effect (light intensity has an inverse relationship with the square of the distance), the boundary issue still is not significant.

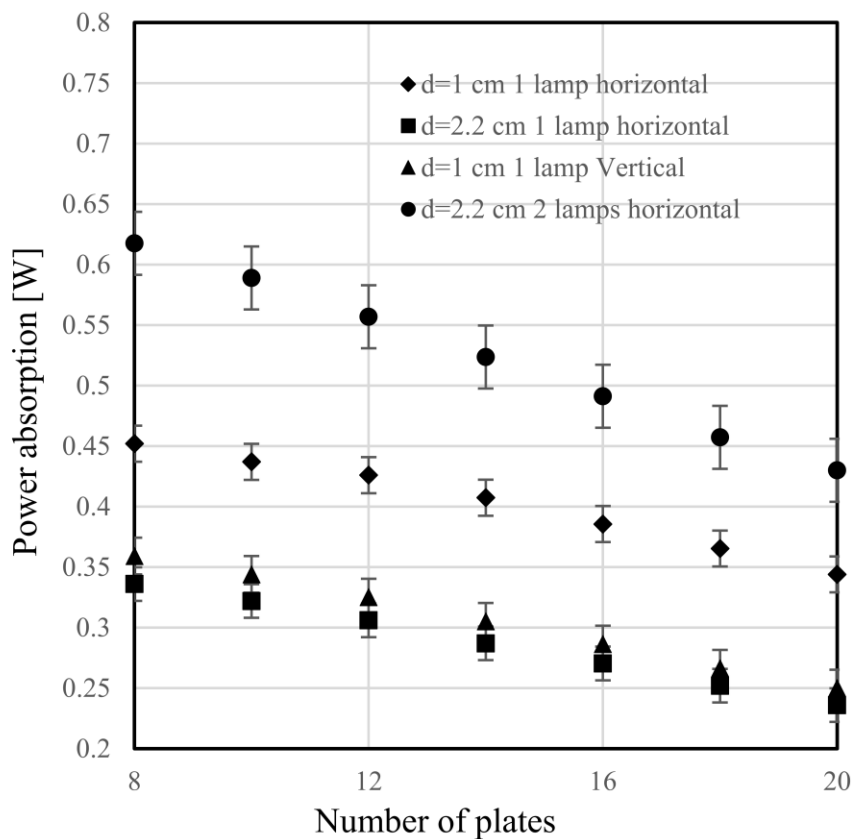


Figure 2.13 Absorbed power by reactors with different number of plates and light source.

2.3.3.5 Reactor performance

Apparent photonic efficiency, or photonic efficiency is one of the important parameters to evaluate the performance of a photocatalytic reactor, which is defined as Equation (2.20):^[12,61,74]

$$\eta = \frac{\text{molecules converted}}{\text{photons incident}} \quad (2.20)$$

where η is the photonic efficiency (in mole_{pollutant}/Einstein, or %); the molecule conversion can be defined as moles reacted, which is usually taken from the reaction rate when half of the concentration is degraded.^[12] One Einstein (or Einstein unit) is the energy per mole of photons carried by a beam of monochromatic light.^[75]

A high photocatalytic reaction rate does not necessarily mean high photonic efficiency. For example, MB degradation with a higher photocatalytic reaction rate under a high photon flux UV irradiation was reported, but this resulted in lower photonic efficiency compared to lower rate reaction under low UV irradiation.^[74] However, higher photonic efficiency with an AOP process shows effectiveness use of radiation by the reactor.^[13]

In calculating the apparent photonic efficiency for the first five minutes, over which the initial concentration had been degraded by half, the number of moles reacted can be determined. For a 36 W UV-C lamp with a distance of 2.2 cm to the top of the 16-plates reactor, the incident photonic energy for the first 5 minutes is 5.73×10^{-7} Einstein/s. Combining the molar reaction rate for the three initial concentrations (5, 11, and 20 mg/L) at a flowrate of 725 mg/L, the photonic efficiencies were 1.53, 2.80, and 2.83 % respectively.

Reported AOP reactors are all different in design and size and, therefore, it is difficult to make exact comparisons. Each reactor design has its own advantages and disadvantages, for example, some being easy to build and others designed to use natural sunlight.^[68] Table 2.2 shows photonic efficiency data of MB degradation obtained with different photocatalytic reactors found in the literature. For water treatment, a photocatalyst immobilized reactor is preferred, and the

reactor should have high photonic efficiency, less surface area or volume, be durable, and easy to maintain.

Table 2.2 Photonic efficiency of MB degradation with different reactors.

Reactor type	Description	Photonic Efficiency (%)
<i>Compound parabolic Collector</i> ^[68] (Nair et al., 2016)	A linear compound parabolic trough reactor with high acceptance angle can receive both UV and visible light. TiO ₂ was suspended in the reactor.	0.106
<i>Glass cylinder reactor</i> ^[74] (Zhang et al., 2012)	A comparative study between high photon flux photocatalytic process and routine low photon flux photocatalytic process for MB degradation has been made in aqueous solution in a glass cylinder reactor with suspended TiO ₂ powder.	2.43
<i>Glass cylinder reactor</i> ^[76] (Tschirch et al., 2008)	A glass cylinder reactor was used to examine the photocatalytic activity of transparent TiO ₂ coatings.	0.09
<i>Spinning disc reactor</i> ^[12] (Boiarkina et al., 2013)	A spinning disc reactor was investigated as a process intensification technology for photocatalysis, TiO ₂ was coated on the disc.	0.88
<i>16-plates corrugated reactor</i> (this work)	A photocatalytic reactor with TiO ₂ coated plates placed with an angle.	2.83

In comparison to other water treatment corrugated-type photocatalytic reactor designs,^[39-41] the system is stationary and relies on a pump to supply spray pipes to promote mass transfer over the

catalytic surfaces instead of rotating drums which are likely to consume more electrical energy. Previous reported work also employed UV-A or UV-B, whereas a UV-C light source was used in this study to allow for co-disinfection. Furthermore, with consideration for system maintenance, the TiO₂ immobilized plates could be reused, or easily removed and changed individually.

2.4 Conclusions

The described photocatalytic TiO₂ coated corrugated plate reactor demonstrated significant improvement over a corrugated system without coating for degrading methylene blue (MB) in solution. The reaction (degradation) rate was found to be affected by the plate configuration, initial MB concentration and fluid flow rate.

With a working volume of 250 mL of an 11 mg/L MB solution, 70 % of the MB was degraded within the first 10 minutes. This compared to a degradation rate of only 12 % for a corrugated reactor without a TiO₂.

As an advanced oxidation process, this type of photocatalytic water treatment also relies on mass transfer, including the adsorption and desorption of contaminants in the flow, and oxygen transport. Therefore, the combination of UV-C light distribution and plate geometry will have a major impact on degradation rates.

A local area specific rate of energy absorption (LASREA) model was, therefore, developed and it was found to correlate well with measured intensity values. Based on this model, with specified illumination conditions, reactor size, and photocatalytic coating surface area, the least corrugated configuration (i.e., the reactor with the least plates) absorbed the most photonic energy, even when taking into account boundary conditions.

Chapter 3 TiO₂ Based Nanopowder Coatings over Stainless Steel Plates for UV-C Photocatalytic Degradation of Methylene Blue

**Yongmei Jiao^a, Nathan Basiliko^a, A.Thomas Kovala^b, Jeffrey Shepherd^c, Helen Shang^a,
John Ashley Scott^{a*}**

^a Bharti School of Engineering, Laurentian University, Sudbury, Ontario, Canada

^b Northern Ontario School of Medicine, Sudbury, Ontario, Canada

^c Department of Chemistry and Biochemistry, Laurentian University, Sudbury, Ontario, Canada

* corresponding author: jascott@laurentian.ca

Published by *The Canadian Journal of Chemical Engineering*, Volume 98 Issue 3, March 2020,
Pages: 625-828

Immobilizing the photocatalyst in a water treatment process design is essential, but the immobilization method may affect the photoactivity of the photocatalyst. In this work, photocatalyst powders were successfully coated on 316L stainless steel plates by a novel brush coating method. Three combinations of photocatalyst mixtures (pure TiO₂ anatase, and anatase doped with WO₃, or TiO₂ rutile) were annealed at different temperatures between 460-540°C. The ~10 µm thick coatings demonstrated full plate coverage and strong adhesion and good durability. Surface roughness increased with annealing temperature. The doping and annealing process enabled bandgap reduction to the visible light spectrum for all coatings, with the smallest bandgap being 2.48 eV. Subsequent methylene blue degradation tests under UV-C showed that the coatings annealed in 460°C exhibited the best performance and with the highest degradation rate constant of 5.59 h⁻¹.

3.1 Introduction

Ultraviolet (UV) photocatalyst based advanced oxidation processes (AOPs), characterized as oxidization processes with hydroxyl radicals ($\text{OH}\cdot$), have gained significant attention in recent years. A hydroxyl radical is a powerful oxidizing agent that has potential to degrade non-biodegradable and toxic waterborne organic pollutants into nonharmful mineralized molecules such as CO_2 and H_2O .^[26,77]

The generation of hydroxyl radicals starts with the excitation of electrons in photocatalytic materials (mostly semiconductors). Upon receiving energy or being struck by photons, if there is a sufficient energy, it makes it possible for electrons on a photocatalytic material to move from the valence band to the conduction band, where both electric current and electron-hole (E-H) pairs form.^[21] Hydroxyl radicals can then be produced either through electrons reacting with oxygen, hydrogen ions, and hydrogen peroxide, or through reactions of the positive E-H pairs with water, oxygen, and hydroxyl ions.^[23]

A high E-H recombination rate is detrimental to AOP process, as this degrades photoelectric energy into heat.^[26] Doping metal or non-metal ions into the lattice of a photocatalyst, or mixing different forms of photocatalyst can slow down the E-H reunion, and thereby increase the reaction rate. Doping processes can also help reduce the bandgap of catalyst materials, and generally a shorter bandgap means less photonic energy required to trigger photocatalytic process.^[17]

Titanium dioxide (TiO_2) is the most popular catalyst in photocatalytic water treatment since it has high activity and is insoluble in water, as well as having low cost and toxicity. Mixing two

phases of TiO₂ (anatase and rutile) can help generate higher photocatalytic power.^[13,17]

Furthermore, tungsten trioxide (WO₃) is also an photocatalytic material with low solubility and low toxicity in water,^[78] which can be doped in other photocatalytic materials to improve reaction efficiency.^[79,80]

Catalyst immobilization on reactor surfaces is necessary when used in water treatment to avoid subsequent photocatalyst/water separation. Coating with different compositions of photocatalyst, substrates, as well as different coating methods are of interest.^[46,79,81]

Different coating methods would result in different morphologies of photocatalyst surface, which consequently influences photocatalytic activities.^[46] The crystal structure anatase is less stable than the rutile phase and the phase change from anatase to rutile has been reported to start between 400-450°C.^[82,83] In this work, a manual brush coating technique was adopted to coat fine TiO₂ powder onto 316L stainless steel plates, which were annealed at different temperatures. Coated plates were inspected with a scanning electron microscope (SEM), atomic force microscope (AFM), and X-ray diffractometer (XRD), as well as by bandgap, adhesion and water friction tests. A flow-through photocatalytic reactor system was set up to test the performance of the coated plates with a model compound methylene blue (MB) solution, which has a stable molecular structure,^[60] and often used in photocatalytic material and reactor tests.^[12,40,61-63]

3.2 Methodology

3.2.1 TiO₂ Coating on Stainless Steel Plates

The TiO₂ coating method used was developed from previously reported work,^[37] in which 304 stainless steel plates was brushed with 25 % (by volume) diluted HCl concentrate (12M), air-dried and oxidized in a muffled furnace for 2 hours. TiO₂ powder was suspended in 20 % (by volume) ethanol and brushed onto the oxidized steel plates, which were then annealed for 5 hours. After cooling they were cleaned with detergent and deionized (DI) water.

For the current work, we used four types of photocatalyst powder (supplied by Nanostructured & Amorphous Materials Inc., USA). They were anatase TiO₂ with an average particle size (APS) of 5 nm and 10 nm, named A5nm and A10nm respectively, below; anatase doped with 6 wt.% of WO₃ (APS 10 nm, named AW10nm), and rutile TiO₂ (APS 20 - 50 nm, named R20-50nm).

Three different powder mixtures were made (all the percentages are by weight, wt.%):

1. 60 % A5nm and 40 % A10nm - named "A".
2. 60 % A5nm, 17.63 % R20-50nm, and 22.37 % A10nm - named "AR".
3. 60 % A5nm and 40 % AW10nm - named "AW".

All mixtures were mixed with deionized water DI and HCl acid (1N) to make a slurry with a density of ~70 g/L and pH of ~1. Different powder mixtures were used to compare the dopant effect on pure anatase, whilst keeping other parameters the same (the powder containing WO₃ had an APS of 10 nm, whilst rutile had an APS of 20-50 nm).

The slurry mixture was brushed onto rectangular 316L stainless steel plates (9.7 cm × 3.5 cm × 0.13 cm), which were pre-sanded with a fine sanding block. A muffle furnace (Thermo

Scientific™ Thermolyne™ Benchtop) was preheated to the annealing temperatures (460, 500, or 540°C), and the plates baked for 1 to 5 minutes, before being taken out and brushed with another layer until the photocatalyst loading reached 65 to 70 mg per plate. The weight of the oxidized layer for each plate brushed with HCl solution and annealed at a temperature of 460, 500 or 540°C was found to be less than 1 mg, and therefore the weight gain from applying the coatings was essentially all photocatalyst.

The plates were then annealed for a further 2 hours. The plates were named with a combination of mixture name and temperature (e.g., AW460 means the plate was coated with 60 % A5nm and 40 % AW10nm annealed at 460°C). After the furnace was shut off, the plates were left to cool to room temperature (22°C), and then washed with dishwashing detergent, rinsed and left to dry.

The primary purpose of this work was to examine the effects of dopant and phase transformation with temperature change on photocatalyst coatings. The dopant addition was to reduce the bandgap of photocatalytic materials in order to absorb wide spectrum solar light.^[84] Doping 15 to 25 % rutile in anatase can promote effective charge separation in the photocatalytic process,^[84] whilst doping WO₃ in anatase can promote charge carrier transport.^[47]

As only AW10nm contains 6 % WO₃, to minimize the size influence and to keep a percentage of WO₃, 40 % of AW10nm was used to make a WO₃ content of 2.4 %. In literature, after a comparison of WO₃ addition from 1 to 50 %, it was found that 24 % WO₃ content in a TiO₂/WO₃ composite contributed the best photocatalytic activity in oxalic acid degradation.^[85]

It has been reported that in solution the anatase to rutile transformation starts after 400°C, whereas in a powder form it starts at ~500°C and full transformation to rutile occurs at 700°C.^[82]

In the AR mixture, 17.63 % rutile was used at the start in order to achieve a resulting rutile

portion of 20 – 25 % after annealing, which has been considered an optimum ratio for photocatalytic activity to occur.^[86]

3.2.2 Characterization of Physical Properties

The coatings bond to the stainless-steel plates was examined through a tape adhesion test. Scotch (Magic™) tape was applied on the surface and removed at a constant speed and consistent angle, with the coated plate weighed before and after applying the tape. The coated plates were also placed in a water container with water flow circulated by a peristaltic pump (Runze Fluid™, China) at a flowrate of 80 mL/min for 5 hours a day for 2 weeks. The plates were also weighed before and after this test.

Coating thickness, composition, and morphology were inspected with a scanning electron microscope (SEM, JEOL6400) with an attached energy-dispersive spectrometer (EDS, Oxford X-Max) detector, which was operated at 15 and 20 kV with a 1 nA beam current. The plates were cut into squares (1cm ×1 cm) and cleaned with water and ethanol and then coated with a thin carbon layer with a carbon coater (Edwards AUTO306). The top-view and side-view of the coatings were carried out with the SEM at 2000 times magnification. EDS (energy-dispersive spectrometer) analysis on the scanned images to analyze the coating's surface element composition.

The surface roughness of a coating was characterized with an atomic force microscope (AFM, Multimode). AFM images were scanned over areas of 25 μm × 25 μm, a rate of 1.49 Hz, and a resolution of 512×512 (i.e., over a scanned area, the probe scans in 512×512 steps). For each

type of coatings, three samples were scanned and the roughness average (R_a) determined as the arithmetic mean of the absolute values of the scanned surface peak heights^[87].

Compared to the other two forms of TiO_2 , anatase is less stable and is subjected to a structural change into rutile when the annealing temperature goes above $400^\circ C$.^[82,88] In the AOP process, higher photocatalytic reaction rates have been found with a doped photocatalyst.^[63] In this work, the rutile fraction, as weight percentage in the coated area, was analyzed with an X-ray diffractometer (XRD, SCINTAG XDS2000TM). The XRD scan was at a wavelength of 1.542 nm and a step size of 0.02° was used from 20° to 80° . The peak intensities used to evaluate the rutile ratio were the heights after baseline corrections (25.3° for anatase and 27.44° for rutile). The rutile weight fraction was evaluated from Equation (3.1):^[89]

$$X_R = \left(1 + 0.8 \frac{I_A}{I_R}\right)^{-1} \quad (3.1)$$

where X_R is weight fraction of rutile, and I_A and I_R are the peak intensities for anatase and rutile respectively.

As the portion of WO_3 powder was only 2.4 wt.% and remains in its orthorhombic structure between 400 and $600^\circ C$,^[90] the crystal structure of on the resulted coatings was not inspected in this work.

3.2.3 Bandgap Energy Evaluating of Coatings

An important role of dopants is to reduce bandgap energy of photocatalysts and thereby enable more reactions to occur.^[88] Band gaps of the coated thin films may not be the same as those of

the powder form, and, therefore, we analysed the bandgap in a powder form by stripping the coating from the plates.

The coatings were scratched carefully from the plates (keeping the grain size) and mixed with DI water, and transferred into a microplate reader (Synergy H1 BioTek[®]) at a solid density of ~5 mg/mL. Each sample was scanned over a UV/Vis spectrum range of 230 nm to 700 nm at 10 nm steps (Figure 3.1a and Figure 3.1b). The 4 photocatalyst powders used, along with an anatase sample with an APS of 25 nm (“A25nm”, Sigma-Aldrich, USA) were also analyzed in order to compare results with literature values.

The UV/Vis spectrum absorbance of the coatings was plotted against the corresponding wavelengths and the bandgap values calculated using the spectrum cut-off wavelengths, which were plotted as shown in Figure 3.1c and Figure 3.1d.

Band gap energies were then calculated with the cut-off wavelengths by using Equation (3.2):^[91,92]

$$\text{Band Gap Energy } (E) = \frac{h \cdot C}{\lambda} \quad (3.2)$$

where h is the Planks constant (6.626×10^{-34} J·S); C , light velocity (3.0×10^8 m/s) and λ the cut-off wavelength in nm ($1 \text{ eV} = 1.6 \times 10^{-19}$ J).

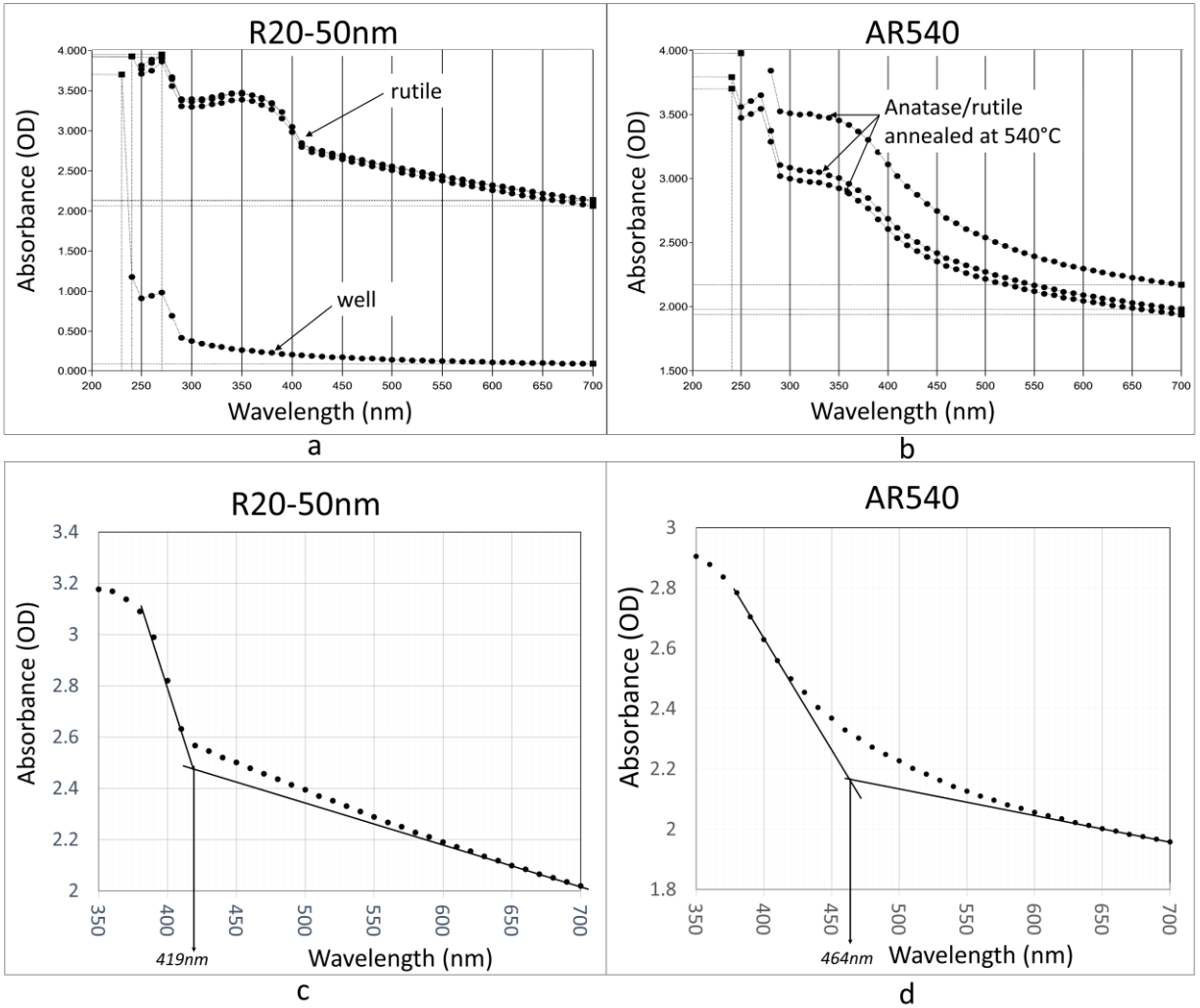


Figure 3.1 Determining the cut-off wavelength of photocatalyst powder and coatings.

3.2.4 Photocatalytic Activity in an UV-C/Photocatalyst Reactor

To compare the activity of the different coatings, methylene blue (MB) degradation tests were conducted in a UV-C irradiated reactor system (Figure 3.2) located in a dark chamber. A two bulb UV-C lamp (Odyssey[®], China) with a 36-watt power output produced monochromatic

irradiation at a wavelength of 254 nm. The two tubes, separated by 0.125 cm, had a length of 38 cm and diameter of 1.675 cm.

Before tests, 200 mL MB solution with a concentration of 11 mg/L was put into the system for to allow for any surface adsorption. When sampling, three samples (200 μ L each) were taken and examined with a microplate reader at a wavelength of 661 nm (Synergy H1 BioTek[®]). After 10 minutes no concentration change was observed and ~6 % (by concentration) MB was absorbed in the system.

The coated plates were soaked in DI water for 15 minutes before being put into the reactor system. In each test, three adjacent plates with the same type of coating were used with 100 mL MB solution (11 mg/L) circulated. The percentage MB degradation after 15 minutes were used to compare efficiencies when the concentrations were reduced more than 50 %. During the tests, pH and dissolved oxygen (DO) levels were monitored.

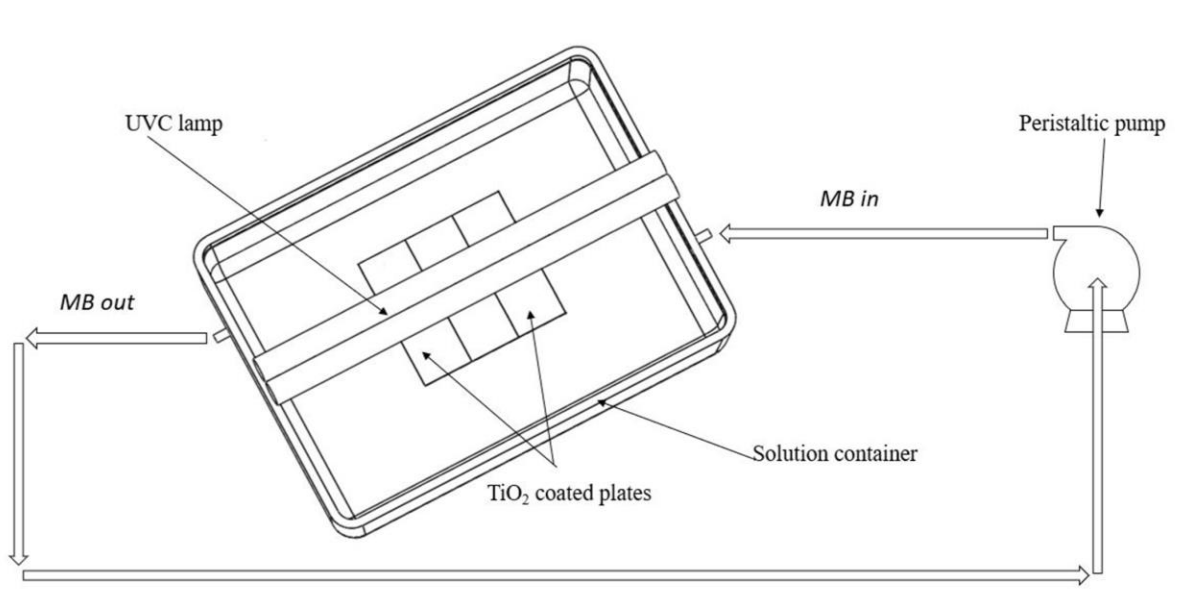


Figure 3.2 The UV-C photocatalytic water treatment system.

3.3 Results and Discussions

3.3.1 Adhesion Test and Durability

The weights remained constant before and after applying the tape for plates annealed at different temperatures, and surface uniformity after tape testing was also observed. No weight loss was also observed for plates placed subject to circulating water for 2 weeks, which again demonstrated good coating durability.

3.3.2 Coating Thickness and Coverage

With a TiO₂ loading of 65–70 mg per plate ($2.1 \pm 0.1 \text{ mg/cm}^2$), from an SEM of the side-view (Figure 3.3), the coating thickness was found to be $\sim 10 \text{ }\mu\text{m}$ for coatings annealed at 460 and 540°C, which indicated that annealing temperature did not have much influence to the coating thickness. It has been reported that a minimum coating thickness of $4.1 \text{ }\mu\text{m}$ is required to block UV-C (wavelength 254 nm) penetration into a TiO₂.^[93] Due to of the agglomeration tendency of TiO₂ at high annealing temperatures,^[88] the coating can be thicker, although increased thickness may not contribute to greater degradation of pollutants due to the surface reaction nature of photocatalytic reactions.^[94]

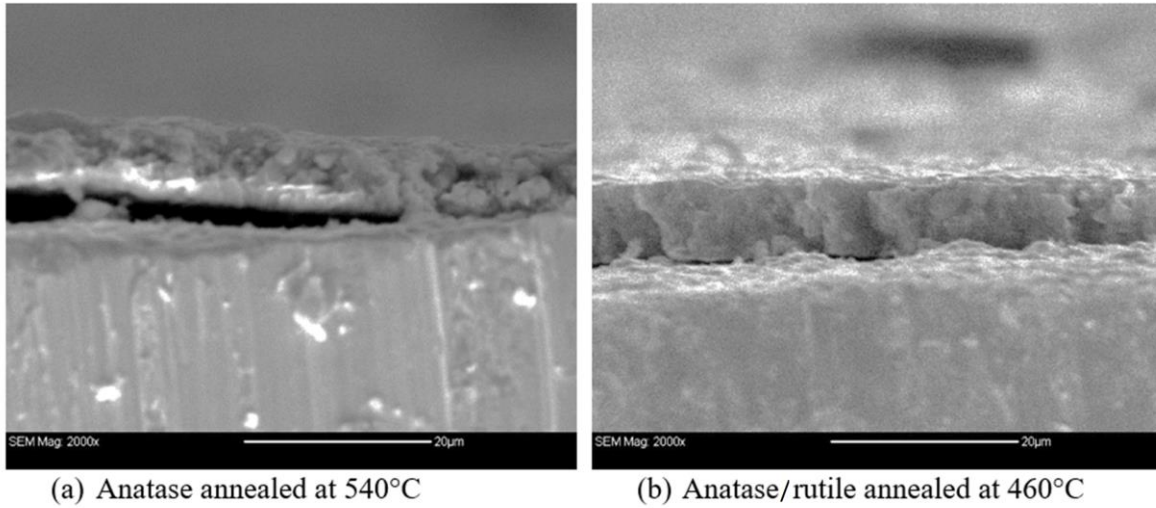


Figure 3.3 TiO₂ film thickness.

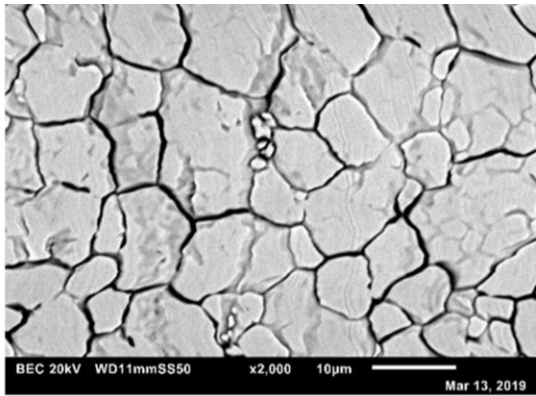
The coatings were also analyzed with SEM-EDS for surface element composition (Table 3.1), and excessive carbon was detected due to the pre-coating used prior to SEM imaging. The detected composition of iron was found to be less than 1.6 % by weight, compared to the 62-72 % content of 316L steel,^[95] which indicates a comprehensive coating coverage over the plate. The residue calcium and sulphur might arise from impurity of the coating slurry and a little iron and chromium may be the result of oxidization of the stainless steel with the dilute HCl solution or relatively uneven coverage of coatings. As there was no chlorine detected, this suggests that intermediate iron salts were converted to oxide.

Table 3.1 Composition (wt.%) comparison between TiO₂ coated and non-coated 316L steel plates

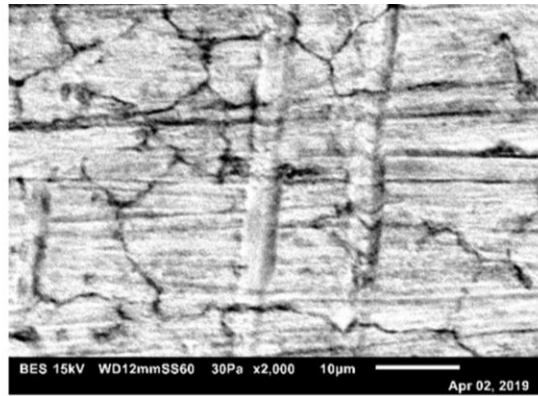
		C	O	Mn	Si	P	S	Ca	Ti	Cr	Mo	Ni	N	Fe
Coatings	Min	8.9	37.4	0.0	0.0	0.0	0.0	0.0	48.8	0.0	0.0	0.0	0.0	0.8
	Max	10.4	39.8	0.0	0.0	0.0	0.5	0.3	51.9	0.3	0.0	0.0	0.0	1.6
316L	Min	0.0	0.0	0.0	0.0	0.0	0.0	0.0	0.0	16.0	2.0	10.0	0.0	72.0
	Max	0.0	0.0	2.0	0.8	0.1	0.0	0.0	0.0	18.0	3.0	14.0	0.1	62.0

3.3.3 Coating Roughness

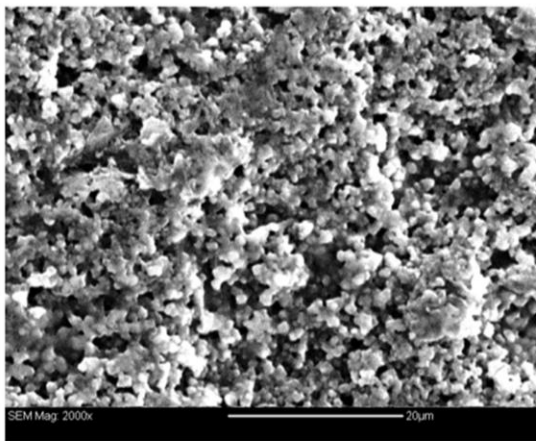
Figure 3.4a is an SEM of an untreated steel plate and Figure 3.4b a plate that was sanded, coated with HCL solution (pH 1), and annealed at 460°C. The untreated stainless plate can be seen to have grain boundaries and the oxidized plate has visually more cracks, which increased the plate surface area for the photocatalyst to be adhered to. Plates with coatings (65-70 mg/cm²) were also inspected with SEM, and coating morphology was found to change with annealing temperature. Figure 3.4c and Figure 3.4e show pure anatase coatings annealed at 460°C and 540°C, respectively, whilst Figure 3.4d and Figure 3.4f are of anatase with rutile annealed at 460°C and 540°C. For both types of coating, those annealed at 460°C were relatively smooth compared to those at 540°C.



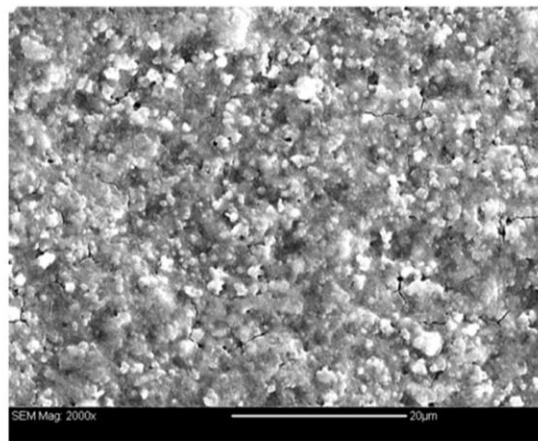
a. Bare 316L steel plate surface



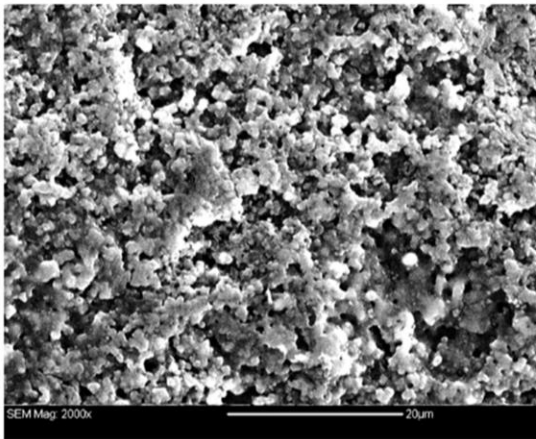
b. 316L plate sanded, oxidized and annealed at 460°C



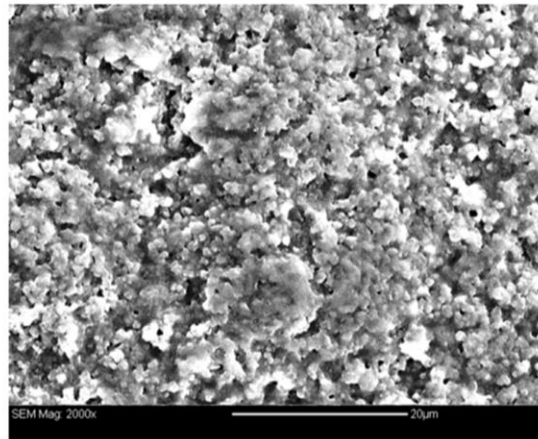
c. Anatase annealed at 460°C



d. Anatase/rutile annealed at 460°C



e. Anatase annealed at 540°C



f. Anatase/rutile annealed at 540°C

Figure 3.4 SEM images of plate surfaces.

SEM images can help visualize the morphology of the coatings, whilst AFM scans can characterize the surface roughness by determining R_a , as a roughness average (in nm). For example, the AFM image in Figure 3.5a. is of a fine sanded polished stainless-steel surface and that in Figure 3.5b. of an anatase coating annealed at 540°C. The stainless-steel plate had an R_a of 95 nm and the anatase coated plate was much rougher with an R_a of 582 nm.

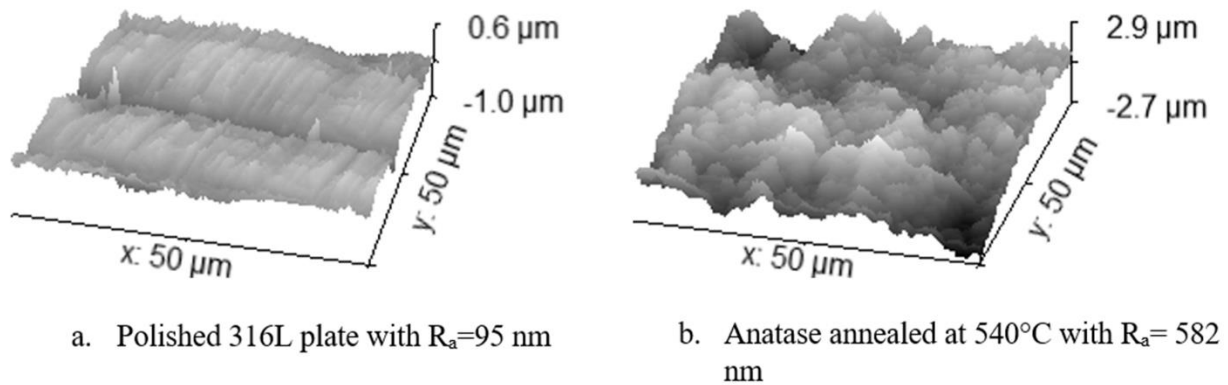


Figure 3.5 AFM images of plate surfaces.

Figure 3.6 shows the relationship between coating annealing temperature (460 to 540°C) and coating roughness. The results indicate that higher roughness resulted from a higher annealing temperature. As mentioned previously, the average particle size distributions of the coating powders prior to use are different. The mixture anatase and rutile (AR) is coarsest because of the 17.63 wt.% rutile portion (APS 20-50 nm). Whereas pure anatase (A) and WO_3 doped anatase (AW) resulted in a powder mixture with the same texture. This explains why at the lower temperature (460°C), the A and AW coatings are almost the same and notably smoother than AR.

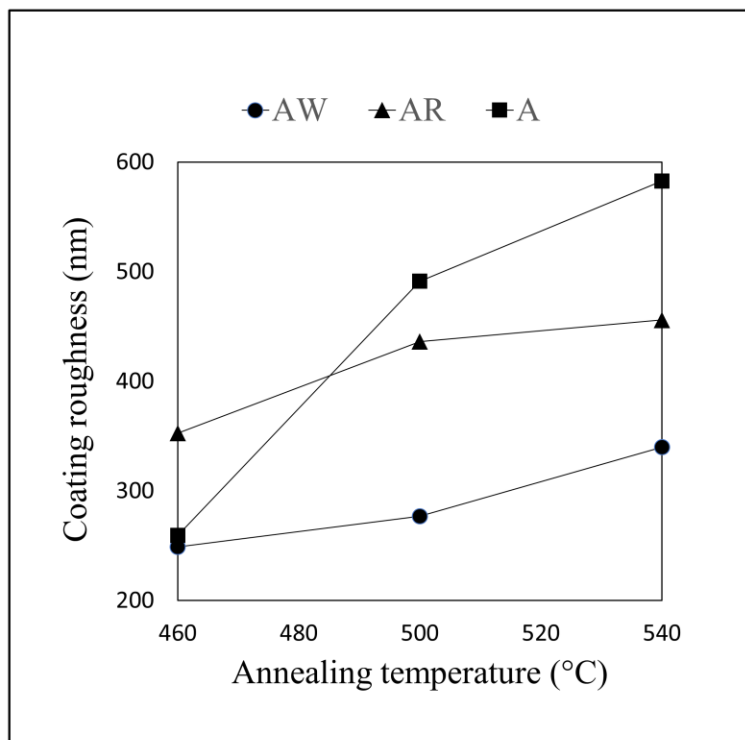


Figure 3.6 Annealing temperature vs. coating roughness.

Roughness increased with annealing temperatures for all three coatings (Figure 3.6). However, the roughness change rates were different, with a higher change found with the pure anatase coating than with the doped coatings (AW and AR). This suggests that the dopants helped stabilize the coating's microstructure, which may be also a result of phase change in the coating materials because of the dopants, as shown by XRD results in next section.

A tendency for agglomeration of anatase (lower surface area) during annealing aimed at rutile transformation at a high temperature (>500 °C) was reported, and which led to negligible transformation of rutile.^[46] The annealing temperatures used (460 to 540°C), have been reported as in the low temperate range for anatase to have a phase change.^[82] The formation of rougher

surface at 540°C may, therefore, be that the grain growth or agglomeration rate was higher than the rutile crystallization rate, and causes a larger grain size.

A higher roughness can lead to a greater adhesive strength of a surface, and adherence is a chemical-physical phenomenon responsible for the union of two surfaces when contracted,^[87] A higher wettability resulting from a higher roughness of TiO₂ film has been also reported.^[89]

UV/photocatalyst based AOPs rely on photonic energy and a photocatalytic material,^[17] and with the more energy the material absorbs, the more reactions may occur. Energy absorption also relies on reactor geometry and catalyst material properties.^[13,37,38] Due to the diffuse emission pattern of UV irradiation,^[71] light energy absorption will be also influenced by reactor geometries,^[39,41,54] and it can be deduced that light energy absorption may be also influenced by surface morphology as excessive roughness of the coated surface may impede light energy absorption.

In this work the roughness, R_a , was in a range between ~200 to ~600 nm. Figure 3.7a is of derived from an AFM scan of a relatively smooth coating (from an AW460 sample), and shows a narrow, small height distribution (normalisation of height densities, ρ , in μm^{-1} , are plotted against the distance below or above the average peak height, z , in μm). On the other hand in Figure 3.7b (from an A540 sample), the height distribution is larger and broader, and irradiated UV light may be blocked in the valley areas and result in less energy absorption due to the diffusive emission property of UV light.^[71] Note that the maximum roughness of this AFM is 6 μm .

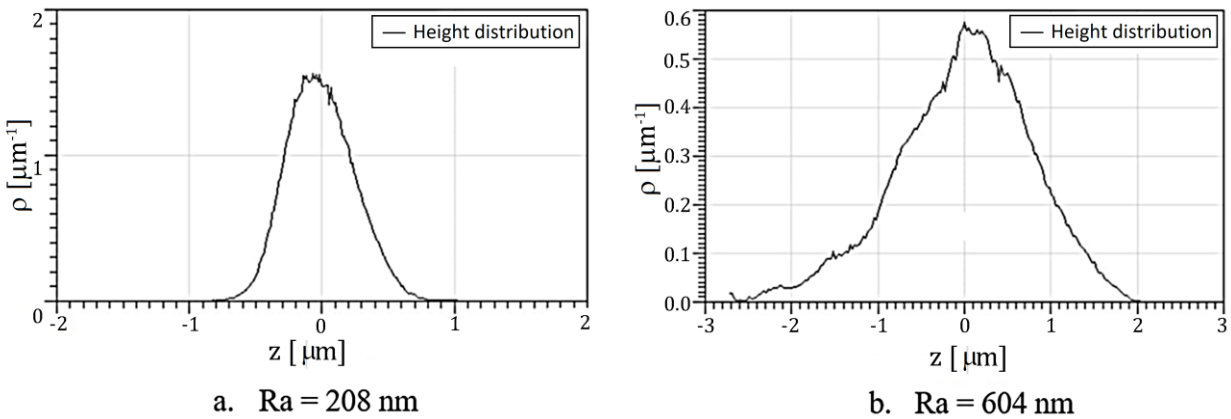


Figure 3.7 Height distribution of scanned peaks (valleys) on coatings.

The coated rough surfaces may have micro geometry effects on energy absorption in the same way as a corrugated plate reactor described in previous work,^[37] in which a broader-angled corrugated plate reactor absorbed more energy than a reactor with a sharper angle under the same irradiation condition of UV-C light.

UV/photocatalyst assisted AOP is a heterogeneous photocatalysis process, which relies on five independent steps: (i) transportation of reactants; (ii) reactants adsorption on catalyst (iii) reaction itself; (iv) desorption of the products; and (v) and the removal of the products.^[26] As the adsorption step is vital, research has been focused on how to increase the photocatalyst surface area.^[81,96,97] Higher surface roughness, or increased surface wettability may help,^[89] but may also result in adverse microgeometry or morphology for light absorption, since UV lights have a diffusive emission character (i.e., direction and strength change with distances).^[71]

3.3.4 XRD Assessment of the Rutile Ratio of the Coating

Figure 3.8 shows XRD images for the anatase/rutile (AR) mixed coating annealed at different temperatures (460, 500 and 560°C). The coating before annealing was also examined at 22°C (sample AR@22°C). A and R are the characteristic absorption peaks for anatase (25.3°) and rutile (27.44°) respectively. After baseline correction, the peak intensity values, I_A and I_R were substituted in Equation (3.1) to find out the rutile weight fraction, X_R .

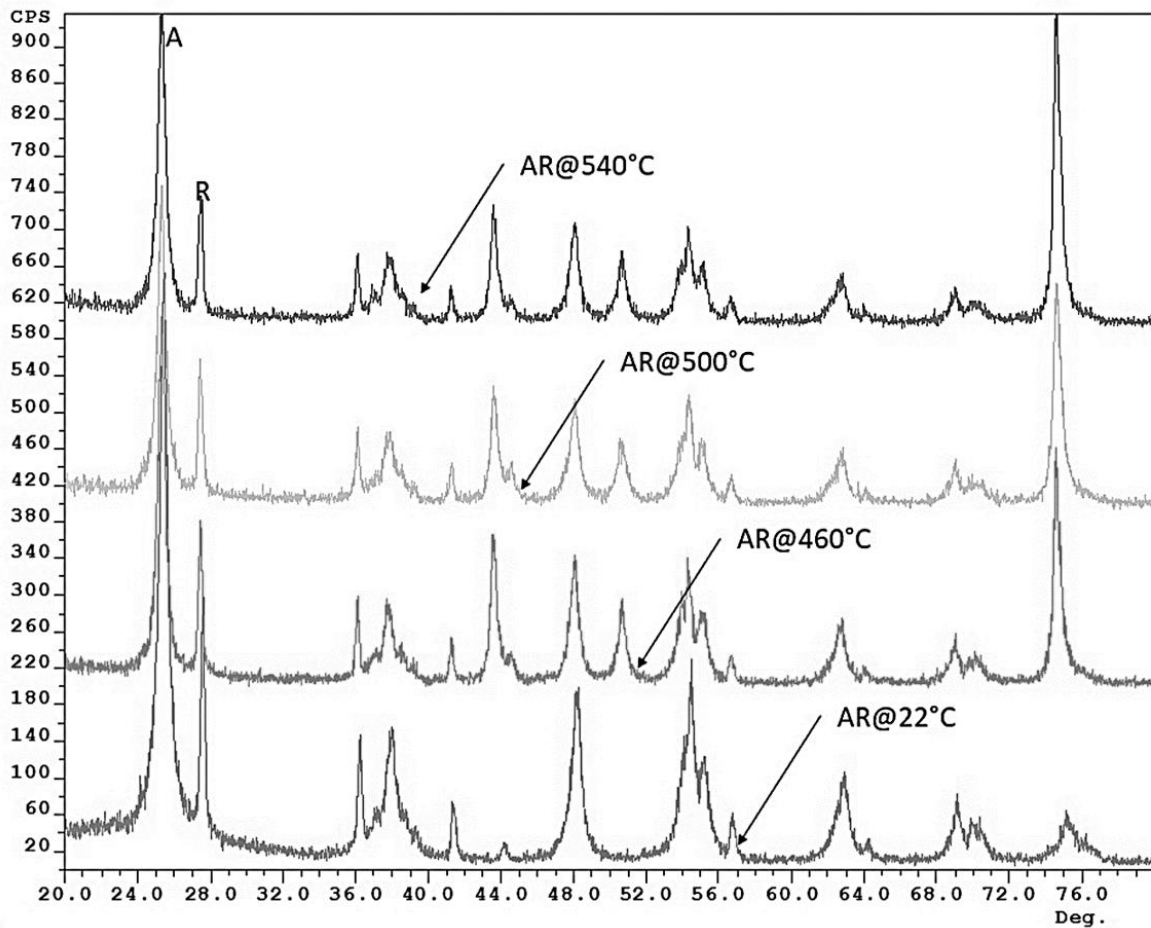


Figure 3.8 Anatase/rutile mixed coating XRD curves before annealing and after different annealing temperatures.

Table 3.2 shows the rutile weight fractions of the various coatings before and after annealing.

Before annealing, there was no rutile in the WO_3 doped anatase (AW) and pure anatase (A)

coatings, and the rutile doped coating (AR) contained 17.63 % (by weight). After annealing, at the lowest temperature (460°C), there was the biggest increase in rutile for the AW and AR coatings.

Table 3.2 Rutile wt.% at different annealing temperatures

Annealing temperature	AW	AR	A
540°C	0.00	23.47	0.81
500°C	0.28	27.58	0.07
460°C	2.92	25.27	1.76
22°C	0.00	17.63	0.00

A synergetic effect was reported with the commercial photocatalyst powder Degussa P25, and other TiO₂ powder combinations that contain 80-85 % anatase and the rest rutile,^[81,98] which was the reason for rutile dopant addition. However, the polymorph composition of TiO₂ after coating and annealing processes is rarely reported. Due to the different coating methods and the intermediate physical and chemical reactions, the subsequent changes of morphology and polymorph composition of the photocatalyst material may influence the photocatalytic activities.

The observed nonlinearity might be the result of a non-uniform coating slurry due to the different particle sizes and the suspension gradient of the powder particles. There are also instrumental issues may contribute to inaccurate XRD imaging^[87] such as the rutile may be presented in a preferred (unfavorable) orientation, or rutile crystallites may be encapsulated or covered by anatase. Despite any error that may occur in XRD imaging, and according to the bandgap energy data (next section) obtained for the coatings, rutile formation against temperature change should be linear and in a downward trend with a temperature rise.

The downward trend of rutile formation with increased temperature may be a result of the parameters used in this work. After being brushed with photocatalyst slurry, the plates were transferred into the preheated muffle furnace operated over a temperature range of 460 to 540°C, which is a range that is relatively low for anatase/rutile transformation (ART) in the powder form.^[82] The powder ART often accompanies agglomeration or grain growth of anatase with crystallization of rutile.^[81,98] An explanation of this result would be that at 540°C, anatase grain grew faster than the crystallization of rutile and when larger-sized anatase formed, it caused a lower heat diffusion rate to the center of the grains which slowed ART. Whereas at 460°C, the rates of grain growth and ART were relatively even, which resulted in a higher content of rutile.

The ART process is based on nucleation and growth, which depends on many variables such as the sample preparation method, heat flow and dopants.^[88] For the anatase/rutile mixture, the larger portion (17.63 % by weight) dopant rutile is likely to contribute to crystallization of rutile^[99], which results in greater rutile generation. On the other hand, a small portion of dopant (2.4 % by weight WO₃) and with the small percentage resulting rutile portion (2.92 %), it is hard to tell if WO₃ contributed significantly to ART. The reported higher tendency for anatase agglomeration at high temperature (>500 °C) resulting in a low yield of rutile,^[46] is similar to what was observed in this work.

3.3.5 Bandgap Energy of Coatings

Table 3.3 lists the bandgap energy values obtained from the photocatalysts before and after coating. The bandgap values obtained from the rutile powder (APS 20-50 nm) and different

anatase powders are close to reported values 2.98 and 3.05 eV(A25nm).^[45] Comparing anatase powders, A25nm, the one with largest particle size, has the smallest value, and anatase doped with 6 wt.% WO₃ (AW10nm) has a lower bandgap than anatase alone (A10nm).

The bandgaps for the coatings were lower than pure powder. For pure anatase and anatase/rutile coatings, the bandgaps were lowest at the lowest annealing temperature (460°C), and the doping of rutile again resulted in a lower bandgap than pure anatase. The bandgaps for the coatings doped with WO₃ at four annealing temperatures (460, 500, 540 and 560°C) were also compared, and there was a slightly downward trend in the range of 460-540°C, with a bigger reduction in 560°C, although the bandgap was larger at 460°C than that of pure anatase or anatase/rutile mixed coatings.

Table 3.3 Bandgap energy obtained from photocatalyst powder before and after coating

Sample	λ (nm)	Band gap (eV)	Sample	λ (nm)	Band gap (eV)
R20-50nm	419	2.97	AR460	502	2.48
AW10nm	380	3.27	AR500	492	2.53
A5nm	337	3.69	AR540	464	2.68
A10nm	375	3.32			
A25nm	410	3.03	A460	492	2.53
			A500	480	2.59
AW460	440	2.83	A540	475	2.62
AW500	442	2.81			
AW540	445	2.79			
AW560	475	2.62			

Note: A, anatase; W, WO₃; and R, rutile; 1 eV=1.6×10⁻¹⁹ J.

3.3.6 MB Degradation Using Plates with Different Coatings

Using the system illustrated in Figure 3.2, methylene blue (MB) solutions with an initial concentration of 11 mg/L were used to evaluate the photocatalytic degradation activity of no plates present, as well as plates with and without with the various coatings.

For the runs conducted without any plates, the average MB degradation after 15 minutes was 6.7 % (by MB concentration) and similar to the 7 % recorded with three uncoated plates present.

With the three types of coated plates, MB degradation after 15 minutes increased to at least 57 % (Figure 3.9). The coatings annealed at 460°C demonstrated the best performance, with more than 74 % MB degradation. All three coatings showed a downward trend in degradation rates with rising annealing temperature. After each reaction, solution pH values generally increased 0.2 to 0.3 and dissolved oxygen decreased by 0.7 to 1.4 mg/L.

Degradation tests were also carried out on AW560, a coating with anatase and WO₃ slurry annealed at 560°C, but the 15-minute degradation was 64 %, which was lower than AW540. Therefore, higher temperatures were not considered in this work.

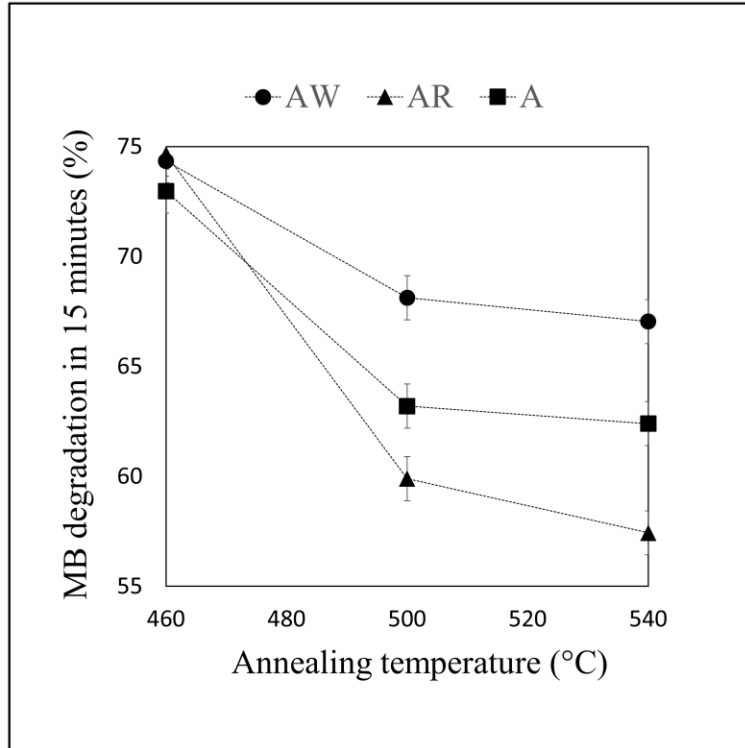


Figure 3.9 Methylene blue degradation vs. plate annealing temperature.

By comparing Figure 3.6 and Figure 3.9, it can be seen that the trends are almost opposite for each coating type, which suggests that increased surface roughness had a negative influence on photocatalytic activity. Although higher degradation rates of dyes on rougher photocatalytic surfaces have been reported elsewhere, the magnitude of roughness was different. The surface roughness resulted from our coating methods is 10-100 times larger than those reported.^[89,90] The high roughness of the coating may influence UV photonic energy absorption.

MB photocatalytic degradation follows the Langmuir-Hinshelwood isotherm, which can when the initial concentration (C_0) is low, be expressed as pseudo-first order kinetics as given in Equation (3.3):^[80,98]

$$\ln\left(\frac{C_0}{C}\right) = Kt \quad (3.3)$$

where C is the concentration of MB and K is the rate constant. By plotting $\ln(C_0/C)$ against time t, K can be then obtained.

Figure 3.10 shows MB degradation rate constants obtained with different coatings, with the highest rate constant being 5.59 h^{-1} . Due to different experimental conditions used by other researchers, MB degradation rates are hard to compare, but the value obtained in this work is higher than other reported rate constants for MB degradation with different coating and irradiation conditions:

- TiO_2 coated 16-plate reactor:^[37] 4.55 h^{-1} , for 250 mL 11 mg/L MB under UV-C (254 nm).
- A coating with optimized anatase/rutile ratio,^[98] 0.071 h^{-1} , for 30 mL 4 μM MB under UVA (365 nm).
- A TiO_2 transparent free standing coating,^[100] 0.046 min^{-1} (2.76 h^{-1}), for 10 mg/mL 10 mL MB under UVA (365 nm) black-light tube.
- A TiO_2 coated spin disc reactor,^[54] 0.0003 s^{-1} (1.08 h^{-1}), for 550 mL of 8 mg/L MB under UV-C (254 nm).
- A TiO_2 coated membrane,^[46] 0.0607 min^{-1} (3.642 h^{-1}), for 4 mL of 20 μM MB under a sunlamp (UVA or UVB).

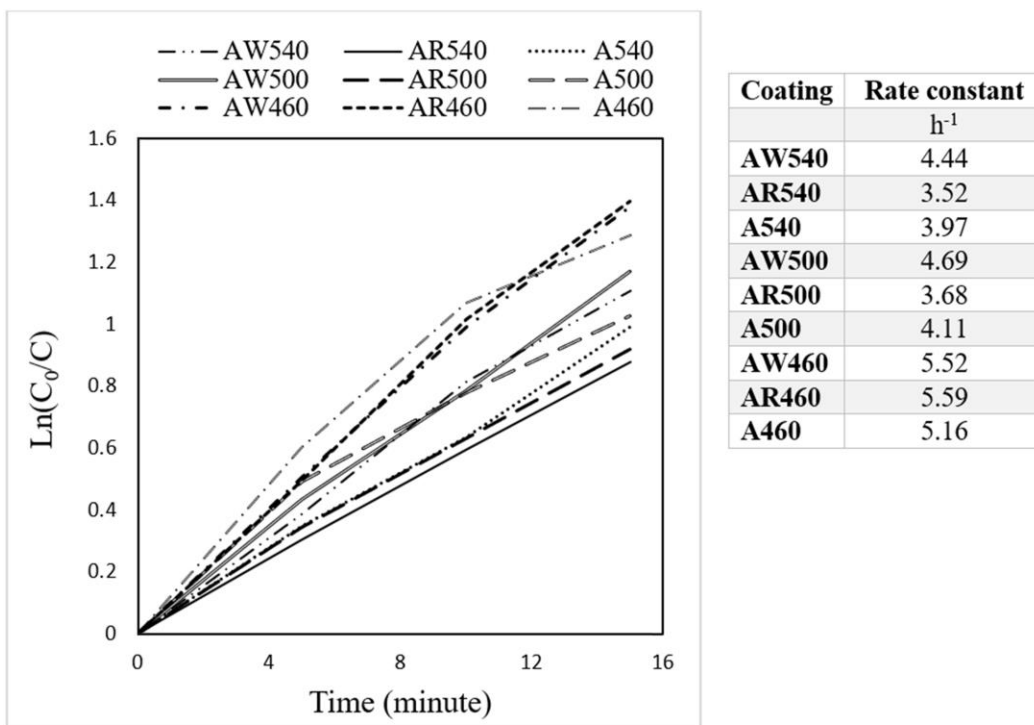


Figure 3.10 Methylene blue degradation rate constants with different coatings.

3.3.7 Coating Parameter Analysis

The immobilized photocatalyst on the steel substrate and the annealing temperature range that was used not only provided ART but also enhanced bandgap reduction as well. The bandgaps for coatings doped with WO₃, which had the biggest reduction at 560°C, were almost constant within the annealing temperature range (460°C-540°C). However, the bandgap for pure anatase was comparable with rutile doped coatings even though the latter almost had the reported ideal anatase/rutile ratio.^[88]

Surface roughness was considered to enhance surface wettability during a photocatalytic process.^[89] However, excessive roughness may result in adverse microgeometry or morphology

for light absorption as UV lights have a diffusive emission character (i.e., direction and strength change with distance).^[71] For a photocatalytic reaction, energy absorption is very important since it is related to the reaction step in a heterogenous photocatalysis process.^[26] For example, WO₃ doped coatings had similar bandgaps, but different roughness and the higher roughness corresponded to lower photodegradation of MB. The slightly reduced bandgap did not provide a significant contribution to the UV-C degradation process.

A reduced bandgap is desired in order to absorb a broader spectrum from solar light, but the monochromic UV-C light used in the MB degradation tests may be less impacted. In these experiments, bandgap theory may not be very fit to the results, since here UV-C irradiation was applied.

At an annealing temperature of 540°C, there were relatively close bandgap values, but MB degradation rates were quite different for the various types of coatings. Anatase had the roughest surface, but the degradation rate was higher than the anatase/rutile coating, but it was WO₃ doped coating that was the best performer (despite the relatively larger bandgap). Pure anatase has been characterized to have a high surface area, which promotes more charge carrier generation and slower charge carrier recombination.^[88] Doping rutile in anatase can promote effective charge separation;^[84] whilst doping WO₃ in anatase could promote charge carrier transport.^[47]

Whereas, with an annealing temperature of 460°C, despite different bandgaps and surface roughness, MB degradation rates were close. This indicates that the resulted bandgap difference did not make a difference with monochromatic UV-C irradiation. For pure anatase and WO₃ doped anatase coatings, with a similar roughness, the strength of charge carrier generation and

transportation was comparable and both higher than at a higher temperature. For anatase/rutile coating, the stronger charge carrier separation ability offset the less advantageous morphology and presented comparable photocatalytic activity.

3.4 Conclusion

Acidic TiO₂ anatase and WO₃ and TiO₂ rutile doped anatase slurries were successfully coated onto 316L stainless steel plates by brush coating and annealing at 460, 500, and 540°C. The coatings were ~10 μm thick and fully covered the plates, and they demonstrated strong adhesion to the substrate and good durability in a flowing water environment.

The doping and annealing process enabled bandgap reduction to the visible light spectrum for all coatings, with the smallest bandgap of 2.48 eV. The value of the bandgap was inversely related to the annealing temperature for both pure anatase and anatase/rutile coatings, with the exception of anatase/WO₃ coatings.

The higher annealing temperatures resulted in rougher coated surfaces, which was proved to have negative effect on photocatalytic activities with the WO₃ doped coatings. Methylene blue degradation tests under UV-C showed that the coatings annealed in 460°C had better performance and with the best rate constant of 5.59 h⁻¹ significantly higher than previously reported values.

Chapter 4 An UV-C Based Advanced Photooxidation Reactor Design for Remote Households and Communities Not Connected to A Municipal Drinking Water System

Yongmei Jiao^a, Helen Shang^a and John A. Scott^{a*}

^a Bharti School of Engineering, Laurentian University, 935 Ramsey Lake Rd. Sudbury, P3E 2C6 Ontario, Canada

* Corresponding author email: jascott@laurentian.ca

Submitted to: *Journal of Environmental Chemical Engineering*

A household scale UV-C/TiO₂ based advanced oxidation process (AOP) reactor was developed for drinking water treatment. A 3D UV-C absorption model to predict light energy absorbed by the photocatalyst coatings was developed and agreed with direct light irradiance measurements. The tubular reactor was used with and without titanium dioxide (TiO₂) coated plates lining inside and was found to simultaneously inactivate a high initial concentration of *Escherichia coli* and degrade uracil, which was used as a synthetic water pollutant. The reactor, lined with replaceable TiO₂ coated plates, degraded uracil by 34.2 % and natural organic matter in raw lake water by 33.2 % within 24 minutes. An additional low dose of hydrogen peroxide also demonstrated an advantage to a reactor without TiO₂ coated plates. The electrical energy per order value was evaluated for this UV-C/TiO₂ reactor to be 8.13 kWh/m³, which is in the competitive range for a photocatalytic reactor. The UV/photocatalyst based AOP water treatment reactor design shows practical application potential for remote households and communities that do not have access to municipal water treatment.

4.1 Introduction

Drinking water disinfection is essential to public health,^[6] but other contaminants in source water, such as natural organic matter (NOM) can form harmful disinfection by-products (DBPs) with commonly used chemical disinfectants.^[101] Due to accelerated water eutrophication from anthropogenic nutrient additions and increasing water temperatures, there has been a rise in cyanobacterial (blue-green algae) blooms and risk from their extremely soluble toxins, such as cylindrospermopsin, which contributes to NOM contamination and toxicity in waterbodies.^[2] NOM is in particulate, colloidal and dissolved forms in all ground and surface waters, with the majority of NOM removed during the coagulation/sedimentation processes of a traditional drinking water treatment plant.^[5] However, residue NOM may enter the final disinfection stage, where methods using chlorination can result in formation of harmful DBPs, such as trihalomethanes (THMs) and haloacetic acids (HAAs).^[4] As carbon is the key component of NOM, total organic carbon (TOC, in mg/L) has been widely used as a quantitative measure of NOM.^[4]

Whilst non-chlorination disinfection techniques, such as UV-C radiation, commonly used for small water supplies or individual households, effectively inactivate microorganisms, they result in little NOM removal.^[6] With the discovery of harmful DBPs resulting from traditional disinfection processes,^[6] as well as stricter regulations for TOC level in drinking water,^[28] there is interest in combined UV-C based advanced oxidation processes (AOPs). AOPs with UV-C irradiation have been reported to achieve both pathogen inactivation and NOM reduction.^[6] AOPs were initially defined as oxidation processes that generate hydroxyl radicals (OH·), a powerful oxidizing agent that can degrade or mineralize NOMs, with or without a

photocatalyst.^[15] The concept has been now extended to other constituents with oxidizing potential, such as sulfate radicals ($\text{SO}_4^{\cdot -}$), ozone (O_3), and hydrogen peroxide (H_2O_2).^[23] However, OH^{\cdot} has the most powerful oxidization potential and can be created at a photocatalytic surface, such as titanium dioxide (TiO_2),^[102] by photons irradiated from a UV lamp (UVA, UVB or UV-C),^[23] or by the combination of UV irradiation with chemicals such as H_2O_2 .^[16] Although both are OH^{\cdot} generating AOPs, the UV/Photocatalyst (mostly TiO_2 or modified TiO_2) and UV/ H_2O_2 processes have different photo-conversion efficiencies. The former has a range between 0.0002 %-2 % with UV lamps, while the latter can reach 50 % with UV-C 254 nm irradiation in an organic matter free water, which in turn leads to 100 % OH^{\cdot} production.^[44] An UV/ TiO_2 heterogeneous AOP generates only OH^{\cdot} s which have a short lifetime, are nonselective, not toxic, and non-corrosive.^[15] The process is also free of bromate ions that are often related to an ozone AOP process,^[15] and iodinated DBPs resulted from the portable reused water (from municipal wastewater effluent and after traditional treatment and granular activated carbon filtration) with an UV/ H_2O_2 process.^[29] Another benefit from using a photocatalyst is that it enables not only oxidation, but also reduction, which means oxyanions such as nitrate, chromate, and redox-active metal ions, such as Ag^+ , can be reductively removed.^[44] Furthermore, toxic ions such as Cr (VI) can be reduced to the less toxic form Cr (III) and precipitated.^[44] TiO_2 is the most used photocatalyst as it is inexpensive (~ 1 USD/kg),^[44] relatively nontoxic and robust in photo reactions, yet is a chemically stable semiconductor material suitable for water treatment applications.^[17] UV/ H_2O_2 AOPs have been applied in pilot and full-scale water treatment,^[16,29,103] whereas UV/ TiO_2 applications have been rarely reported. There is, therefore, a need to develop advanced photocatalytic materials and optimize reactor design/evaluation in order to adapt the technology

to full-scale applications.^[44] The benefit of achieving NOM or anthropogenic pollutant purification without adding consumable chemicals or use of expensive equipment, such as an ozone generator, is attracting attention world-wide.^[18]

Based on the electrical energy per order (EE/O) needed to degrade a contaminant by one order of magnitude in 1 m³ of contaminated water,^[104,14] due to low photon conversion efficiency,^[44] the energy efficiency of UV/TiO₂ AOP is lower than UV/H₂O₂ by orders of magnitude. This disadvantage could be offset by applying this technology in a place where solar energy is abundant, since UV/TiO₂ AOP can be initiated from sunlight,^[105] or with solar power running the treatment system.^[106] This process can, therefore, be applied to remote communities with no municipal water treatment and chemical transportation is difficult, when the soluble NOM in the source water is low, or where there are existing UV-C water treatment units to disinfect water. In these cases, adapting UV/TiO₂ AOP for further NOM deduction could be cost effective.

Photon conversion efficiency can be also enhanced through photocatalyst material improvements, including bandgap reduction to help absorb more energy from a broader spectrum.^[43] The improvement of other properties such as charge carrier separation of photocatalyst separation by doping anatase TiO₂ with rutile TiO₂, and surface morphology optimization are also important to enhancing photocatalytic reactions.^[86] For an immobilized catalyst reactor with a fixed light source, reactor design can influence the energy absorbed by the photocatalysts, and thus the photon conversion efficiency.^[43,107] To evaluate a photocatalytic reactor design, overall mass transfer optimization such as flowrate control is important for reaction efficiency improvement^[37] and light energy absorption can be modelled.^[13,37,38]

A few UV/TiO₂ AOP commercially available applications for water treatment (have been reported in recent years. These include the TiO₂ slurry photoreactor Photo-Cat® and a

photoreactor with TiO₂ coating developed by Brightwater Environment.^[18] However, the impact on NOM, light energy absorption or a photonic efficiency analysis, which are important to photocatalytic reactor design, have not been reported.

In this work, a household scale UV-C/TiO₂ reactor was developed and investigated for decontaminating raw water. A tubular reactor was lined with thin stainless-steel plates coated with doped TiO₂ developed from previous work.^[43] The plates were removable for cleaning and for regeneration. A set of non-coated stainless plates were lined inside the reactor for comparison.

A 3D model of light energy absorption was developed and validated with direct light irradiance measurements. The light power absorption by the TiO₂ coating was determined from the mathematic model and reactor photonic efficiency evaluated.

As the primary treatment target for UV-C is disinfection,^[27] *Escherichia coli* (*E. coli*) inactivation experiments and were conducted in the reactor system. It is essential that the designed reactor retains its capacity to inactivate microorganisms, as well as degrade harmful organic pollutants. To test NOM removal, degradation of both uracil, a simple organic compound, and raw lake water were tested in the reactor. As one of the soluble pyrimidine derivatives present in water bodies through natural DNA biodegradation,^[108] uracil, has the potential to be mineralized by a UV/TiO₂ AOP.^[108-110] The additional use of hydrogen peroxide (H₂O₂) was also examined with a view to further enhance NOM reduction.

4.2 Experimental Details

4.2.1 Photocatalyst Coating

The TiO₂ coating method used was adapted from previous reported work,^[43] in which 316 stainless-steel plates were coated with combinations anatase and rutile (the two forms of TiO₂) and cured for two hours at 460°C. In this current work, 17 wt.% of rutile and 83 wt.% anatase powder (Nanostructured & Amorphous Materials Inc., USA) were mixed with deionized water (DI) and HCl acid (1N). The resulted slurry had a density of ~70 g/L and pH of ~1, which was coated on 304 stainless-steel plates (10 cm × 16.7 cm × 0.01 cm) and cured in a muffle furnace (Thermo Scientific Thermolyne™ Benchtop) at 460°C for 2 hours. The resulting photocatalyst loadings were an average of 3 mg/cm². 16 pieces of coated plates were placed into the reactor column (Figure 4.1), and the plates were reused without apparent loss of coating or efficiency through out all the experiments. As a comparison, 16 uncoated stainless-steel plates were also used to line the reactor.

From previous work, the anatase/rutile coating had a band gap of 2.48 eV, compared to the original powder band gaps of rutile (2.97 eV) and anatase (3.69 eV).^[43] This much shortened band gap is liable to absorb more light energy.^[43] The coating layer fully covered the substrate and had a thickness of 17-30 μm (measured with R&D™ TC100 coating gauge), which exceeded the minimum requirement of 4.1 μm for UV-C penetration.^[93] The coating was found to be both mechanically and chemically stable, and kept effectiveness with all experiments conducted.^[43]

4.2.2 Reactor Design

The reactor system set-up is shown in Figure 4.1. An 84 cm column (PVC pipe, inside diameter 10 cm) was fitted with end caps that held individually controlled four 55-W UV-C lamps

(Geekpure™, 82.5 cm long, 1.5 cm diameter) and quartz sleeves (diameter 2.4 cm with 1 mm thickness). The distance between each lamp center and the column center was 3.1 cm. A 20 L of deionised water (DI) was circulated from a reservoir by a submersible utility pump (ECOFLO™, 1/4HP or 186.4 W) via a water filter (Rainfresh™, pore size 1 μm). Inlet and outlet valves were used to control the flowrate, with any excess flow diverted back to the reservoir.

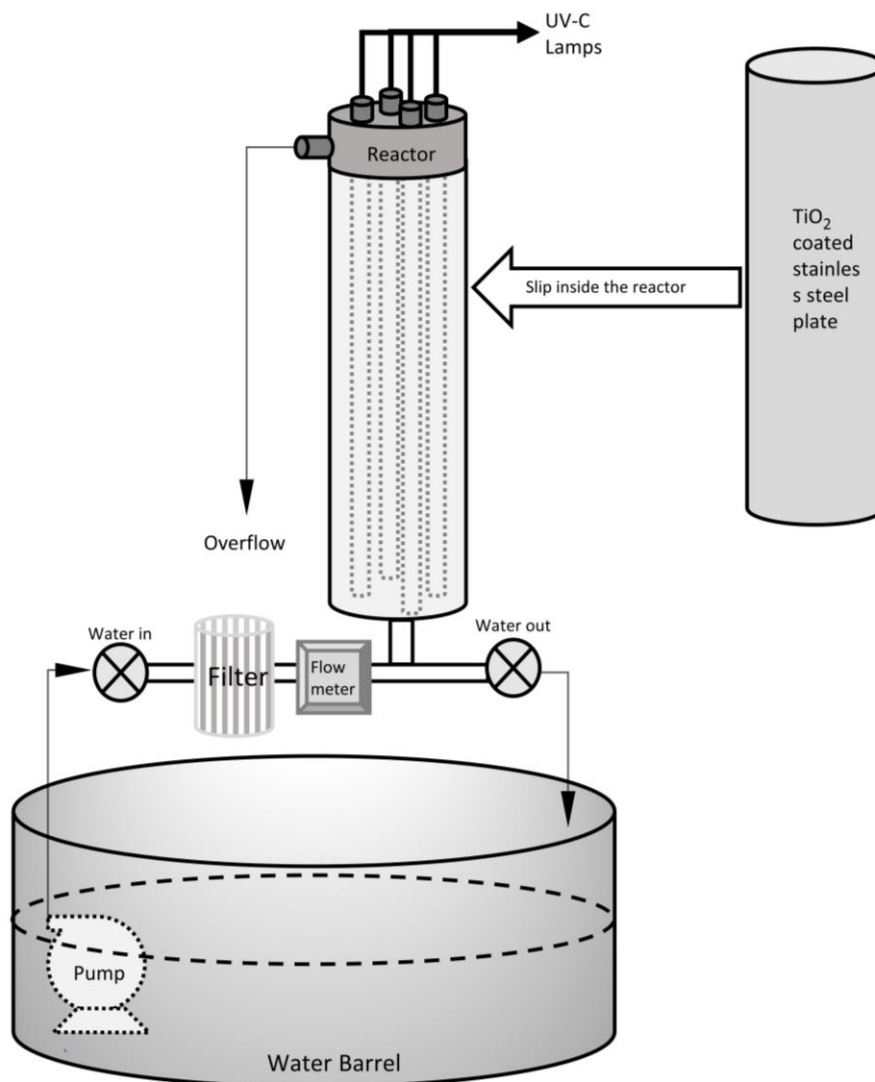


Figure 4.1 The experimental water purification system.

4.2.3 Experimental Runs

The UV-C light irradiance within the reactor was measured with a photometer (Linshang™ LS125 UV- light meter) in both the air and in the water flows to help determine energy absorption by the photocatalyst coated and uncoated stainless-steel plates lined reactor wall.

E. coli was mixed uracil/NaCl water to simulate natural condition. A sterilized solution containing 100 mL uracil (Sigma-Aldrich™, 1 g/L) and NaCl (Sigma-Aldrich™, 8.5 g/L) solution was mixed into 20 L sterilized DI water to make an uracil concentration of 5 mg/L with NaCl at 0.85 % w/v (for *E. coli*. to maintain viability). DI water was sterilized by circulating (by the pump) the water through the reactor for 20 minutes at 5.1 L/min (without the filter used for other experiments), but with two 55-W UV-C lamps operational. A 50 mL *E. coli* (ATCC 11303) stock solution (1.05×10^9 CFU/mL) was pelleted in a centrifuge at 3000 rpm for 10 minutes, after removing solute, the pellet was suspended in 500 mL 0.85 % w/v sterilized NaCl water for the inactivation experiments.

For the adsorption experiments, 1 mL *E. coli* solution (from the 500 mL suspended *E. coli*) was circulated in 20 L sterilized uracil water by the pump for 5 minutes and 0.5 mL samples were taken at the beginning and after 24 minutes; for the disinfection experiments (immediately after adsorption), two lamps were turned on and 0.5 mL samples (*E. coli* sampling) taken every 2 minutes for 6 minutes, and for uracil degradation, three 1 mL samples taken every 4 minutes for 24 minutes. The *E. coli* samples, after dilution, were spread onto petri dishes containing LB agar (Luria-Bertani broth powder and agar powder, Sigma-Aldrich™), and placed in an incubator

(RH-TECH™) for 18 hours at 37°C. The number of colonies formed were counted and averaged. Each set of experiment was repeated three times.

The concentration change of uracil during experimental runs was determined with an UV-Vis spectrophotometer (Biochrom™ Libra S32 PC) at a peak wavelength of 259 nm or UV₂₅₉.

Changes occurring with a pure uracil solution (5 mg/L), uracil with salt, and uracil with salt and *E. coli* were all examined. These experiments were carried at room temperature (22±0.5°C) and with a solution initial pH range of 6.2 ± 0.2, and dissolved oxygen (DO) level of 5.2 ± 0.2 mg/L.

The 4-minute sampling interval was approximately the time for 20 L to be circulated at a flowrate of 5.1 L/min.

Oxidation experiments were also conducted with untreated lake water (Ramsey Lake, Sudbury, Ontario, Canada). Before each experiment, lake water was circulated through the 1 µm filter, but without UV, for 30 minutes to remove suspended solids. The initial lake water pH values were 7.5 ± 0.2 and the dissolved oxygen (DO) content 7.0 ± 0.4 mg/L. The determination of NOM concentration change of lake water was by using UV₂₅₄ measurement (UV absorbance at 254 nm), an accepted method to quantify NOM in drinking water sources.^[4,111,112] The initial NOM concentration of the lake water was also examined with a TOC analyzer (SHIMADZU™ TOC-5000A) and was in the range of 4.1 to 4.6 mg/L.

During the experimental runs, the initial sample temperature was 27.4 ± 3.6°C. For the experiments with H₂O₂, the treated water was tested with WaterWorks™ low range test strips.

4.3 Results and Discussions

4.3.1 Light Irradiance Absorption Modelling

As the photocatalytic reaction involves water, photons, and surface interaction, the energy absorption capacity is particularly important in reactor design. Essentially, the more energy absorbed, the more reactions may occur. From these photocatalytic experiments and other literature,^[23] both photolysis and photocatalysis mechanisms were found to contribute in a UV-C/TiO₂ based AOP. Therefore, maximising OH· production is the most important factor in the photoreactor design as a photoreaction greatly depends on the degree of energy absorption. For example, in previous work,^[37] different photoreactor layouts resulted in different light energy absorption levels and subsequent methylene blue degradation. Because the UV-C light has a diffusion emission nature,^[71] light energy will decay with distance, and a relatively compact design will help contaminated water to receive more energy.

For the reactor used in this work, a coated thin film on the thin stainless-steel plates around the reactor column receives UV-C lamp light energy and produces a heterogenous reaction, which is key to total OH· production. Based on the diffusion emission theory of UV-C light,^[37] a 3D mathematic model was developed to evaluate the absorbed energy of the coatings, which was then verified with direct measurements taken with a photometer (Linshang™ LS125 UV- light meter). To take into consideration of the influence of water flow and make the model more precise, the light irradiance was measured in air inside a column lined with uncoated and TiO₂ coated stainless-steel plates and also with water at a fixed flowrate.

4.3.1.1 3D UV-C Absorption Model for TiO₂ Coated Surface

Photocatalytic material is excited by photon energy, where energy is transferred from its electrons in the valence band to the conduction band. This generates electron-hole (E-H) pairs that enable photocatalytic reactions. The optical absorption coefficients of materials determine

the penetration depth of the light, and these values strongly depend on the light wavelength.^[72]

The spectral absorption coefficient, $\alpha(\lambda)$, of the TiO₂ coating is the fraction of the absorbed incident energy of wavelength λ , and the relationship is expressed by Equation (4.1):^[40]

$$\alpha(\lambda) = 0.5 - 0.5 \tanh\left[\frac{\lambda - 355.66}{12.743}\right] \quad (4.1)$$

Since UV-C light's λ is 254 nm, by substituting λ into Equation (4.1), the absorption coefficient $\alpha(\lambda)$ would be 1, which means UV-C energy will be totally absorbed by the TiO₂ coating.

To evaluate UV-C absorption by the coating of the reactor system, a three-dimensional (3D) coordinate was set-up, with Figure 4.2 depicting part of the column reactor surface under the lamp tube, and with the tube axis coincident to the Y-axis. As the absorption coefficient is assumed to be 1, this means all the photonic energy can be absorbed by the plates and no photon reflection need to be considered. Furthermore, as the irradiation condition is identical for all lamps, only half of the reactor surface and the incident energy from one lamp need to be calculated. As shown in Figure 4.2, the lamp has a radius of a , and the reactor column has a radius of b with its center in Z-axis $(0, 0, c)$; $\overrightarrow{PP'}$ is the vector between P (a random point or differential area on the lamp) and P' (a random point or differential area on the reactor wall/coating); α is the angle between lamp normal vector $\overrightarrow{n_{lamp}}$ and $\overrightarrow{PP'}$, β is the angle between $\overrightarrow{PP'}$ and $\overrightarrow{n_{wall}}$, the vector of the reactor wall.

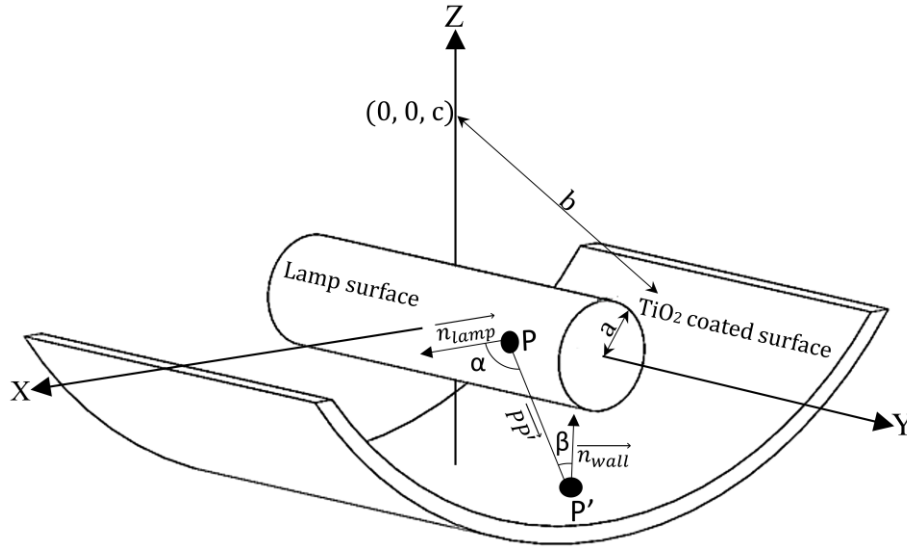


Figure 4.2 UV-C light absorption coordinate system.

The absorbed energy at any point on the reactor coating surface depends on the light irradiance value, the angle from light source normal, incident direction to the reactor surface, and the absorption coefficient.^[37-39] In this reactor system, the irradiance absorbed along the lamp surface by any point P' on reactor coating can be expressed as Equation (4.2):^[37]

$$I = a(\lambda) \frac{dP}{\pi^2} \iint \frac{\cos \alpha \cdot \cos \beta}{r^2} ds \quad (4.2)$$

where I is the absorbed light irradiance by any point P' on the reactor wall; $a(\lambda)$ is the light absorption coefficient, and dP is the unit light irradiance on the lamp surface; r is vector modulus $|\overrightarrow{PP'}|$ and S is the lamp surface area to be projected to P' . Cosine of vector angles (α and β) can be expressed as Equations (4.3) and (4.4):

$$\cos \alpha = \frac{\overrightarrow{n_{lamp}} \cdot \overrightarrow{PP'}}{|\overrightarrow{n_{lamp}}| \cdot |\overrightarrow{PP'}|} \quad (4.3)$$

$$\cos \beta = \frac{\overline{n_{wall}} \cdot \overline{PP'}}{|\overline{n_{wall}}| \cdot |\overline{PP'}|} \quad (4.4)$$

As shown in Figure 4.3, the lamp surface area can be expressed as a parameter equation. A random point $P (a \cos \theta, t, a \sin \theta)$, where a is the lamp radius, t is the perimeter of the point on the Y-axis, and the lamp normal vector can be expressed as Equation (4.5):

$$\overline{n_{lamp}} = -(a \cos \theta)i - (a \sin \theta)k \quad (4.5)$$

Assume P' is a fixed point and has a coordinate as (R, S, T) on the reactor wall and then the vector $\overline{PP'}$ can be expressed as Equation (4.6), the boundary angles $\theta 1$ and $\theta 2$ (Figure 4.3) can be found when $\overline{n_{lamp}}$ and $\overline{PP'}$ are perpendicular as shown in Equation (4.7):

$$\overline{pp'} = (R - a \cos \theta)i + (S - t)j + (T - a \sin \theta)k \quad (4.6)$$

$$\overline{n_{lamp}} \cdot \overline{PP'} = 0 \quad (4.7)$$

Substitute Equation (4.5) and (4.6) into (4.7), $\theta 1$ and $\theta 2$ can be expressed as Equation (4.8) and (4.9):

$$\theta 1 = 2 \left(\tan^{-1} \left(\frac{T - \sqrt{R^2 + T^2 - a^2}}{R + a} \right) \right) \quad (4.8)$$

$$\theta 2 = 2 \left(\tan^{-1} \left(\frac{T + \sqrt{R^2 + T^2 - a^2}}{R + a} \right) \right) \quad (4.9)$$

When the differential area or point P' on the cylindrical column reactor surface is random, it can be expressed as a parameter equation $(b \cos \varphi, y, b \sin \varphi + c)$, and then the vector $\overline{n_{wall}}$, $\overline{PP'}$ and modulus $|\overline{pp'}|$ can be expressed as Equation (4.10), (4.11) and (4.12) respectively:

$$\overline{n_{wall}} = -(b \cos \varphi)i - (b \sin \varphi)k \quad (4.10)$$

$$\overrightarrow{pp'} = (bcos\varphi - a cos \theta)i + (y - t)j + (bsin\varphi + c - a sin \theta)k \quad (4.11)$$

$$r = |\overrightarrow{PP'}| = \sqrt{(bcos\varphi - acos\theta)^2 + (y - t)^2 + (bsin\varphi + c - asin\theta)^2} \quad (4.12)$$

where $0 \leq \varphi \leq \pi$, and $-l/2 \leq y \leq l/2$ (l is the length of the reactor column).

Substituting Equation (4.3) and (4.4) to obtain cosine angles and then Equation (4.12) into Equation (4.2) together with boundary values, the light irradiance absorbed by a random point or differential area can be rewritten as Equation (4.13):

$$I = a(\lambda) \frac{dP}{\pi^2} \int_{-f}^f \int_{\theta_1}^{\theta_2} \frac{\cos \alpha \cdot \cos \beta}{r^2} ad\theta dt \quad (4.13)$$

where a is the lamp radius and f the projection length from the lamp to a point or differential area on the reactor surface, which was obtained from light intensity measurements inside the reactor column, and θ_1 and θ_2 are the boundary angle values.

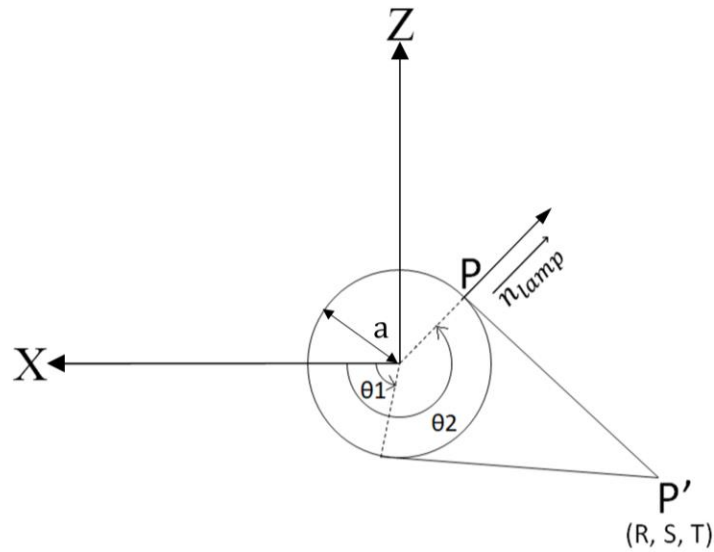


Figure 4.3 Cross section view of a lamp irradiation to a point of the reactor.

After the intensity for each differential area is integrated along the reactor wall and the reactor dimension data are applied, the total power or energy absorption can be calculated from Equation (4.14):

$$w = \int_0^{\pi} \int_{-\frac{l}{2}}^{\frac{l}{2}} I b dy d\theta \quad (4.14)$$

where w is the power, l the length of lamp that is parallel to the Y-axis, I light irradiance absorbed by each differential area, and b the inside radius of the reactor column wall.

A model to calculate the numerical value of light energy absorption was constructed using MATLAB®. The light absorption profile along half of the column is plotted in Figure 4.4 (the X-axis is the angle from 0 to π along the half column surface, with, as expected, the peak position closest to one of the lamps). The boundary values were considered when integrating column absorption areas. Based on the reactor geometry and lamp position, the coated wall receives 16 W power from a 55-W UV-C lamp with a length of 82.5 cm. If rearrange the lamp to a little center by changing “ c ” position (Figure 4.2) from 3.1 cm to 2.8 cm (by moving the lamp toward the column reactor center), the power absorption would be 13.1 W.

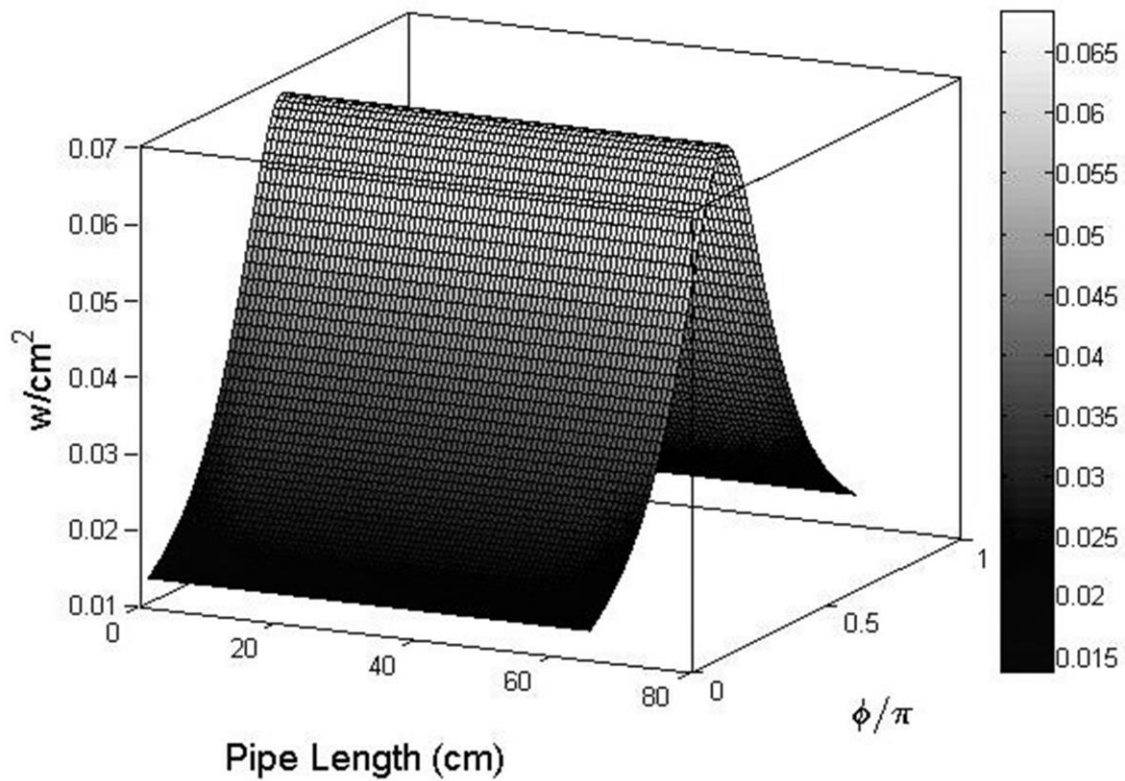


Figure 4.4 UV-C powder absorption profile along the reactor wall.

4.3.1.2 Model Validation

The light irradiance at different distances from the lamp center was calculated and the results compared with direct measurements (in air) using a photometer (Linshang™ LS125 UV- light meter). Figure 4.5 shows that the measured values agree well with the model's predictions.

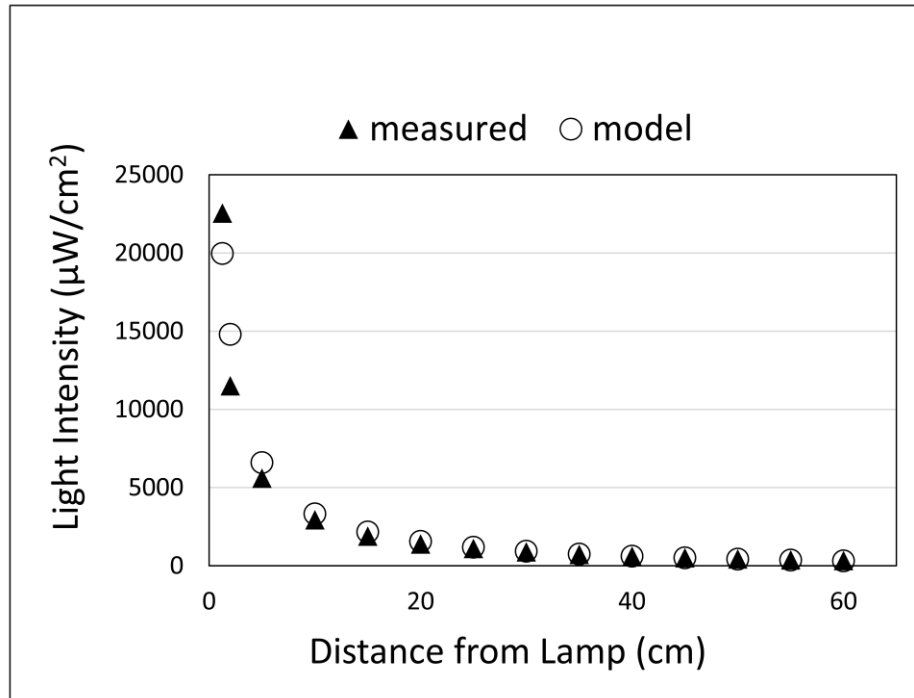


Figure 4.5 Measured UV-C light irradiance and model predictions.

4.3.1.3 Model Justification in Water

According to Snell's law (Equation (4.15)),^[113] the light angle will be changing with different media. However, since the emitters on the UV-C lamp are considered as spheres and rays are in all directions,^[37] when they pass through the thin quartz sleeves (1 mm thickness) to water, the influence of direction change can be ignored.

$$\frac{n_{water}}{n_{quartz}} = \frac{\sin\theta_{quartz}}{\sin\theta_{water}} \quad (4.15)$$

where n is the index of refraction for the travelling media (quartz or water), and θ the incident or refractive angle in the adjacent media.

Light irradiance testing was carried out at different flowrates in the reactor lined with either uncoated or TiO₂ coated stainless-steel plates. It was observed that in the uncoated stainless-steel lined reactor, the irradiance was higher than that with the coated one at the same location and higher than the model value. This may be a result of surface reflection of the uncoated plates. With the TiO₂ coated surface, light irradiance measurements agreed with the model.

When the reactor was filled with water at different flowrates (0 to 12.25 L/min), the light irradiance values measurement was different from the model and dropped slightly with increased flowrates. The presence of small bubbles, which increased with flowrate, may be the cause of lower irradiance readings and, therefore, a slower flowrate (5.1 L/min) was adopted for all the experiments to avoid bubble generation.

When UV rays travel through water, photonic energy will be absorbed by water molecules and other ions/molecules that are present. In pure water, UV-C transmittance (1 cm) can be 97.72 %.^[114] In the reactor design studied, the maximum distance from the lamp to a catalyst coated surface was 2.5 cm, therefore, the incident irradiance to the photocatalyst coated wall should be modified to reflect the transmittance percentage (e.g., 90 %, which a typical value for tap water^[115]). However, whilst the percentage transmission needs to be determined for each source of water investigated, application of this model is valid to compare the efficiency of different reactor configurations in order to help optimize the design.

4.3.1.4 Photonic Efficiency Comparison

Photonic efficiency, as defined by Equation (4.16), can be used to evaluate the performance of a photocatalytic reactor:^[37]

$$\eta = \frac{\text{molecules converted}}{\text{photons incident}} \quad (4.16)$$

where η is the photonic efficiency. The higher photonic efficiency with an AOP process shows effective use of radiation by the reactor.^[116] Taking the run with four UV-C lamps and rutile doped plates as an example, using uracil reduction data from next section, the photonic efficiency was 0.19 % (taking into account of 90 % transmittance), which was lower than that reported for methylene blue (MB) in previous work (2.83 %).^[37] This is likely a result of different reacting species and differences in reactor configurations. That is, compound (uracil or MB) dissociation energies are different, and/or the corrugated photocatalytic reactor used for MB degradation might absorb more energy than the flat photocatalyst plate reactor used to degrade uracil.

4.3.2 Advanced Oxidation Experiments

UV-C application in a drinking water treatment plant is primarily for disinfection, and removal of *E. coli*, is used in routine quality analysis.^[117] UV/TiO₂ based AOP application in water treatment should be able to disinfect microorganisms, but also degrade harmful organic pollutants at the same time.

After the disinfection/purification experiments, both the uracil solution and the raw lake water samples (without adding *E. coli* and salt or sterilizing solution) were run through the reactor at

different conditions. These were (i) with the reactor column lined with either uncoated stainless-steel plates or with TiO₂ coated plates, (ii) irradiation with different numbers of UV-C lamps and (iii) with the addition of H₂O₂.

4.3.2.1 Sample Run Naming

Sample runs are identified by a code based on the experimental conditions. The code sequence is sample name, plate lining, lamp number, and H₂O₂ concentration:

- Uracil as “U”, lake water as “L”, *E. coli* and uracil as EU;
- Uncoated stainless-steel plates as “S” and the coated plates as “C”;
- Lamp numbers are: 0, 2, and 4;
- H₂O₂ concentrations are 0.0, 2.5, 5.0, 7.5, and 13.2 mg/L respectively.

For example, the sample run labelled “EU-C-2-0” was a solution of *E. coli* and uracil, passed through a reactor lined with coated plates and irradiated by two lamps, but with no added H₂O₂.

4.3.2.2 Disinfection and AOP

To test the simultaneous disinfection and oxidation capacity of the reactor, *E. coli* (ATCC 11303) at an initial concentration of 4900 CFU/mL and sterilized uracil at a concentration of 5 mg/L were used. The concentration measurement of uracil at 259 nm was not influenced by either NaCl or by both NaCl and *E. coli*.

As shown in Table 4.1, during the 24-minute adsorption process with the standard deviation (SD) of sample CFU/mL counts. The *E. coli* count was relatively stable because of the 0.85 % w/v salt

water (the count difference may be an uneven distribution of *E. coli* in water). After the UV-C lamps were turned on, more than half of the *E. coli* were inactivated and at the 2th minute, there was no live *E. coli* after the 4th minute (based on the flowrate, 4-minute was a time period for all the water flow through the reactor).

Table 4.1 *E. coli* Inactivation Test

Test	NO. of UV-C lamp	Time (min)	CFU/mL	
			Count	SD
Adsorption	0	0	4900	200
	0	24	4400	360
Inactivation	2	0	4400	360
	2	2	1480	85
	2	4	0	0
	2	6	0	0

The concentration of *E. coli* used in this experiment was much higher than the U.S. Environmental Protection Agency (EPA) guideline values for *E. coli* in fresh recreational waters single sample maximum concentration (2.35 CFU/mL)^[118] and there should be no detectable *E. coli* in drinking water.^[117] Based on the experimental results, the UV-C reactor has sufficient capacity to inactivate all *E. coli* at such a concentration. Although *E. coli* inactivation with OH⁻s was reported,^[6] the influence of TiO₂ coated plates to *E. coli* inactivation could be minimum due

to the high germicidal power of UV-C for *E. coli* inactivation.^[27] As shown in Table 4.2, uracil reduction over 24 minutes was 11.7 % (EU-C-2-0.0), and slightly lower than the pure uracil degradation at the same condition (U-C-2-0.0), possibly due to the salt addition, which absorbed light energy before it reaches to the photocatalyst coated surface and the absorption will increase with the salt concentration^[119] (not detectable with UV₂₅₉). An experimental run period of 24 minutes was relative short for an UV/TiO₂ based AOP with such a practical volume (20L), however, with the total power consumption (four 55-W lamps and 186.4 W pump), if the time is too long, the electrical energy per order (EE/O) value will be exceeding the competitive range (<~0.5 to 10 kWh/m³) for drinking water applications,^[14,44] the following different AOP development was aimed to be both efficient and economical.

4.3.2.3 Uracil and Lake Water Natural Organic Matter Degradation

Uracil and lake water natural organic matter (NOM) degradation are likely to involve different reaction mechanisms, making reaction rates difficult to compare. However, as the purpose of the experiments was to compare efficiency of reaction under different conditions, only percentage concentration deductions after 24 minutes are given in Table 4.2 (with the percentage of standard deviation of each sample run).

Table 4.2 Uracil and Lake Water NOM % Degradation in 24 Minutes

	Sample Run	% Degradation	SD (%)	Sample Run	% Degradation	SD (%)
U R A C I L	EU-C-2-0.0	11.7	0.9	U-S-0-7.5	0.9	0.0
	U-S-2-13.2	94.5	1.6	U-S-0-13.2	1.4	0.1
	U-S-2-0.0	13.7	0.6	U-C-2-0.0	12.9	0.7
	U-S-4-0.0	29.0	1.7	U-C-4-0.0	34.2	0.8
	U-S-4-2.5	41.0	2.6	U-C-4-2.5	57.6	1.2
	U-S-4-5.0	69.8	1.6	U-C-4-5.0	74.9	1.0
	U-S-4-7.5	84.5	1.5	U-C-4-7.5	97.5	1.1
L A K E						
	L-S-2-0.0	16.6	0.5	L-C-2-0.0	18.9	0.9
	L-S-4-0.0	27.4	2.2	L-C-4-0.0	33.2	0.8
	L-S-4-2.5	40.0	1.5	L-C-4-2.5	43.5	2.2
	L-S-4-5.0	61.6	1.2	L-C-4-5.0	65.9	1.8
	L-S-4-7.5	71.2	1.6	L-C-4-7.5	76.3	2.5

As shown in Table 4.2, the U-S-0-7.5 and U-S-0-13.2 runs are similar to a traditional disinfection process (not involve OH[·] generation), which resulted in little uracil degradation.

A germicidal UV-C lamp has a peak wavelength at 254 nm, and its radiation range covers a small part of the UV spectrum less than 242 nm, where direct photolysis of water can occur, as shown in Equation (4.17):^[23]



where hv is the photonic energy.^[23]

The OH· generating direct photolysis reactions in runs with only UV lamps (U-S-2-0.0, U-S-4-0.0, L-S-2-0.0, and L-S-4-0.0) demonstrated higher degradation potential, and the higher light energy, the higher percentage of degradation.

With the UV-C lamp in operation, all the reactions should have a certain degree of direct photolysis reactions because of the short wavelength range of the lamp; when adding H₂O₂ the direct photolysis reaction might be dominated by the UV/H₂O₂ AOP because of the high OH· production potential of the process,^[28] which have been applied in pilot and full-scale water treatment.^[16,29,103] The overall OH· generation of UV/H₂O₂ AOP can be shown in Equation (4.18):^[28]



The OH· generation from a UV/ H₂O₂ AOP likely initiated a chain of reactions, which led to the maximum OH· production in organic free water.^[44] However, when the H₂O₂ concentration is too high, it will act as an OH· scavenger.^[6] But for both uracil and lake water sample runs (U-S-4-0.0, U-S-4-2.5, U-S-4-5.0, U-S-4-7.5, L-S-4-0.0, L-S-4-2.5, L-S-4-5.0, and L-S-4-7.5), the increase of H₂O₂ from 0 to 7.5 mg/L, increased the percentage degradation of the original concentrations, which indicates that increasing OH· production within this dosage range of H₂O₂ did not result in OH· scavenging.

TiO₂ in the anatase phase is the most popular catalyst for photocatalytic water treatment because of its high photocatalytic activity, insolubility in water, low cost, photo-corrosion resistance, and resistance to chemical reactions.^[13,17] In a photocatalytic process, dopant addition of the rutile phase of TiO₂ into the anatase phase can promote effective charge separation and photocatalytic

activity.^[84] The coating method enabled a shortened band gap of the coated photocatalyst, which in turn allow a broader range of light energy to be absorbed and more light induced reactions to occur.^[43] UV/TiO₂ based AOP starts from the excitation of TiO₂ by the photons, which push electrons from their covalent band to conduction band where positive holes form on the photocatalyst surface, and then the positive holes and the electrons will react with water, oxygen and hydroxyl ions to produce OH·s that can be expressed as Equation (4.19) to (4.22):^[23]



Apart from the direct photolysis, sample runs with the lined TiO₂ coated plates (U-C-2-0.0, U-C-4-0.0, L-C-2-0.0, and L-C-4-0.0), may also involve UV/TiO₂ AOP which led to a comparable percentage degradation with two lamps, and a higher difference with four lamps.

With the addition of H₂O₂ into the TiO₂ coated reactor system, the degradation reactions may involve not only direct photolysis, UV/H₂O₂, UV/TiO₂ but also UV/TiO₂/H₂O₂ AOPs, with which extra OH·s may be generated during the interaction between the stricken a photocatalyst (TiO₂) surface, where the electron reacts with H₂O₂ as the Equation expressed below:^[15]



By comparing sample runs (U-S-4-2.5 vs. U-C-4-2.5, U-S-4-5.0 vs. U-C-4-5.0, U-S-4-7.5 vs. U-C-4-7.5, L-S-4-2.5 vs. L-C-4-2.5, L-S-4-5.0 vs. L-C-4-5.0, and L-S-4-7.5 vs. L-C-4-7.5), enhanced photodegradation was found with the TiO₂ coated-plate settings (Table 4.2).

With the uracil samples and four 55-W lamps, the reactor with TiO₂ coated plates demonstrated an advantage over uncoated stainless-steel plates by 5.2 % (U-C-4-0.0 vs. U-S-4-0.0, Table 4.2). Under two-lamp irradiation, the coated surface ((U-C-2-0.0) did not show an advantage over the uncoated one (U-S-2-0.0), which may be due to the photolysis reaction being greater than the photocatalytic reaction. When the light irradiance was measured inside the reactor at a fixed middle point, higher irradiance was found with uncoated steel plates lined reactor due to stronger light reflection from the steel surface, which enhanced the photolysis reaction. In Table 4.2, when adding H₂O₂ at different concentrations (2.5, 5.0 and 7.5 mg/L) under four lamps irradiation, degradation of uracil was greater with TiO₂ coated plates (U-C-4-2.5 vs. U-C-4-5.0, U-C-4-7.5) than with uncoated plates (U-S-4-2.5, U-S-4-5.0, U-S-4-7.5) by 16.6, 5.1, and 13 % respectively. Without UV irradiation and with 7.5 or 13.2 mg/L H₂O₂ (U-S-0-7.5, U-S-0-13.2), the degradation of uracil was only 0.9 or 1.4 % respectively. Whereas 97.5 % of uracil degradation was obtained with a 4-lamp TiO₂ coating lined configuration and 7.5 mg/L H₂O₂ (U-C-4-7.5). By comparing U-S-4-2.5 and U-C-4-2.5, the 16.6 % of uracil degradation difference could be attributed to the TiO₂ coating, which was equal to the contribution of two 55-W UV-C lamps. A comparison between the results with U-S-2-13.2 (94.5 % degradation) and with U-C-4-7.5 (97.5 % degradation), indicates the potential to reduce half of the H₂O₂ needs with a photocatalyst reactor.

With the lake water samples under different conditions the NOM degradation were generally lower than those for uracil. For example, with the same reactor configuration (L-C-4-7.5), NOM degradation was 76.3 %, compared to 97.5 % for uracil. UV_{254} and TOC has a linear relation in quantifying NOM in drinking water source,^[4,111,112] and the NOM of raw lake water at the same sample period was in the range of 4.1 to 4.6 mg/L. Therefore, according to the UV_{254} values of both the untreated raw lake water and of the uracil solutions, 5 mg/L uracil can be translated to a TOC of ~5.8 mg/L when TOC of the raw lake water is 4.6 mg/L. However, uracil had a better degradation rate, which might be a result of different reaction species, or the higher volume of suspend solids that was blocking UV irradiation and reducing the AOP reaction rate. Compare to a deionized water filter, which has a filtration pore size less than 0.2 μm ,^[120] the low pressure filter in this reactor system has a pore size of 1 μm ,^[121] and the non-removed suspended solids may hinder UV-C light penetration and subsequent reactions. It was found that the runs with TiO_2 coated plates had higher NOM degradation than the runs with uncoated stainless-steel plates by 2.3 to 5.8 %.

In both uracil and the lake water degradation experiments, the run with TiO_2 coated plates had better concentration degradation than without coated plates, and the low dose H_2O_2 enhance $\text{OH}\cdot$ production and reactions.

During all the runs, pH values were reduced by 0.5-0.6 units, hence increasing solution pH may enhance $\text{OH}\cdot$ production and photoreaction as described in Equation (4.20) and (4.22), which might be an explanation that the lake water had higher NOM degradation than uracil before adding H_2O_2 despite the suspended solids (the lake water had higher initial pH values). DO was similarly reduced, by 0.6-0.7 mg/L, and adding dissolved oxygen may enhance photooxidation

via E-H separation of charge carriers associated with the TiO_2 , $\text{O}_2^- \cdot$ generation (Equation (4.21)), or a combination with organic radicals.^[122] The amount of H_2O_2 residue after each experiment was assessed and found to be less than 0.3 ppm (mg/L). The US EPA guidelines for residual H_2O_2 is 25-50 ppm (mg/L) for drinking water disinfection.^[123] However, compared to traditional disinfection with chlorine, the cost of H_2O_2 is higher when applied to a full sized water treatment operation,^[16] and there is risk of DBPs.^[29]

4.3.2.4 Electrical Energy Per Order (EE/O) Evaluations

As an important parameter to evaluate AOP reactor performance, the EE/O values was investigated for four lamp coated plates lined reactor runs, which resulted in 34.2 % degradation in uracil and 33.2 % in lake water NOM, to be 8.13 kWh/m³. This is in the competitive range (0.5 to 10 kWh/m³)^[14,44] for a UV/ TiO_2 photoreactor. It may, however, be improved by lining some photocatalyst coated plates with corrugated surface to increase the surface area and achieve better results.^[37] The pump used in the system is also oversized for the flowrate applied (5.1 L/min), and could be replaced with a smaller unit to reduce the EE/O value.

The reactor is compact and easy to maintain and regeneratable on-site by the simple procedure of periodically replacing the coated linings. The concept could, therefore, for example be applied in remote areas where municipal water treatment is not available.

4.4 Conclusions

To cope with the aggregated natural organic matter (NOM) pollution in drinking water bodies and the carcinogenic disinfection by-products generated from the chlorine disinfection, a

practical scale water treatment system was developed to disinfect microorganisms and degrade water contaminants simultaneously, and was aimed to be both efficient and economical.

A three-dimensional UV-C absorption model was developed to predict light energy absorbed by the photocatalyst coatings, which was validated as a good fit with the light irradiance measurement in air and justified in water and could be applied in photocatalyst reactor design.

The tubular reactor of different configurations was examined with 20 L *Escherichia coli* (*E. coli*) solution (in NaCl and 5 mg/L uracil solution), uracil solution alone (used as a synthetic NOM pollutant), and the lake water from a municipal drinking water supply. It was found to be able to inactivate a high concentration of *E. coli* and degrade uracil at the same time, but uracil degradation without NaCl and *E. coli* was not as good as the degradation of uracil solution alone due to the NaCl absorption of UV light. Without adding any disinfectant, the reactor lined with replaceable TiO₂ coated plates, degraded uracil by 34.2 % and NOM in raw lake water by 33.2 % within 24 minutes. With additional low dose of hydrogen peroxide also demonstrated an advantage to a reactor without TiO₂ coated plates, which offers an option to achieve an optimum result for a full-scale water treatment operation.

The electrical energy per order value was evaluated for this reactor to be 8.13 kWh/m³, which is in the competitive range (0.5 to 10 kWh/m³) for a photocatalytic reactor. The reactor design can be improved by using corrugated coating surface to increase irradiated area and to produce more reactions, which is favorable for the applications in remote communities that do not have access to municipal water treatment. This reactor design also provided a niche to adapt the low-cost yet low-efficiency UV/photocatalyst based advanced oxidation technology.

Chapter 5 Conclusion and Future Work

To cope with the aggregated natural organic matter pollution (NOM) pollution in drinking water and the well-known carcinogenic disinfection by-products (DBPs) generated from the traditional chlorine disinfection, a germicidal ranged ultraviolet (UV-C)/photocatalyst based advanced oxidation process (AOP) has been studied, which has potential to disinfect microorganisms and degrade water contaminants at the same time but with low efficiency. The researcher had been working on the improvement of photoreactor design and photocatalyst activity, as well as on the adaption of the photocatalytic reaction water treatment technology in a practical scale and an economical fashion.

5.1 Conclusion

The contributions of this PhD work consist three parts:

- The establishment of A 3D UV-C light irradiance absorption model (by photocatalyst coated surface), which can be used in UV/photocatalyst AOP reactor design and optimization.
- A rutile titanium dioxide (TiO_2) and WO_3 doped anatase TiO_2 coating method was developed that greatly reduced bandgaps from the compounds' original powder forms.
- A household scale photocatalytic reactor design that has potential in NOM degradation and *E. coli* inactivation without adding any disinfectant. This may be applied in remote communities, which is a niche for photocatalyst application. This inexpensive and low

toxicity material could be used to produce additional water treatment performance from an existing UV-C disinfection unit.

As described in Chapter 2, a TiO₂ coated corrugated plate reactor was designed to improve water treatment performance. With a corrugated photocatalyst coated plate system, methylene blue (MB) degradation rate was found to be influenced by reactor configuration, initial concentration, and fluid flowrate. Under the same flow conditions, 70% of the MB was degraded within the first 10 minutes by a corrugated surface with TiO₂ coating, but only 12 % for a corrugated reactor without TiO₂ coating, and 4 % for a no-plate reactor. The MB photocatalytic degradation reaction mechanism could be described by the Langmuir-Hinshelwood model. A local area specific rate of energy absorption model was also developed and found to correlate well with measured irradiance values. Based on this model, with specified illumination conditions, reactor size, and photocatalytic coating surface area, the least corrugated configuration (i.e., the reactor with the least plates) absorbed the most photonic energy. The highest apparent photonic efficiency of the corrugated arrangement was found to be 2.83 %.

A coating method was described In Chapter 3, which could enhance photocatalytic activity of the TiO₂ based catalyst. The developed coating method used acidic anatase TiO₂ slurries doped with tungsten oxide (WO₃) or rutile TiO₂ to coat 316L stainless steel plates. The brush-coated plates were annealed at 460, 500, and 540°C in a muffled furnace. The successfully developed coatings were ~10 μm thick and demonstrated good durability in a flowing water environment. The doping and annealing process enabled bandgap reduction to the visible light spectrum for all coatings, with the smallest bandgap of 2.48 eV. The value of the bandgap was inversely related

to the annealing temperature for both pure anatase and anatase/rutile coatings, except for anatase/WO₃ coatings. The higher annealing temperatures resulted in rougher coated surfaces, which was proved to have negative effect on photocatalytic activities. MB degradation tests under UV-C showed that the coatings annealed in 460°C had better performance and with the best rate constant of 5.59 h⁻¹, which is significantly higher than previously reported values.

A household scale UV-C/TiO₂ based AOP column reactor described in Chapter 4, has potential to be applied in a small drinking water treatment plant, such as a household. The reactor used TiO₂ coated plates that lined the inside the tubular reactor, which has the potential to save energy and costs. A 3D UV-C absorption model based on the reactor's geometry was then developed and validated with direct light irradiance measurements. The model can be applied in UV/Photocatalyst reactor design to optimize use of the UV-C light source. The reactor also concurrently inactivated high concentrations of *E. coli* and degraded uracil which was used as a synthetic drinking water pollutant. Without adding any chemicals, the reactor with lined TiO₂ coating degraded uracil by 34.2 % and lake water natural organic matter (NOM) by 33.2% within 24 minutes. A low dose of food grade H₂O₂, was added to the reactor lined with TiO₂ coated plates and further improved performance. The electrical energy per order value was evaluated for this UV-C/TiO₂ reactor to be 8.13 kWh/m³, which is in the competitive range of 0.5 to 10 kWh/m³.

5.2 Future Work

The research outcomes of this work are very encouraging, but there are further tasks can be tackled to optimize this drinking water purification system design:

- Developing corrugated (triangular or wave) shaped surface coating to increase irradiated photocatalyst area in a limited space reactor for enhanced hydroxyl radical generation.
- Testing the coatings developed from previous work^[43] in the column photocatalytic reactor system with common waterborne toxins such as cylindrospermopsin.
- Research a filtration system design for further removal of suspended solids or NOM from drinking water source for the enhancement of UV irradiation efficiency.
- Applying the household scale water treatment system in daily water treatment operation.

References

- [1] W. J. Cosgrove, F. R. Rijsberman, *World water vision: making water everybody's business*, Routledge, **2014**.
- [2] R. Xia, Y. Zhang, A. Critto, J. Wu, J. Fan, Z. Zheng, Y. Zhang, *Sustainability* **2016**, *8*, 229.
- [3] G. Zhang, X. He, M. N. Nadagouda, K. E. O'Shea, D. D. Dionysiou, *Water Res.* **2015**, *73*, 353.
- [4] H. Canada, "Guidance on Natural Organic Matter in Drinking Water," *aem*, **2019**, accessed on June 8, 2020, <https://www.canada.ca/en/health-canada/programs/consultation-organic-matter-drinking-water/document.html>.
- [5] D. R. J. Moore, N. K. Nagpal, British Columbia, Water Quality Section, British Columbia, Environment and Resource Management Dept, *Ambient water quality guidelines for organic carbon in British Columbia: a report*, Environment and Resource Management Dept., Ministry of Environment, Lands and Parks, Victoria, B.C., **1999**.
- [6] M. Collivignarelli, A. Abbà, I. Benigna, S. Sorlini, V. Torretta, *Sustainability* **2017**, *10*, 86.
- [7] C.-H. Hsu, W.-L. Jeng, R.-M. Chang, L.-C. Chien, B.-C. Han, *Environ. Res.* **2001**, *85*, 77.
- [8] H. H. Hahn, E. Hoffmann, H. Ødegaard, *Chemical Water and Wastewater Treatment VIII*, IWA Publishing, **2004**.
- [9] J. R. Bolton, C. A. Cotton, *The Ultraviolet Disinfection Handbook*, American Water Works Association, **2011**.
- [10] W. Kowalski, "UVGI Disinfection Theory," *Ultraviolet Germicidal Irradiation Handbook*, Springer Berlin Heidelberg, Berlin, Heidelberg **2009**, p. 17.
- [11] E. Rodríguez, G. D. Onstad, T. P. J. Kull, J. S. Metcalf, J. L. Acero, U. von Gunten, *Water Res.* **2007**, *41*, 3381.
- [12] I. Boiarkina, S. Norris, D. A. Patterson, *Chem. Eng. J.* **2013**, *222*, 159.
- [13] C. McCullagh, N. Skillen, M. Adams, P. K. J. Robertson, *J. Chem. Technol. Biotechnol.* **2011**, *86*, 1002.
- [14] D. B. Miklos, C. Remy, M. Jekel, K. G. Linden, J. E. Drewes, U. Hübner, *Water Res.* **2018**, *139*, 118.
- [15] E. M. Cuerda-Correa, M. F. Alexandre-Franco, C. Fernández-González, *Water* **2019**, *12*, 102.
- [16] A. K. Boal, C. Rhodes, S. Garcia, *Groundw. Monit. Remediat.* **2015**, *35*, 93.

- [17] D. Chinungi, Surface Treatment of Photocatalyst Metal Supports for VOCs Abatement Applications. Master, KTH Royal Institute of Technology, Stockholm, Sweden, **2016**.
- [18] J. Strutt, J. Froud, Potential for Formation of Disinfection By Products from Advanced Oxidation Processes, WRc **2018**, <https://www.dwi.gov.uk/research/completed-research/risk-assessment-chemical/potential-for-formation-of-disinfection-by-products-from-advanced-oxidation-processes/>.
- [19] M. M. Khan, S. F. Adil, A. Al-Mayouf, *J. Saudi Chem. Soc.* **2015**, *19*, 462.
- [20] G. D. Christian, P. K. Dasgupta, K. Schug, *Analytical chemistry*, Seventh edition., John Wiley and Sons, Inc, Hoboken, NJ, **2014**.
- [21] “Explained: Bandgap,” *MIT News*, accessed on September 21, 2019, <http://news.mit.edu/2010/explained-bandgap-0723>.
- [22] Y. Doekhi-Bennani, Photoelectrocatalysis in water treatment. PhD thesis, Delft University of Technology, Delft, Netherlands, **2017**.
- [23] Y. Deng, R. Zhao, *Curr. Pollut. Rep.* **2015**, *1*, 167.
- [24] S. Kommineni, J. Zoeckler, A. Stocking, P. S. Liang, A. Flores, R. Rodriguez, T. Browne, P. R. Roberts, A. Brown, *Treat. Technol. Remov. Methyl Tert. Butyl Ether MTBE Fron Drink. Water Air Stripping Adv. Oxid. Process Granul. Act. Carbon Synthetic Resin Sorbents* **2000**, *2*, 109.
- [25] M. A. Rauf, S. Ashraf, S. N. Alhadrami, *Dyes Pigments* **2005**, *66*, 197.
- [26] J.-M. Herrmann, *J. Photochem. Photobiol. Chem.* **2010**, *216*, 85.
- [27] J. Park, E. Kettleon, W.-J. An, Y. Tang, P. Biswas, *Catalysts* **2013**, *3*, 247.
- [28] J. C. Mierzwa, R. Rodrigues, A. C. S. C. Teixeira, “Chapter 2 - UV-Hydrogen Peroxide Processes,” *Advanced Oxidation Processes for Waste Water Treatment*, S. C. Ameta, R. Ameta, Eds., Academic Press **2018**, p. 13.
- [29] Y.-H. Chuang, A. Szczuka, W. A. Mitch, *Environ. Sci. Technol.* **2019**, *53*, 3729.
- [30] A. Z. Jones, “What Exactly Is a Photon?,” *ThoughtCo*, **2017**, accessed on January 28, 2018, <https://www.thoughtco.com/what-is-a-photon-definition-and-properties-2699039>.
- [31] G. A. Shaw, A. M. Siegel, J. Model, A. Geboff, S. Soloviev, A. Vert, P. Sandvik, “Deep UV photon-counting detectors and applications,” 1 May **2009**.
- [32] David L. Chandler, “Explained: Bandgap,” *MIT News*, **2010**, accessed on January 24, 2018, <http://news.mit.edu/2010/explained-bandgap-0723>.
- [33] P. Gies, C. Roy, J. Javorniczky, S. Henderson, L. Lemus-Deschamps, C. Driscoll, *Photochem. Photobiol.* **2004**, *79*, 32.

- [34] B. Oram, “Water Research Center - UV Disinfection,” **2014**, accessed on January 28, 2018, <http://www.water-research.net/index.php/water-treatment/water-disinfection/uv-disinfection>.
- [35] M. Castellote, N. Bengtsson, “Principles of TiO₂ Photocatalysis,” *Applications of Titanium Dioxide Photocatalysis to Construction Materials: State-of-the-Art Report of the RILEM Technical Committee 194-TDP*, Y. Ohama, D. Van Gemert, Eds., RILEM State of the Art Reports, Springer Netherlands, Dordrecht **2011**, p. 5.
- [36] R. Yin, C. Shang, *IUVA News* **2018**, 20, 7.
- [37] Y. Jiao, A. T. Kovala, H. Shang, J. A. Scott, *Can. J. Chem. Eng.* **2019**, 97, 1760.
- [38] H. Shang, Z. Zhang, W. A. Anderson, *AIChE J.* **2005**, 51, 2024.
- [39] L. Zhang, W. A. Anderson, Z. (Jason) Zhang, *Chem. Eng. J.* **2006**, 121, 125.
- [40] A. A. Donaldson, A. Ye, J. G. McEvoy, Z. Zhang, *AIChE J.* **2013**, 59, 560.
- [41] S. M. Meunier, J. Gamage, Z. Duvnjak, Z. Zhang, *Int. J. Photoenergy* **2010**, 2010, 1.
- [42] L. Zhang, T. Kanki, N. Sano, A. Toyoda, *Sol. Energy* **2001**, 70, 331.
- [43] Y. Jiao, N. Basiliko, A. T. Kovala, J. Shepherd, H. Shang, J. A. Scott, *Can. J. Chem. Eng.* **2020**, 98, 728.
- [44] S. K. Loeb, P. J. J. Alvarez, J. A. Brame, E. L. Cates, W. Choi, J. Crittenden, D. D. Dionysiou, Q. Li, G. Li-Puma, X. Quan, D. L. Sedlak, T. David Waite, P. Westerhoff, J.-H. Kim, *Environ. Sci. Technol.* **2019**, 53, 2937.
- [45] A. Di Paola, M. Bellardita, L. Palmisano, *Catalysts* **2013**, 3, 36.
- [46] K. Fischer, A. Gawel, D. Rosen, M. Krause, A. Abdul Latif, J. Griebel, A. Prager, A. Schulze, *Catalysts* **2017**, 7, 209.
- [47] K. R. Reyes-Gil, D. B. Robinson, *ACS Appl. Mater. Interfaces* **2013**, 5, 12400.
- [48] W. H. Glaze, Y. Lay, J.-W. Kang, *Ind. Eng. Chem. Res.* **1995**, 34, 2314.
- [49] K. Aghasadeghi, M. Csordas, S. Peldszus, D. R. Latulippe, *Can. J. Chem. Eng.* **2017**, 95, 1943.
- [50] C. Chee, A. Abd, S. Ibrahim, M. Matheswaran, P. Sarav, “Heterogeneous Photocatalytic Oxidation an Effective Tool for Wastewater Treatment – A Review,” *Studies on Water Management Issues*, M. Kumarasamy, Ed., London., InTech **2012**.
- [51] CAMEO Chemicals, “TITANIUM DIOXIDE | CAMEO Chemicals | NOAA,” **2016**, accessed on September 15, 2018, <https://cameochemicals.noaa.gov/chemical/21114>.
- [52] F. Montecchio, D. Chinungi, R. Lanza, K. Engvall, *Appl. Surf. Sci.* **2017**, 401, 283.

- [53] M. Mirzaei, S. Sabbaghi, M. M. Zerafat, *Can. J. Chem. Eng.* **2018**, 9999, 1.
- [54] I. Boiarkina, S. Norris, D. A. Patterson, *Chem. Eng. J.* **2013**, 225, 752.
- [55] T. Akehata, T. Shirai, *J. Chem. Eng. Jpn.* **1972**, 5, 385.
- [56] S. Corbel, N. Becheikh, T. Roques-Carmes, O. Zahraa, *Chem. Eng. Res. Des.* **2014**, 92, 657.
- [57] C. Passalía, O. M. Alfano, R. J. Brandi, *Ind. Eng. Chem. Res.* **2011**, 50, 9077.
- [58] D. Mukherjee, S. Barghi, A. K. Ray, *Can. J. Chem. Eng.* **2014**, 92, 1661.
- [59] M. A. Rauf, S. S. Ashraf, *Chem. Eng. J.* **2009**, 151, 10.
- [60] F. Huang, L. Chen, H. Wang, Z. Yan, *Chem. Eng. J.* **2010**, 162, 250.
- [61] R. S. Dariani, A. Esmaili, A. Mortezaali, S. Dehghanpour, *Opt. - Int. J. Light Electron Opt.* **2016**, 127, 7143.
- [62] A. R. Khataee, M. B. Kasiri, *J. Mol. Catal. Chem.* **2010**, 328, 8.
- [63] H. R. Patil, Z. V. P. Murthy, *Chem. Eng. Res. Des.* **2017**, 124, 134.
- [64] A. Houas, H. Lachheb, M. Ksibi, E. Elaloui, C. Guillard, J.-M. Herrmann, *Appl. Catal. B Environ.* **2001**, 31, 145.
- [65] N. Ho, J. D. Gamage, Z. Zhang, *Int. J. Chem. React. Eng.* **2010**, 8, 1.
- [66] L. Bengtson, "Use the Friction Factor to Calculate Frictional Head Loss (Pressure Drop) for Pipe Flow," *BrightHub Engineering*, **2010**, accessed on July 31, 2018, <https://www.brighthubengineering.com/hydraulics-civil-engineering/55227-pipe-flow-calculations-3-the-friction-factor-and-frictional-head-loss/>.
- [67] M. V. Shankar, B. Neppolian, S. Sakthivel, B. Arabindoo, M. Palanichamy, V. Murugesan, *Indian J. Eng. Materials Sci.* **2001**, 8, 104.
- [68] R. G. Nair, P. J. Bharadwaj, S. K. Samdarshi, *Ecotoxicol. Environ. Saf.* **2016**, 134, 301.
- [69] R. B. Reed, D. A. Ladner, C. P. Higgins, P. Westerhoff, J. F. Ranville, *Environ. Toxicol. Chem.* **2012**, 31, 93.
- [70] M. Rochkind, S. Pasternak, Y. Paz, *Molecules* **2014**, 20, 88.
- [71] M. Sasges, J. Robinson, F. Daynouri, *Ozone Sci. Eng.* **2012**, 34, 306.
- [72] A. A. Donaldson, Z. Zhang, *AIChE J.* **2012**, 58, 1578.
- [73] *MATLAB*, The MathWorks Inc., Natick, **2013**.

- [74] Q. Zhang, C. Li, T. Li, *Int. J. Photoenergy* **2012**, 2012, 1.
- [75] R. Rowlett, "Units: E," *the University of North Carolina at Chapel Hill*, **2008**, accessed on July 31, 2018, <https://www.unc.edu/~rowlett/units/dictE.html>.
- [76] J. Tschirch, R. Dillert, D. Bahnemann, B. Proft, A. Biedermann, B. Goer, *Res. Chem. Intermed.* **2008**, 34, 381.
- [77] P. Bansal, A. Verma, K. Aggarwal, A. Singh, S. Gupta, *Can. J. Chem. Eng.* **2016**, 94, 1269.
- [78] A. Ivask, T. Titma, M. Visnapuu, H. Vija, A. Kakinen, M. Sihtmae, S. Pokhrel, L. Madler, M. Heinlaan, V. Kisand, R. Shimmo, A. Kahru, *Curr. Top. Med. Chem.* **2015**, 15, 1914.
- [79] H. Khan, M. G. Rigamonti, G. S. Patience, D. C. Boffito, *Appl. Catal. B Environ.* **2018**, 226, 311.
- [80] M. Liu, Y. Liu, D. Zhang, J. Pan, B. Liu, S. Ouyang, *Can. J. Chem. Eng.* **2017**, 95, 922.
- [81] N. Yuangpho, S. T. T. Le, T. Treerujiraphapong, W. Khanitchaidecha, A. Nakaruk, *Phys. E Low-Dimens. Syst. Nanostructures* **2015**, 67, 18.
- [82] K. Farhadian Azizi, M.-M. Bagheri-Mohagheghi, *J. Sol-Gel Sci. Technol.* **2013**, 65, 329.
- [83] A. Cenovar, P. Paunovic, A. Grozdanov, P. Makreski, E. Fidancevska, *Adv. Nat. Sci. Theory Appl.* **2012**, 1, 133.
- [84] A. Ibhaddon, P. Fitzpatrick, *Catalysts* **2013**, 3, 189.
- [85] B. Boga, I. Székely, Z. Pap, L. Baia, M. Baia, *J. Spectrosc.* **2018**, 2018, 1.
- [86] C. Byrne, G. Subramanian, S. C. Pillai, *J. Environ. Chem. Eng.* **2018**, 6, 3531.
- [87] R. R. L. De, D. A. C. Albuquerque, T. G. S. Cruz, F. M. Yamaji, F. L. Leite, "Measurement of the Nanoscale Roughness by Atomic Force Microscopy: Basic Principles and Applications," *Atomic Force Microscopy - Imaging, Measuring and Manipulating Surfaces at the Atomic Scale*, V. Bellitto, Ed., InTech, London **2012**, p. 7.
- [88] D. A. H. Hanaor, C. C. Sorrell, *J. Mater. Sci.* **2011**, 46, 855.
- [89] M. Laamari, A. B. Youssef, L. Bousselmi, *Mater. Res. Innov.* **2018**, 22, 261.
- [90] Y.-C. Liang, C.-W. Chang, *Coatings* **2019**, 9, 90.
- [91] J. Dharma, A. Pisal, "Simple Method of Measuring the Band Gap Energy Value," *PerkinElmer*, **2009**, accessed on June 7, 2019, https://www.perkinelmer.com/lab-solutions/resources/docs/APP_UVVISNIRMeasureBandGapEnergyValue.pdf.

- [92] C. Steinbach, "UV/VIS analysis and optical band gap identification of NM suspension," *Informationen zu Nanomaterialien und Nano-Sicherheitsforschung*, **2016**, accessed on June 4, 2019, https://www.nanopartikel.info/files/projekte/nanOxiMet/SOP/nanOxiMet_SOP_UV_VIS-analysis-optical-band-gap-calculation-NM_V1.pdf.
- [93] J. Zhang, J. Wang, Z. Zhao, T. Yu, J. Feng, Y. Yuan, Z. Tang, Y. Liu, Z. Li, Z. Zou, *Phys. Chem. Chem. Phys.* **2012**, *14*, 4763.
- [94] S. Valizadeh, M. H. Rasoulifard, M. S. S. Dorraji, *Korean J. Chem. Eng.* **2016**, *33*, 481.
- [95] A. S. M. AEM, "ASM Material Data Sheet," **2019**, accessed on March 17, 2019, <http://asm.matweb.com/search/SpecificMaterial.asp?bassnum=mq316q>.
- [96] S. Songara, V. Gupta, M. Kumar Patra, J. Singh, L. Saini, G. Siddaramana Gowd, S. Raj Vadera, N. Kumar, *J. Phys. Chem. Solids* **2012**, *73*, 851.
- [97] S. Yanagida, *J. Ceram. Soc. Jpn.* **2018**, *126*, 625.
- [98] R. Su, R. Bechstein, L. Sjø, R. T. Vang, M. Sillassen, B. Esbjörnsson, A. Palmqvist, F. Besenbacher, *J. Phys. Chem. C* **2011**, *115*, 24287.
- [99] J. Kalb, J. A. Dorman, A. Folger, M. Gerigk, V. Knittel, C. S. Plüsch, B. Trepka, D. Lehr, E. Chua, B. H. Goodge, A. Wittemann, C. Scheu, S. Polarz, L. Schmidt-Mende, *J. Cryst. Growth* **2018**, *494*, 26.
- [100] S. Zhang, Y. Hu, L. Hu, Y. Zhang, Y. Zhou, B. Li, *Micro Nano Lett.* **2019**, *14*, 42.
- [101] X. Luan, X. Liu, C. Fang, W. Chu, Z. Xu, *Environ. Sci. Water Res. Technol.* **2020**, *6*, 2275.
- [102] M. R. Al-Mamun, S. Kader, M. S. Islam, M. Z. H. Khan, *J. Environ. Chem. Eng.* **2019**, *7*, 103248.
- [103] P. Somathilake, J. A. Dominic, G. Achari, C. H. Langford, J.-H. Tay, *Environ. Technol.* **2019**, *40*, 3031.
- [104] J. R. Bolton, K. G. Bircher, W. Tumas, C. A. Tolman, *Pure Appl. Chem.* **2001**, *73*, 627.
- [105] M. Motegh, J. R. van Ommen, P. W. Appel, M. T. Kreutzer, *Environ. Sci. Technol.* **2014**, *48*, 1574.
- [106] Z. Bian, F. Cao, J. Zhu, H. Li, *Environ. Sci. Technol.* **2015**, *49*, 2418.
- [107] S. Kim, M. Kim, S. K. Lim, Y. Park, *J. Environ. Chem. Eng.* **2017**, *5*, 1899.
- [108] C. Jaussaud, O. Païssé, R. Faure, *J. Photochem. Photobiol. Chem.* **2000**, *130*, 157.
- [109] H. K. Singh, M. Saquib, M. M. Haque, M. Muneer, *J. Hazard. Mater.* **2007**, *142*, 425.

- [110] H. E. Krokan, F. Drabløs, G. Slupphaug, *Oncogene* **2002**, *21*, 8935.
- [111] R. Albrektienė, M. Rimeika, E. Zalieckienė, V. Šaulys, A. Zagorskis, *J. Environ. Eng. Landsc. Manag.* **2012**, *20*, 163.
- [112] B. B. Potter, J. C. Wimsatt, Determination of Total Organic Carbon and Specific UV Absorbance at 254 nm in Source Water and Drinking Water **2009**.
- [113] Math UBC, “Snell’s Law -- The Law of Refraction,” **2020**, accessed on August 12, 2020, <https://www.math.ubc.ca/~cass/courses/m309-01a/chu/Fundamentals/snell.htm>.
- [114] T. Koutchma, *Food Bioprocess Technol.* **2009**, *2*, 138.
- [115] VIQUA, “UV Pre-Treatment,” *VIQUA*, **2020**, accessed on December 16, 2020, <https://viqua.com/water-treatment/uv-water-treatment/uv-pre-treatment/>.
- [116] L. A. Morais, C. Adán, A. S. Araujo, A. P. M. A. Guedes, J. Marugán, *Glob. Chall.* **2017**, *1*, 1700066.
- [117] H. Canada, “Escherichia coli in Drinking Water,” *aem*, **2019**, accessed on August 27, 2020, <https://www.canada.ca/en/health-canada/programs/consultation-e-coli-drinking-water/document.html>.
- [118] H. Canada, “Page 9: Guidelines for Canadian Recreational Water Quality – Third Edition,” *aem*, **2012**, accessed on October 6, 2020, <https://www.canada.ca/en/health-canada/services/publications/healthy-living/guidelines-canadian-recreational-water-quality-third-edition/guidelines-canadian-recreational-water-quality-third-edition-page-9.html>.
- [119] X. Li, L. Liu, J. Zhao, J. Tan, *Appl. Spectrosc.* **2015**, *69*, 635.
- [120] TM ASSOCIATES, “DI Water Specifications.htm,” **2020**, accessed on August 10, 2020, <http://www.t Masc.com/di%20water%20specs.htm>.
- [121] Rainfresh, “1 Micron Filter Cartridge, High Performance, Universal Fit | Rainfresh Canada,” *Rainfresh*, **2020**, accessed on August 10, 2020, <http://rainfresh.ca/product/1-micron-filter-cartridge/>.
- [122] T. Hirakawa, C. Koga, N. Negishi, K. Takeuchi, S. Matsuzawa, *Appl. Catal. B Environ.* **2009**, *87*, 46.
- [123] T. Clark, B. Dean, S. Watkins, *AVIAN Advice* **2009**, *11*, 12.

Appendices

Appendix a. *E. coli* Culture and Storage

Growth Curve

Pipet 400 ul *E. coli* (strain ATCC 11303) stock solution in 250 mL (500 mL flask) sterilized LB medium (from Luria-Bertani broth powder, Sigma-Aldrich™), place the flask in an incubator shaker grow 18 hrs at a shaking speed of 150 rpm/min and temperature of 37°C.

Take samples every two hours, and dilute 10 times each time from the sample in 0.85 % w/v NaCl to an estimated dilution to make a CFU (colony forming unit) count between 30 to 300 and spread 0.5 mL dilutions on to LB-Agar (made from Luria-Bertani broth powder and agar powder, Sigma-Aldrich™) petri dishes (100 × 15 mm, Fisher Scientific™) to be placed in the incubator for 18 hours.

Monitor optical density OD600 and observe the change.

Count CFU/mL in each petri dish and plot growth curve in logarithm as Figure a.1., some plated *E. coli* petri dishes are shown in Figure a.2.

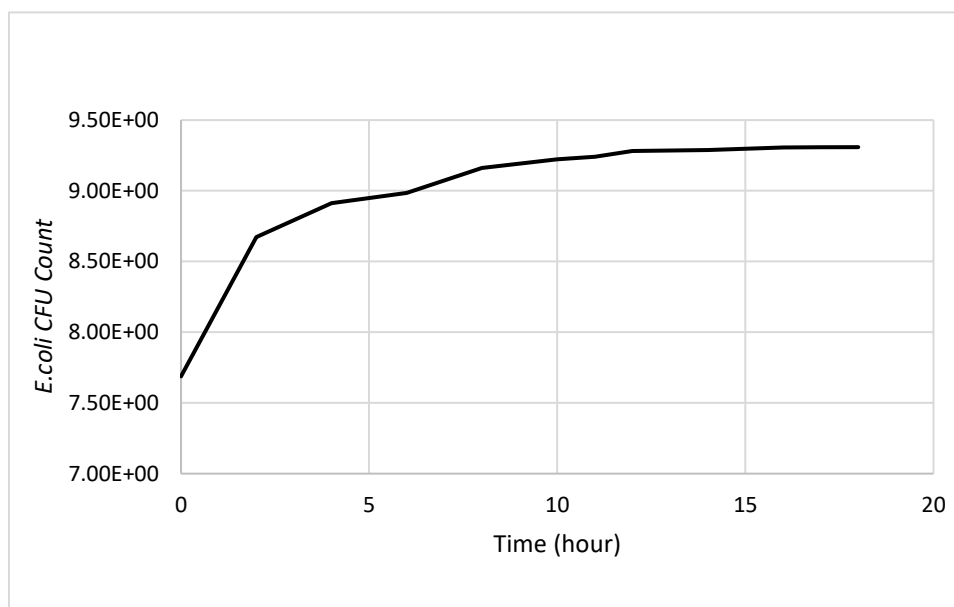


Figure a.1. *E. coli* growth curve

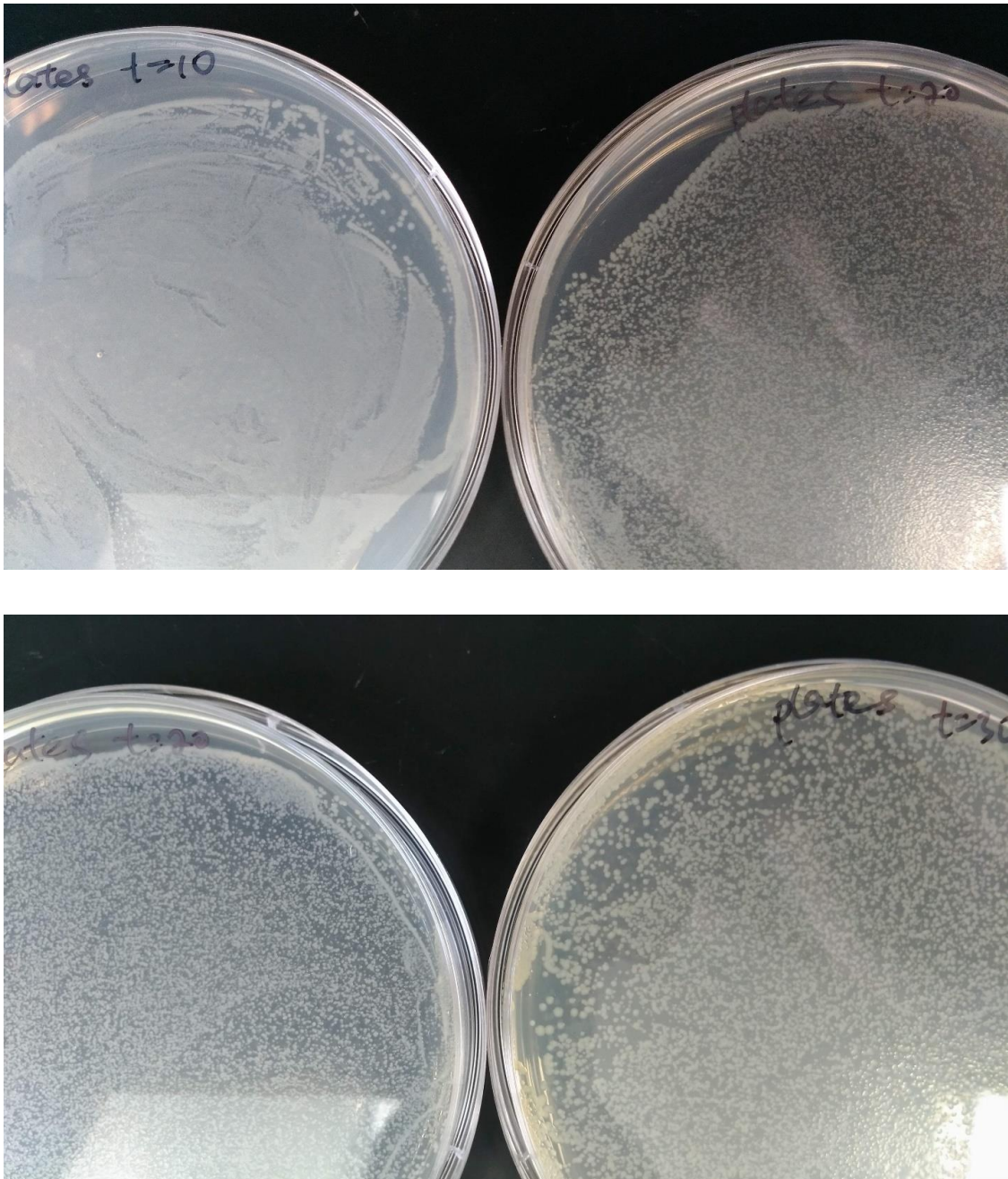


Figure a.2. *E. coli* petri dish

E. coli Freeze Protocol

1. Follow the steps for Inoculating an Overnight Liquid Culture.

2. After you have bacterial growth, add 500 μL of the overnight culture to 500 μL of 50 % glycerol in a 2 mL screw top tube or cryovial and gently mix.

Note: Make the 50 % glycerol solution by diluting 100% glycerol in dH₂O.

Note: Snap top tubes are not recommended as they can open unexpectedly at -80°C.

3. Freeze the glycerol stock tube at -80°C. The stock is now stable for years, as long as it is kept at -80°C. Subsequent freeze and thaw cycles reduce shelf life.

4. To recover bacteria from your glycerol stock, open the tube and use a sterile loop, toothpick or pipette tip to scrape some of the frozen bacteria off of the top. Do not let the glycerol stock unthaw! Streak the bacteria onto a LB agar plate.

5. Grow your bacteria overnight at the appropriate temperature. Growth conditions, including copy number and growth temperature, can be found on your plasmid's information page. The next day you will be able to start an overnight culture for plasmid DNA prep the following day.

***E. coli* stock solution preparation**

E. coli preparation will need the frozen *E. coli* strain, LB medium and 0.85% w/v NaCl water, as well as other materials:

E. coli (atcc11303) was frozen in 2-mL screw top tubes and stored under 20 Celsius.

Luria-Bertani (LB) medium: sterilize 15 g/L LB powder and DI water in an autoclave.

0.85%w/v NaCl water (salt water): sterilize 0.85 g NaCl in 100 mL DI water in an autoclave.

MB solution: mix MB powder in the sterilized salt water to make a concentration of 11 mg/L.

Cell spreader, magnetic stirrers, and the 1.5 mL tube are also sterilized.

Using all solutions in room temperature, keep fridge for the leftovers.

Based on the growth curve, *E. coli* solution is prepared as the following steps:

Take one capsule of *E. coli* from the freezer and unfrozen it in room temperature (about 10 minutes)

Transfer 75 mL LB medium in a 150 mL flask and place it in an incubator shaker (37 Celsius, 130 rpm); pour the dissolved *E. coli* into the flask and incubated for 4 hours and 48 minutes.

Transfer the 37.5 mL *E. coli* solution into a 500 mL flask and add 148.5 mL LB medium in the incubator shaker (37 Celsius, 130 rpm), shaking 17 hrs to obtain the *E. coli* stock solution, which should contain 2×10^9 CFU (colony forming unit)/mL of *E. coli*.

Agar plating

LB agar: sterilize 20 g agar and 15 g LB powder in 1 L DI water in an autoclave.

LB agar plating: wait for the LB agar mixture cool down to 40 to 50 Celsius and pour it in to the transparent plates in front of open flame, cover the plates for a couple hours, then turn the plates upside down to be stored in a plastic bag in a fridge.

Experiments

To make a solution with *E. coli* CFU (colony forming unit)/mL of 10^8 and keep the solution relatively clear, the stock solution is pelleted. Centrifuge about 10 mL *E. coli* stock solution (at 3000 rpm for 10 minutes), decant the LB medium and suspend the pellet in 100 mL 0.85% w/v NaCl water or MB/ NaCl water for use.

After the reactor system sterilization (described above), pump the *E. coli* solution 15 minutes in the system for 15 minutes, pipetting 100 μ L samples at $t=0, 5, 10,$ and 15 minute for agar plating and 200 μ L (3 samples) for microplate reading (at OD600). Each empty plate should be scanned, and the OD reading taken, and another reading taken after having samples, and record the OD difference.

When doing the *E. coli* plating, dilute a 100 μ L sample in the 900 μ L salt water each time, and 5 to 6 times to make the initial CFU/mL in a range between 30 to 300. To have a accurate information of *E. coli* count, 3 plates are needed for each sample. With UV irradiation, samples of should be taken at 10th, 20th and 30th second for plating, but the OD600 reading.

A sample calculation is attached for reference, note that the solution volume used in the calculation was 250 mL, and in these experiments the sample volume to be used is 100 mL with a time range in 15 minutes.

Appendix b. Prototype Photoreactors

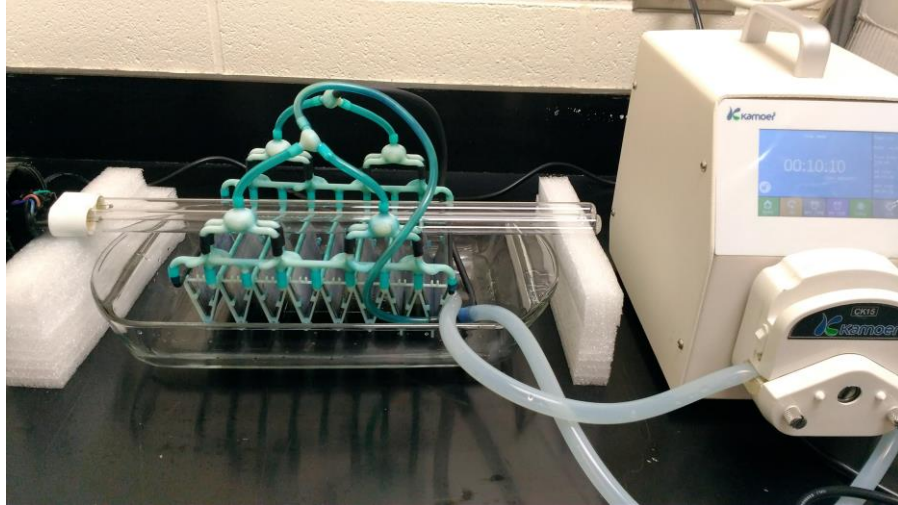


Figure b.1. The 16-plate corrugated plate photoreactor

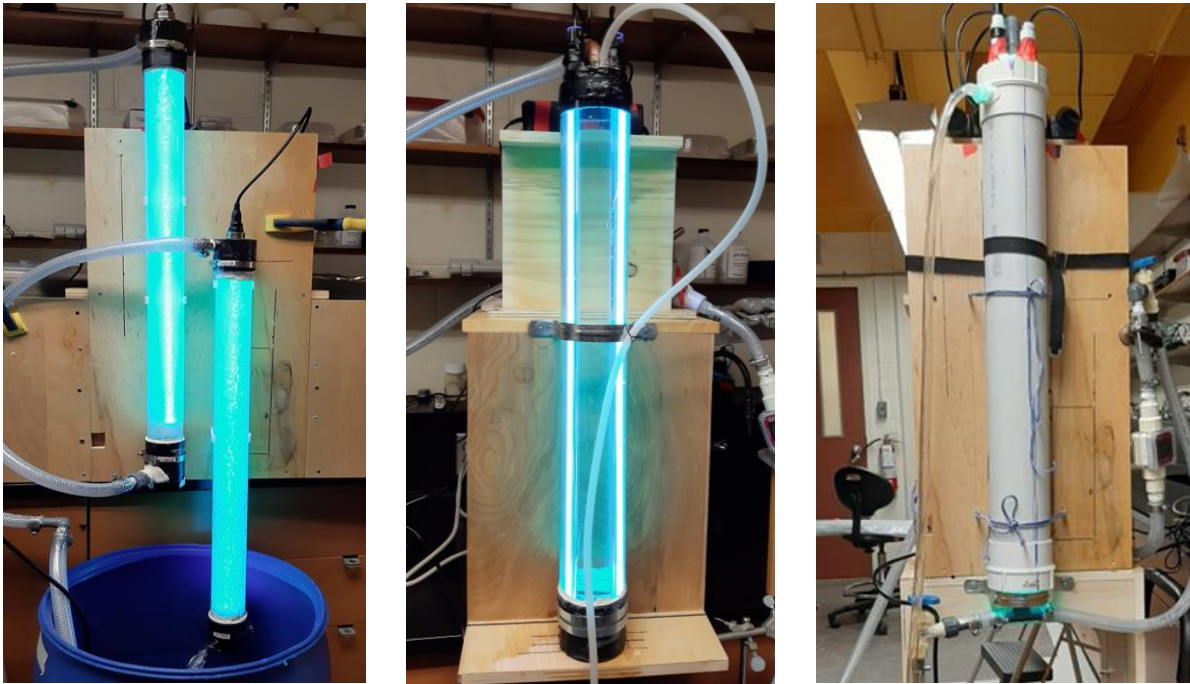


Figure b.2. Tubular photoreactors